C_{60} and its derivatives at Si surfaces: experimental and theoretical studies of electronic structure

by Michael Andrew Phillips, MSci

Thesis submitted to The University of Nottingham
for the degree of Doctor of Philosophy, June 2004.

Contents

Abstract

There has been a considerable amount of research into the effects of the modification of C_{60} on its properties in the bulk and at metal surfaces. Strong covalent interactions between C_{60}, its derivatives, and a silicon substrate, however, are not well understood, nor is their role in determining the electronic properties of a modified fullerene film. In conjunction with existing knowledge concerning the behaviour of unmodified C_{60} at silicon surfaces, the study of modified C_{60} at these surfaces may provide some insight into the nature of the adsorbate–substrate interactions. Furthermore, if the tunability offered by fullerene modification is to be exploited in the production of novel nanoscale devices, an understanding of the role of these interactions is of key importance.

From a theoretical perspective, modelling a fullerene–substrate system can prove to be computationally costly, and an approach to the reduction of this expense has been tested. Relative stabilities of various binding geometries of C_{60} to the Si(100)–(2×1) surface have been determined. Additionally, an agreement between experimental results and a rather simplistic model of the C_{60}/Si interaction suggests that the electronic structure of C_{60} adsorbed at Si surfaces is not strongly dependent upon adsorption geometry – much of the structure in the valence region is inherent to the formation of localised covalent bonds.

Photoemission spectroscopy has been used to study alkali- and noble-metal doping of C_{60} at Si surfaces, and the effects of functional groups on electronic structure and adsorption. An alternative method for the determination of charge transfer from a dopant to the fullerene cage has been proposed and tested. The results show that a metallic phase of K_xC_{60} can exist at the Si(111)–(7×7) surface, but not at the Si(100)–(2×1) surface, and that the LUMO-derived band is split, in both cases. In contrast to the considerable charge transfer seen upon adsorption of C_{60} at noble-metal surfaces, a Si substrate severely limits the interaction of both Ag and Au with thin films of C_{60}. Furthermore, Au demonstrates an interaction with the encapsulated Si surface that is sufficiently strong to displace adsorbed C_{60}. A mechanism for this interaction is proposed. Finally, the addition of phenyl groups to C_{60} is observed to have a profound effect on the chemistry of the fullerene cage itself.

Acknowledgements

I would like to thank my supervisor, Dr. Philip Moriarty, for the help and support he has provided throughout this research, and Dr. James O'Shea, Dr. Michael Hunt, Dr. Karina Schulte, Dr. Nick Besley, Prof. Peter Gill and Prof. Peter Beton for their input to my research.

I would also like to acknowledge the excellent in-house technical support provided by the team in the School of Physics and Astronomy.

Synchrotron beamlines are complicated contrivances, and much of the work presented here would not have been possible without the technical assistance of George Miller, Vin Dhanak, Sunil Patel, Nigel Poolton and Sergei Butorin. I must also thank those that have worked long shifts on beamlines with me, including Amit, Fiona, James, Karina, Li, Mike, Mito, Phil, Rich, and Tony.

Thanks also to past and present members of the Nottingham Nanoscience Group, and others that work (or have worked) within the department.

Special thanks to Jill & Andy, Anne-Marie, Rob, Ste, Stu and Soroosh.

The work presented here was funded by the Engineering and Physical Sciences Research Council.

This document was prepared using LaTeX 2_ε, AFPL Ghostscript and GNU Emacs.

List of publications

Publications directly related to this thesis

1. *K-doped C_{60} monolayers, covalently bound at Si surfaces*,
   M. A. Phillips, J. N. O'shea, V. R. Dhanak, S. Patel, N. J. Poolton and P. Moriarty,
   in preparation, June 2004.

2. *$(C_6H_5)_5C_{60}H$ at Si(111)–(7×7) and Ag:Si(111)–$(\sqrt{3} \times \sqrt{3})R30^\circ$ surfaces*,
   M. A. Phillips, J. N. O'Shea, P. R. Birkett, J. Purton, H. W. Kroto, D. R. M. Walton and P. Moriarty,
   submitted for publication, June 2004.

3. *Competing interactions of noble metals and fullerenes with the Si(111)–(7×7) surface*,
   J. N. O'Shea, M. A. Phillips, M. D. R. Taylor, P. H. Beton, P. Moriarty, M. Kanai, T. J. S. Dennis, V. R. Dhanak, S. Patel, and N. Poolton,
   J. Chem. Phys. 119, 13046 (2003).

4. *Empirical density functional and the adsorption of organic molecules on Si(100)*,
   M. A. Phillips, N. A. Besley, P. M. W. Gill and P. Moriarty
   Phys. Rev. B 67, 035309 (2003).

Other publications

1. *Controlling molecular deposition and layer structure with supramolecular surface assemblies*,
   J. A. Theobald, N. S. Oxtoby, M. A. Phillips, N. R. Champness and P. H. Beton,
   Nature 424, 1029 (2003).

2. *Colloidal particle foams: Templates for Au nanowire networks?*,
   J. N. O'Shea, M. A. Phillips, M. D. R. Taylor, P. Moriarty, M. Brust and V. R. Dhanak,
   App. Phys. Lett. 81, 5039 (2002).

CHAPTER 1

Introduction

During experiments investigating the formation of carbon chains carried out in 1985, time-of-flight mass spectrometry revealed an unusually abundant species containing 60 carbon atoms [1]. Further studies revealed that the stability of this species was not consistent with that expected for a 60-membered carbon chain. The topography of a near-spherical carbon cage had been proposed some years before this discovery [2], and further results showed that this structure was feasible: a new form of carbon, in which the bonding is neither planar nor tetrahedral, had been discovered — C_{60} or buckminsterfullerene. Since then, it has become apparent that the closed-cage structure is not unique to C_{60}: a whole family of fullerene molecules exist.

The discovery of fullerenes, and the development of methods for their synthesis in large quantities [3], was greeted with much interest, largely generated by proposals that the new form of carbon offered great opportunities for development in the fields of novel materials and electronic devices, drug delivery technology and nanoscale structures. Although some of the initial impetus in the field arguably faded to some extent, when very many practical or technological applications of

fullerenes (and their derivatives) were not readily realised, a resurgence of interest in fullerene systems has occurred, largely prompted by the fascinating (and highly cited) discovery of ferromagnetism in polymerised C_{60} [4]. Furthermore, research into the exploitation of fullerenes as core elements of single molecule spectroscopy [5] and fullerene manipulation at surfaces [6–15] continues apace. A highly topical example is that of controllable doping of individual C_{60} molecules placed, using an STM tip, above K atoms on a Ag surface [16].

A particularly attractive feature of the fullerene family of molecules is the ability to modify the electronic structure via the introduction of various species. Such 'doping' can be achieved in a number of ways. In bulk fullerene materials, alkali metals can be incorporated into interstitial sites [17]. Charge is transferred from the metal to the fullerene, filling a band derived from the fullerene lowest unoccupied molecular orbital (LUMO). Such *exohedral* doping has produced materials which demonstrate the full range of electronic behaviour, from insulating, through semiconducting and to superconducting. Various elements (to date, around a third of the periodic table) can be encapsulated within the fullerene cage, yielding an *endohedral* or *incar*-fullerene [18–20]. The endohedral species may cause relaxation of the cage structure, or interact directly with specific atoms of the fullerene cage. Both of these processes result in alteration of the fullerene's electronic structure, and the latter may produce localisation of some of the valence molecular orbitals. Members of the fullerene cage may also be replaced with some other element, producing a *substitutionally*-doped fullerene, such as $C_{59}N$ [21]. Should the valency of the dopant differ from that of carbon, this will certainly lead to orbital localisation. In the case of $C_{59}N$, such localisation creates sites on the cage that are more chemically active, leading to phenomena such as fullerene dimerisation.

In addition to the doping with single species, the susceptibility of fullerenes to nucleophilic attack enables the attachment of various chemical groups to the cage, to produce a *functionalised* fullerene. This offers the potential to introduce new chemistry to the fullerene system. At one extreme, the chemistry of highly reactive functional groups may be expected to dominate the system, whilst it

is conceivable that more benign species could be 'delivered' to a target through the exploitation of fullerene chemistry. Further to direct modification of the electronic structure of the system, the addition of functional groups to a fullerene cage has important implications for the ordering and packing of the material in the bulk. It is believed that the superconductivity of alkali-doped C_{60} arises, in part, as a result of the increased lattice constant within the material. As such, the presence of functional groups may produce fundamental changes in the electronic properties of the bulk material by means which are more subtle than the direct chemical interaction of the functional groups and the cage.

The modification of fullerenes through these methods not only yields novel structural, electronic and chemical behaviour, but this behaviour is tunable, to some extent, through the careful choice of doping-method and dopant. In this respect, the exohedral doping and functionalisation of fullerenes are perhaps the most intriguing, as these offer greater scope for modification, due the sheer number of different elemental dopants and functional groups available, and the variety of stoichiometric and geometric configurations that are possible. In addition to the effects upon bulk material properties, both of these methods of modification raise important issues in the field of surface science. In the case of the former, it is important to understand how interactions of supported fullerene films with the substrate affect the doping process. Certainly, the availability and organisation of sites for occupation by dopant atoms is heavily modified by the proximity of a substrate; complications may also arise from competing interactions of the substrate, fullerene and dopant. In the latter case, it is necessary to address how the presence of functional groups affects adsorption of the host fullerene, particularly with respect to changes in packing that may result in self-assembling systems.

This work seeks to address many of these issues. The results of several experimental investigations are presented; these concern the effects of fullerene functionalisation on bulk properties and adsorption at various silicon surfaces, ranging from reactive to relatively inert, and the role of a reactive silicon substrate in the doping of a fullerene film with metals. In order to understand the physics and chemistry underlying these issues, however, a theoretical understanding of the ad-

sorption of fullerenes at silicon surfaces is necessary. It is only very recently that understanding in this area has begun to develop. For this reason, the feasibility of one approach to a theoretical study of fullerene adsorption is also presented.

CHAPTER 2

Theoretical techniques

In this chapter, concepts concerning the theoretical techniques used in this research are introduced. Molecular mechanics, Hartree-Fock theory and density functional theory are described and the issue of computational expense is discussed, along with various approaches to its reduction. Finally, the chapter provides specific details concerning particular computational methods .

The computational chemistry techniques used in this research fall into three categories: molecular mechanics (MM), *ab initio molecular orbital* (MO) theory, or *Hartree-Fock* (HF) theory, and *density functional theory* (DFT). This section provides a brief introduction to these three areas; much greater detail can be found in comprehensive texts, such as references [22] and [23].

2.1 Molecular mechanics

Molecular mechanical models rely largely upon empirical observations, and exploit the fact that particular functional groups behave similarly within different molecules. As an example, C–H bond lengths are constant in all molecules, to

within a few hundredths of an Ångstrom. Similarly, the stretch frequencies of this bond vary within only a small range from molecule to molecule, implying that that the associated force constant is comparable in different chemical environments. This underlying assumption of molecular mechanics allows a molecular system to be represented as a simplified 'ball and spring' model: atomic centres are represented by balls of an appropriate mass, and the bonds by springs. The energy of a system may then be obtained from the sum of functions corresponding to bonded atom contributions (due to bond stretching, bending and rotation) and non-bonded atom contributions (arising from the Coulomb and van der Waals interactions).

Molecular mechanical models rely upon various species-specific parameters, obtained by fitting the model to experimental data, or to the results of calculations carried out at a higher level of theory. Practically, tabulation of these parameters is broken down beyond the elemental level. Elements are considered in a variety of different chemical environments, yielding a list of 'atom types' such as 'sp^2 carbon in an aromatic ring' and 'hydrogen in an alcohol group', bonds between these species and their associated parameters. The particular classification of atom types and the manner in which their associated parameters are obtained are the features which define a molecular mechanical model.

2.1.1 Bonded atom contributions

Energetic contributions due to bond stretching and bending are relatively trivial. They are often modelled as a parameterised series expansion about a 'natural' bond length or angle. Contributions due to rotation about a bond are not so straightforward to evaluate, since the form of the rotational potential varies not only with the atomic species involved, but also with the nature of the bond. For instance, the potential due to rotation about a bond between two carbon atoms has a periodicity of 180° in ethene, but 120° in ethane. To account for this, rotational contributions are often treated in the form of a Fourier series, in which the n^{th} term represents a rotation of $(360/n)°$. Each term thus describes

the energetic barrier to rotation through a particular angle. Typically, molecular mechanics models include rotational terms up to $n = 3$, since the rotational profiles of many organic molecules include only three minima in a rotation of 360°. A more detailed description of the rotational profile may be obtained by considering higher order terms in the Fourier series.

More elaborate MM methods include terms to account for the coupling between bond stretching and bending: if the angle of a bond is subject to a small change, then the two groups connected by that bond are no longer at their minimum energy separation, leading to a corresponding change in bond length. A suitable term to describe this coupling takes the form of the product of bond angle, bond length and some coupling constant. Similar terms may also be included to consider other types of component coupling, at the expense of introducing additional parameters.

2.1.2 Non-bonded atom contributions

The interaction between pairs of atoms which are not directly bonded is dominated by the effects of polarisation (arising from the formation of chemical bonds) and the van der Waals interaction. Polarisation effects may be treated by consideration of the interaction of dipole moments assigned to each bond. However, it is more common to employ a simplified model in which each atomic centre is assigned an effective charge. The electrostatic energy of the system is obtained by evaluation of the Coulomb potential. It is common, however, to evaluate the Coulomb potential only over pairs of atomic centres, with the result that effects due to screening are excluded. Where screening makes a significant contribution to the energy of the system, its effects may be emulated through the use of an artificially elevated value for the dielectric constant, thereby diminishing the effects of long range electrostatic interactions.

The van der Waals potential[1] produces a force which varies with the separation R between two atoms. The force is repulsive at small R, attractive at

[1] taken to be that implied by the van der Waals gas equation

intermediate R and falls to zero as $R \to \infty$. The repulsive component arises due to Pauli repulsion, and its form can not be completely determined from first principles. However, the behaviour of the overall potential requires that the repulsive component falls to zero at infinite separation, and becomes sufficiently small at intermediate R that the attractive component, which is observed to vary as R^{-6}, may dominate. These considerations give rise to a simple model of the van der Waals potential, known as the Lennard-Jones potential [24] and expressed as

$$E_{LJ} = \varepsilon \left[\left(\frac{R_0}{R} \right)^{-C_r} - \left(\frac{R_0}{R} \right)^{-C_a} \right] \tag{2.1}$$

where:

ε is the depth of the potential minimum;

R_0 is the position of the potential minimum;

C_r is an integer to determine the rate of decay of the repulsive component;

C_a is an integer to determine the rate of decay of the attractive components.

An alternative description of the van der Waals potential may be obtained from further consideration of the nature of the repulsive component. The repulsion arises from the spatial overlap of electronic wavefunctions, which determine electron density. Since electron density decays exponentially with distance from an atomic centre, the repulsive term in equation 2.1 may be replaced with an exponential term in R and R_0. The result is known as the Hill potential [25].

These models of the van der Waals potential are used in molecular mechanics in order to account for the van der Waals radii of atoms (R_0) and the attraction between non-bonded pairs. However, van der Waals effects are often seen between functional groups, for example, in hydrogen bonding. Both the Lennard-Jones and the Hill potential can be applied to multi-atom species through the use of modified parameters: R_0 is replaced with $\sum_i R_{0i}$ and ε with $\overline{\varepsilon_i}$. Depending upon the system, this can be a poor approximation since it neglects variations in the potential due to many-body effects. To compensate for this, MM methods may

include empirically determined van der Waals parameters for common functional groups, in addition to those for the various atom types. The fact that these parameters are obtained empirically implies that they include some many-body contribution.

2.1.3 Limitations

MM is a very simplistic model which does not include any consideration of electrons. As a result, it can reveal nothing concerning the distribution of electronic charge within a system, and consequently is of no use for studies of charge transfer effects, or the organisation of chemical bonds in novel systems. Furthermore, the success of a particular MM method in predicting the properties of some system relies heavily on the data set used to determine the parameters of that method. This data set is finite: if the system under study incorporates components or configurations which are not represented in the data set, the method can not be expected to perform well. However, the simplicity of MM results in a very low computational expense. As a result, MM can prove extremely useful in searching for stable binding configurations within a system, provided that the particular method used is well matched to that system.

2.2 Molecular orbital (MO) theory

Hartree-Fock theory is a truly *ab initio* technique, in that it is completely derived from first principles. Since the late 1950's, it has been used to determine details concerning the electronic structure of small systems. With more recent developments in computational capabilities, HF is commonly used in conjunction with variational procedures to determine the properties of increasingly complex systems.

The theory is derived directly from fundamental quantum mechanics, which stipulates that the energy of a system can be found by solving the Schrödinger

equation. In the time independent form, this may be generalised to

$$\hat{H}\Psi = E\Psi \tag{2.2}$$

in which:

Ψ is the wavefunction;

$\hat{H}$ is the Hamiltonian operator;

E is the energy of the system.

For many-body systems, it is not possible to solve the Schrödinger equation exactly: various assumptions and approximations are necessary.

2.2.1 The Born-Oppenheimer approximation

A molecular system consists of electrons and atomic nuclei, of which the latter are much more massive. The Born-Oppenheimer approximation assumes that the velocities of the nuclei are negligible when compared to those of the electrons, due to this difference in mass. Equation 2.2 is then separable into electronic and nuclear components:

$$\hat{H}_e\Psi_e = E_e\Psi_e \tag{2.3}$$

$$\hat{H}_n\Psi_n = E_n\Psi_n \tag{2.4}$$

with

$$\hat{H}_e = \hat{T}_e + \hat{V}_{ee} + \hat{V}_{en} \tag{2.5}$$

$$\hat{H}_n = \hat{V}_{nn} \tag{2.6}$$

where $\hat{T}$ & $\hat{V}$ represent kinetic and potential energy operators, and the subscripts e and n refer to electrons and nuclei. The nuclear Hamiltonian contains only a single term, corresponding to the Coulomb potential of the nuclear system; there is no kinetic component, due to the assumption of negligible nuclear velocity. The electronic Hamiltonian contains terms corresponding to the kinetic energy of the electrons, and the sum of electronic potentials in both the field of all other electrons and the field of the nuclei.

The electronic Schrödinger equation is now only dependent upon the position of the nuclei, and not their momenta. However, it may still only be exactly solved for, at most, H_2^+. Furthermore, the Hamiltonian resulting from the Born-Oppenheimer approximation is non-relativistic: spin is neglected, and effects such as spin-orbit and spin-spin coupling remain unaccounted for. Additional approximations are required and the effects of spin must be considered.

2.2.2 The Hartree-Fock approximation

The Hartree-Fock approximation assumes that all electrons in a system move independently of one another. This allows expression of the all-electron wavefunction in terms of one-electron wavefunctions, which in turn enables consideration of the effects of spin. Despite its relativistic origins, spin may introduced into a non-relativistic theory as required. Here, this is achieved by defining each one-electron wavefunction as a product of a spatial wavefunction and a function that represents spin. The latter is always one of two functions, α and β, which are orthonormal. This definition yields a set of one-electron *spinorbitals*, χ_i.

The all-electron wavefunction could be constructed from the sum of the one-electron spinorbitals. However, there is one important criterion in the consideration of electrons that this approach neglects: electrons are fermions, and so the total electronic wavefunction must be asymmetric with respect to the interchange of electron co-ordinates. In order to ensure asymmetry of the all-electron wavefunction, it is constructed from a determinant in terms of the single-electron wavefunctions. This construction is known as the Slater determinant (SD),

$$\Phi_{\mathrm{SD}} = \frac{1}{\sqrt{N!}} \begin{vmatrix} \chi_1(1) & \chi_2(1) & \cdots & \chi_N(1) \\ \chi_1(2) & \chi_2(2) & \cdots & \chi_N(2) \\ \vdots & \vdots & \ddots & \vdots \\ \chi_1(N) & \chi_2(N) & \cdots & \chi_N(N) \end{vmatrix} \tag{2.7}$$

in which N is the total number of electrons. Each column represents a single-electron wavefunction, or *molecular orbital* (MO), and electron co-ordinate increases as a row is traversed from left to right.

2.2.3 The Hartree-Fock equations

It is possible to use a superposition of Slater determinants as the trial electronic wavefunction. However, derivation of the Hartree-Fock equations relies upon the assumption that this wavefunction consists of a single determinant. The electronic energy is then

$$E = \left\langle \Phi_{\mathrm{SD}} | \hat{H}_e | \Phi_{\mathrm{SD}} \right\rangle \tag{2.8}$$

By collecting the terms in $\hat{H}_e$, the energy of the Slater determinant can be expressed as

$$E_e = \sum_{i=1}^{N} h_i + \frac{1}{2} \sum_{i,j}^{N} \left(J_{ij} + K_{ij} \right) \tag{2.9}$$

with

$$h_i = \int \chi_i^* \left(\mathbf{r}_1 \right) \left[-\frac{1}{2} \nabla^2 - \sum_a \frac{Z_a}{|\mathbf{R}_a - \mathbf{r}_i|} \right] \chi_i \left(\mathbf{r}_1 \right) \, d\mathbf{r}_1 \tag{2.10}$$

$$J_{ij} = \iint \chi_i \left(\mathbf{r}_1 \right) \chi_i^* \left(\mathbf{r}_1 \right) \frac{1}{\mathbf{r}_{12}} \chi_j \left(\mathbf{r}_2 \right) \chi_j^* \left(\mathbf{r}_2 \right) \, d\mathbf{r}_1 \, d\mathbf{r}_2 \tag{2.11}$$

$$K_{ij} = \iint \chi_i^* \left(\mathbf{r}_1 \right) \chi_j \left(\mathbf{r}_1 \right) \frac{1}{\mathbf{r}_{12}} \chi_i \left(\mathbf{r}_2 \right) \chi_j^* \left(\mathbf{r}_2 \right) \, d\mathbf{r}_1 \, d\mathbf{r}_2 \tag{2.12}$$

h_i includes terms corresponding to the kinetic energy of electron i and its potential in the field of all nuclei. J_{ij} is the *Coulomb integral*, representing classical electrostatic repulsion, and K_{ij} is the *exchange integral*, which has no classical analogue. All of these integrals may be replaced with appropriate operators in the Hamiltonian: $\hat{h}_i$, $\hat{J}_i$ and $\hat{K}_i$. Application of the variational principle then yields the set of Hartree-Fock equations,

$$\hat{\mathbf{f}}_i \chi_i = \sum_j^N \lambda_{ij} \chi_i \tag{2.13}$$

where $\hat{f}_i$ is the *Fock operator*:

$$\hat{f}_i = \hat{h}_i + \sum_j \left(\hat{J}_j - \hat{K}_j \right) \tag{2.14}$$

It contains terms relating to the kinetic, Coulomb and exchange energy of a given electron; the use of a single-determinant wavefunction results in no correlation

term. λ_{ij} is a set of Lagrange multipliers, forming a Hermitian matrix. This can be further simplified through a linear transformation of the MOs to diagonalise the matrix of Lagrange multipliers such that

$$\begin{aligned} \lambda_{ij} &\rightarrow 0 \\ \lambda_{ii} &\rightarrow \epsilon_i \\ \chi_i &\rightarrow \chi'_i \end{aligned}$$

and thus

$$\hat{f}_i \chi'_i = \epsilon_i \chi'_i \tag{2.15}$$

is obtained. χ'_i are the set of *canonical MOs*, and the Lagrange multipliers, ϵ_i, are the expectation values of the Fock operator in this basis.

2.2.4 Energies from MO theory

Due to the presence of the Coulomb and exchange integrals, the Fock operator is dependent upon all occupied MOs: a given orbital can only be obtained if all other occupied MOs are known. Equation 2.15 is therefore a pseudo-eigenvalue problem that may only be solved through the use of an iterative approach. The orbitals which satisfy this problem are known as a set of *self consistent field* (SCF) orbitals. Once the SCF orbitals have been obtained, equation 2.9 can be employed to obtain the total energy of the system:

$$E = \sum_i^N \epsilon_i - \frac{1}{2} \left(\hat{J}_j - \hat{K}_j \right) \chi'_i + V_{nn} \tag{2.16}$$

Each ϵ_i in equations 2.15 and 2.16 may be taken as the energy of MO i. For larger systems, this has further implications. For a system with many electrons, the relaxation of MOs caused by the excitation, addition or removal of an electron can be, in some cases, assumed to be negligible. Thus, results of a ground state calculation can predict values of ionisation energy (from the occupied MO energies), electron affinity (from unoccupied MO energies) and excitation energies. This result is known as *Koopmans' Theorem* [26].

However, solving for the SCF orbitals is not trivial. The Hartree-Fock equations consist of a set of coupled partial-differential equations. These may be solved

numerically, but for more complex systems this approach becomes unfeasible: an analytical approach is preferable.

2.2.5 Basis set expansion and the Roothaan-Hall equations

The Hartree-Fock equations may be reduced to a matrix eigenvalue equation through the expansion of the molecular orbitals, χ_i, in terms of a linear combination of a set of known functions, the *basis set*:

$$\chi_i = \sum_{m=1}^{K} C_{mi}\phi_m \tag{2.17}$$

By substituting this into the Hartree-Fock equations, multiplying by the conjugate of a particular basis function and integrating, the problem may be represented in matrix form as

$$\mathbf{FC} = \mathbf{SC}\epsilon \tag{2.18}$$

$\mathbf{C}$ is the matrix of expansion coefficients, c_{mi}. The matrix elements of $\mathbf{F}$ (the *Fock matrix*) and $\mathbf{S}$ (the *overlap matrix*) are defined as

$$F_{mn} = \left\langle \chi_m \left| \hat{f} \right| \chi_n \right\rangle \tag{2.19}$$

$$S_{mn} = \langle \chi_m | \chi_n \rangle \tag{2.20}$$

These are the *Roothaan-Hall* equations [27,28], and they may be solved by varying the parameters of the basis functions in order to minimise the resulting energy. Methods resulting from such a solution are classed as Hartree-Fock methods.

2.2.6 Computational Implementation

Conceptually, any functional form may be used in order to carry out expansion of the MOs in terms of a basis set. However, the basis functions should permit a reasonable description of the MOs — the basis functions must be physically representative of the problem in order to allow the convergence of any variational approach. As such, it is usual to choose one-electron basis functions that are representative of solutions to the Hartree-Fock equations for hydrogen. Typically,

these basis functions are centred about the positions of nuclei, and are therefore termed *atomic orbitals* (AO). Their use in the expansion given in equation 2.17 constitutes an approximation known as *linear combination of atomic orbitals* (LCAO). It should be noted that the atomic orbitals are merely a construction. They are only *representative* of one-electron atomic solutions, and do not necessarily constitute such solutions in their own right — their mathematical form is arbitrary. The practical construction of basis sets will be discussed later.

In the Roothaan-Hall equations (given in matrix form in equation 2.18), each element of $\mathbf{F}$ contains one-electron integrals due to $\hat{h}$, in addition to a sum over all occupied MOs of coefficient products and two-electron integrals arising from $\hat{J}$ and $\hat{K}$. For computational convenience, it is useful to write the two-electron components as a product of a *density matrix*, $\mathbf{D}$, and the two-electron integrals, $\mathbf{G}$:

$$\mathbf{F} = \mathbf{h} + \mathbf{G}.\mathbf{D} \tag{2.21}$$

The matrix elements of $\mathbf{h}$ are the one-electron integrals, and those of $\mathbf{D}$ and $\mathbf{G}$ are defined as:

$$D_{pq} = \sum_{j}^{\text{Occupied MO}} c_{pq}c_{pq} \tag{2.22}$$

$$G_{pq} = \sum_{r}^{\text{AO}}\sum_{s}^{\text{AO}} \langle\chi_p\chi_r|\hat{g}|\chi_q\chi_s\rangle - \langle\chi_p\chi_r|\hat{g}|\chi_s\chi_q\rangle \tag{2.23}$$

where $\hat{g}$ is the electron–electron repulsion operator. The construction of the density matrix, $\mathbf{D}$, enables determination of the unknown MO coefficients through an iterative process. Initially, $\mathbf{D}$ is obtained from guesses of MO coefficients, which are typically tabulated for a given basis set. The one- and two-electron integrals are evaluated, and used in conjunction with $\mathbf{D}$ to obtain the Fock matrix, $\mathbf{F}$. A unitary transformation is applied to diagonalise $\mathbf{F}$ and generate a new density matrix which, in turn, is used to re-evaluate $\mathbf{F}$. This iterative process is repeated until the density matrix is unchanged by diagonalisation of $\mathbf{F}$, within the limit of some threshold level. Once this condition has been met, the Fock matrix represents a set of SCF orbitals.

2.2.7 Restricted, restricted open-shell and unrestricted HF

The specific treatment of electron spin results in three distinct classes of HF wavefunction. When considering systems with singlet multiplicity (*closed shell* systems), it is possible to insist that electrons of opposite spin are paired in doubly-occupied MOs. Pairs of α- and β-spinorbitals are described by the same spatial wavefunction; the determinant wavefunction and calculation are described as *restricted Hartree-Fock* (RHF).

Open shell systems, on the other hand, have a multiplicity greater than singlet, arising from excited states or the presence of an odd number of electrons. For such systems, it is not possible to meet the RHF condition. The case may be treated by using the same spatial co-ordinates to describe α- and β-spinorbitals, and imposing single-occupancy on a sufficient number of the highest occupied MOs to obtain the desired multiplicity. This produces a spin-*restricted open-shell Hartree-Fock* (ROHF) wavefunction.

If no such limitations on spin pairing are enforced, the calculation is described as *unrestricted Hartree-Fock* (UHF). α- and β spinorbitals are treated with separate sets of spatial co-ordinates, but are coupled by the Coulomb part of the Fock operator. As a result, a given pair of spinorbitals can become spatially separate, which may result in a reduction in the energy of the system. However, this separation implies that the α and β components are energetically distinct, and hence the overall wavefunction is no longer an eigenfunction of the total spin operator $\langle \mathbf{S}^2 \rangle$. This introduces an error in the calculation termed *spin contamination*, in which the resulting wavefunction is tainted by admixtures of higher spin states than that required. If spin contamination is large, there may be discrepancies in the molecular structure, electron density and spin density obtained from the calculation. Typically, however, spin contamination is small; this can be verified by comparing the result of the spin expectation operator to the theoretical value for the correct multiplicity.

2.2.8 Limitations

Hartree-Fock techniques have proven to be successful in the calculation of the ground state energies of many systems and, in conjunction with Koopmans' theorem, the prediction of excitation energies, ionisation energies and electron affinities. However, there are some significant limitations to Hartree-Fock theory.

Firstly, multiple unpaired electrons are not treated well using HF theory. It is not possible to consider such states using RHF wavefunctions. The ROHF approach frequently presents problems with convergence, possibly due to discontinuities in the determinant energy arising from constraints on the spin-state of the highest occupied MOs. UHF wavefunctions, on the other hand, are at a disadvantage in that they may describe spin states that are not pure. As a result, HF theory may perform poorly in predicting the properties of systems with a high spin multiplicity, such as ionic states and highly dissociated systems. UHF wavefunctions can produce excellent results, but care must be taken to ensure that spin contamination does not significantly affect the properties of interest.

Secondly, HF theory relies on construction of the wavefunction from a single Slater determinant, and is therefore entirely non-relativistic. The effects of spin are considered *ad hoc*, but beyond this, no relativistic effects are accounted for. As such, the theory is inappropriate for the study of systems involving heavy nuclei.

Finally, and most significantly, the independent particle approximation results in the neglect of any instantaneous interactions between electrons. Any coupling in the motion of electrons is not considered, and the electron-electron repulsion is overestimated. The energy resulting from such effects is termed the *correlation energy*, and is defined as

$$E_{\text{cor}} = E_{\text{exact}} - E_{\text{HF}} \tag{2.24}$$

where E_{exact} is the energy resulting from an exact solution of the Schrödinger equation and E_{HF} is that obtained from HF theory. The correlation energy is typically small, but can become significant, for example, in systems which contain many electrons localised within the same region, or small bandwidth systems

such as fullerenes and crystals. There are a number of theories which attempt to account for the correlation energy but only one of these, *density functional theory*, is relevant to the work in this thesis.

2.3 Density Functional Theory (DFT)

Density functional theory [29] arises from two theorems, the proofs of which were given by Hohenberg and Kohn [30]. The first asserts that the electron density, $\rho(\mathbf{r})$, completely determines the observable ground state properties of an electronic system: the energy of that system can be expressed as some functional of the density, $E[\rho]$. The second theorem states that any trial density, $\rho_t(\mathbf{r})$, satisfying

$$\rho_t(\mathbf{r}) \geq 0 \text{ and } \int \rho_t(\mathbf{r})\, d\mathbf{r} = N$$

where N is the total number of electrons in the system, will yield an energy which is greater than that of the system's ground state. By analogy to the Hamiltonian in HF theory, the energy functional can be expressed in terms of a number of components:

$$E[\rho] = T[\rho] + V_{\text{ne}}[\rho] + V_{\text{ee}}[\rho] \tag{2.25}$$

$T[\rho]$ is the electronic kinetic energy. $V_{\text{ne}}[\rho]$ and $V_{\text{ee}}[\rho]$ are potential terms, the former arising from the interaction of electrons with the field of the nuclei (or, more generally, any field external to the electronic system), and the latter from electron–electron interactions. The first of these two potentials is obtained rather trivially, by integrating the action of the external field on the electron density over all space. The forms of the kinetic term and electron–electron potential, however, can not be determined from first principles, and their expression in suitable forms has been the subject of much research over the past three decades.

Early approaches to the problem of the unknown functionals, such as the *Thomas Fermi* (TF) and *Thomas Fermi Dirac* (TFD) functionals, take the electron–electron potential as the Hartree energy, which is that due to the Coulomb

interaction,

$$V_{\mathrm{H}}[\rho] = \frac{1}{2} \iint \frac{\rho(\mathbf{r})\rho(\mathbf{r}')}{|\mathbf{r}\mathbf{r}'|}\, d\mathbf{r}\, d\mathbf{r}' \tag{2.26}$$

Expressions for the kinetic term are obtained from considerations of an idealised, uniform and non-interacting electron gas. The kinetic expressions proved to be very crude approximations and, although the Coulomb potential is a significant component of $V_{\mathrm{ee}}[\rho]$, it does not cover the full scope of electron–electron interactions. The TF and TFD models fail to predict any bonding, and as such are of no use in the study of molecular or covalent crystalline systems.

To tackle the problem of determining an expression for the kinetic energy, Kohn and Sham introduced a formalism in which this term is split into two parts:

$$T[\rho] = T_{\mathrm{KS}}[\rho] + (T[\rho] - T_{\mathrm{KS}}[\rho]) \tag{2.27}$$

The term $T_{\mathrm{KS}}[\rho]$ is the kinetic energy of a fictitious system of N non-interacting particles, represented by a single Slater determinant consisting of N *Kohn-Sham* orbitals, ϕ_i, which reproduce the real particle density:

$$\rho(\mathbf{r}) = \sum_{i}^{N} |\phi_i|^2 \tag{2.28}$$

The kinetic energy of the non-interacting system can then be found by solution of the Schrödinger wave equation:

$$T_{\mathrm{KS}} = -\frac{1}{2} \sum_{i} \int \phi_i^*(\mathbf{r}) \nabla^2 \phi_i(\mathbf{r})\, d\mathbf{r} \tag{2.29}$$

The electron–electron interaction is treated similarly, taking the exact part as the Hartree energy (equation 2.26):

$$V_{\mathrm{ee}} = V_{\mathrm{H}}[\rho] + (V_{\mathrm{ee}}[\rho] - V_{\mathrm{H}}[\rho]) \tag{2.30}$$

The errors in $T[\rho]$ and $V_{\mathrm{ee}}[\rho]$ arising from the non-interacting and Hartree energy approximations are then assimilated into a new term: the *exchange-correlation* (XC) functional, $E_{\mathrm{xc}}[\rho]$, which thus incorporates the exchange energy, the correlation energy and a kinetic correction. The total energy functional may then be written as

$$E[\rho] = T_{\mathrm{KS}}[\rho] + V_{\mathrm{ne}}[\rho] + V_{\mathrm{H}}[\rho] + E_{\mathrm{xc}}[\rho] \tag{2.31}$$

which, in the absence of any external applied field, becomes

$$= -\frac{1}{2}\sum_i \int \phi_i^*(\mathbf{r})\nabla^2\phi_i(\mathbf{r})\,d\mathbf{r} - \sum_a \int \frac{Z_a\rho(\mathbf{r})}{|\mathbf{R}_a - \mathbf{r}|}\,d\mathbf{r} + \frac{1}{2}\iint \frac{\rho(\mathbf{r})\rho(\mathbf{r}')}{|(r)_1\mathbf{r}_2|}\,d\mathbf{r}\,d\mathbf{r}' + E_{\mathrm{xc}}[\rho] \tag{2.32}$$

Given a specific expression for $E_{\mathrm{xc}}[\rho]$, the energy functional becomes completely defined. Equation 2.32 can be expressed in the form of an operation on the Kohn-Sham orbitals, ϕ_i, yielding a pseudo-eigenvalue problem analogous to that obtained in HF theory:

$$\mathbf{h}_{\mathrm{KS}}\phi_i = \epsilon_i\phi_i \tag{2.33}$$

Again, the problem has a self-consistent field solution, obtainable through expansion of the Kohn-Sham orbitals in terms of a basis set.

2.3.1 Approximations to the exchange-correlation term

The generalised form of E_{xc} is

$$E_{\mathrm{xc}} = \int \rho(\mathbf{r})\varepsilon_{\mathrm{xc}}[\rho, \mathbf{r}]\,d\mathbf{r} \tag{2.34}$$

with $\varepsilon_{\mathrm{xc}}$ dependent on the form of $\rho(\mathbf{r})$ at all points in space, but its exact form is not known. However, there are a number of widely used forms, resulting from much research, many of which are based on one of the following approximations.

The most straightforward manner in which to reduce the complexity of $\varepsilon_{\mathrm{xc}}$ is the *local density approximation* (LDA), or its generalised form, the *local spin density approximation* [31]:

$$E_{\mathrm{xc}} = \int \rho(\mathbf{r})\varepsilon_{\mathrm{xc}}(\rho(\mathbf{r}))\,d\mathbf{r} \tag{2.35}$$

Thus the exchange-correlation energy at a point, $\mathbf{r}$, is only dependent on the density at that point. Another, slightly more complex, approximation includes local density gradients: the *generalised gradient approximation* (GGA) [32, 33],

$$E_{\mathrm{xc}} = \int \rho(\mathbf{r})\varepsilon_{\mathrm{xc}}(\rho(\mathbf{r}), \nabla\rho(\mathbf{r}), ...)\,d\mathbf{r} \tag{2.36}$$

Certain density functionals also include the exact Fock exchange from Hartree-Fock theory as a component in the XC term. Such functionals are known as *hybrid* functionals.

2.3.2 Implementation

Unlike HF theory which, using the LCAO basis set expansion, can be solved entirely analytically, DFT relies upon numerical techniques. Typically, an implementation of a DFT method will evaluate various terms by different means. Electron–electron contributions, excluding the exchange and correlation terms, may be evaluated analytically in the same manner as in HF theory, through computation of the Coulomb integrals. Alternatively, since DFT considers electron density, more advanced techniques based on multipole expansions may be employed. The XC functional is the cause for dependence upon numerical techniques. Analytical methods to evaluate the required integrals are not available, and the XC contribution must be calculated through the use of numerical quadrature over a set of grid points. The accuracy and success of a particular DFT implementation depends, to a large extent, on the specification of this grid. As such, much contemporary research concentrates on the development of superior grid specification techniques. Finally, a density functional method may call for the exact Fock exchange. There is no other way to calculate this than the evaluation of two-electron integrals from Hartree-Fock theory.

The manner in which various terms are calculated has significant consequences for the computational expense of an implementation of DFT. Pure density functional methods can demonstrate a considerably lower computational expense than HF methods, as the use of multipole methods can yield a significant benefit over the conventional evaluation of integrals. The main reduction in computational expense arises from the fact that it is not necessary to evaluate the two-electron integrals for the Fock exchange. Calculations involving hybrid density functionals, on the other hand, do require evaluation of these integrals and, as a consequence, their computational expense is comparable to, if not greater than, the corresponding HF calculations.

2.3.3 Limitations

Although the Kohn-Sham formalism of density functional theory employs the concept of orbitals, these orbitals may not be considered to be the same as the molecular orbitals of HF theory. They are Kohn-Sham orbitals, describing a fictitious set of non-interacting particles, and their physical interpretation is still a matter of debate. Koopmans' theorem is particular to Hartree-Fock theory; however, a similar theorem exists for DFT. The theorem is specific to the highest occupied Kohn-Sham orbital, stating that the eigenvalue of this orbital may be taken as the first ionisation energy, but its proof has been questioned [34]. Generally, other KS eigenvalues must be scaled or shifted by some quantity in order to correspond to physical electronic potentials. The scaling factor varies, depending upon the density functional used, but DFT typically underestimates energy differences such as the band gap in semiconducting systems. Very recently, evidence has been produced to suggest that the DFT analogue of Koopmans' theorem can be applied to other occupied Kohn-Sham orbitals, in order to determine approximate ionisation energies [35].

2.4 Methods to reduce computational expense

MO/HF and DFT methods require considerable computational power, in order to evaluate all of the required integrals and matrices. As a general rule of thumb, the computational expense of a given method may be expected to increase as N^4, where N is the total number of basis functions. Calculations concerning systems larger than, for example, a few tens of silicon atoms can become unfeasible. Molecular mechanical methods are no substitute for HF or DFT calculations, as they do not consider electronic structure in any way. For these reasons, it is often necessary to make additional approximations to reduce the complexity of a system, and thus reduce computational expense. Two methods which implement such approximations have been used in this research: *semi-empirical* methods and *pseudopotential basis sets*, or *effective core potentials* (ECPs).

2.4.1 Effective core potential basis sets

In any chemical system, a large proportion of the electrons occupy core-level orbitals. In larger atoms ($Z > 10$), these electrons become chemically unimportant. The complexity of the system may be reduced by not treating these core-level electrons explicitly. To account for effects such as the repulsion between core-level and valence electrons, the core-level orbitals may be replaced by an *effective core potential*. The core potential is represented by some parameterised function which is typically fitted to data obtained from calculations at a very high level of theory. These high-level calculations can involve relativistic theory, and thus the use of an ECP basis set can incorporate some relativistic effects into non-relativistic HF and DFT calculations: ECP basis sets have been seen to give good agreement with experimental data, particularly for systems involving heavier elements.

2.4.2 Semi-empirical methods

A semi-empirical method aims to reduce the computational complexity of a HF calculation by reducing the number of integrals that must be evaluated. There are a number of considerations which rationalise the omission of various integrals.

The most obvious approach to the reduction of the number of required integrals is to reduce the number of electrons in a system that are treated explicitly, and the number of basis functions with which they are modelled. Semi-empirical methods typically replace core-level orbitals with an effective core potential. Each of the remaining orbitals is modelled using the fewest possible basis functions, in a *minimal basis set*, details of which are given in section 2.5.3.

Even with the explicit treatment of only valence electrons, there still remains a considerable number of two-electron integrals, the evaluation of which forms the major contribution to the computational expense incurred by a calculation. Many of these terms, however, have values very close to zero, and so may be neglected. In many semi-empirical methods, this is achieved through the *neglect of diatomic differential overlap* (NDDO) approximation [36–39], which asserts that the overlap density arising from two atomic orbitals centred about different

atoms is zero:

$$\langle \psi_r(1)\,\psi_s(2)\,|1/r_{12}|\,\psi_t(1)\,\psi_u(2)\rangle = 0 \tag{2.37}$$

if either ψ_r and ψ_t or ψ_s and ψ_u reside on different atoms. In this way, the NDDO approximation includes interactions of the overlap density of two atomic orbitals on one atom with that of two atomic orbitals on the same or one other atom. The effect is a reduction of the overlap matrix, $\mathbf{S}$, in the Roothaan Hall equations, eliminating the need for evaluation of a number of two-electron integrals. The results of those integrals that remain are expressed in parameterised forms and fitted to experimental data. It is the manner in which remaining integrals are parameterised which defines a particular semi-empirical method.

Semi-empirical methods offer a great reduction in computational expense and, since their parameters are fitted to experimental data, some effects of electron correlation may be indirectly considered. However, as for molecular mechanics, a semi-empirical method can not be expected to perform well when applied to the study of systems containing species or combinations which are poorly represented in the data set used for parameterisation. It is therefore important to choose a particular semi-empirical method which is appropriate to the chemistry of the system of interest.

2.5 Specific techniques

2.5.1 Merck molecular force field 94 (MMFF94)

MMFF94 [40–45] is a non-specialised molecular mechanics technique which uses 99 atom type definitions. Since it is non-specialised, it is suited to the study of a variety of systems. The model uses the charge centre approach, as opposed to interacting dipoles, to account for electrostatic effects. The van der Waals interaction is modelled using the Lennard-Jones potential (equation 2.1), with values of 14 and 7 for C_r and C_a. Bond stretching and bending energies are modelled using polynomials of order 3 and 4, respectively, and a term to describe coupling between the two.

2.5.2 Semi-empirical methods

Three semi-empirical methods were considered for use in this research: *modified neglect of diatomic orbitals* (MNDO) [46], *Austin method 1* (AM1) [47, 48] and *parameterised method 3* (PM3) [49–51]. The three methods are closely related. MNDO is purely parametric, but has been observed to systematically overestimate various interatomic interactions. AM1 is a development from MNDO, with the inclusion of Gaussian functions to better model interactions between core-level electrons. PM3 uses the same 'parameter + Gaussian' model as AM1, but its parameters are fitted to a much larger set of experimental data. Of these three models, AM1 was found to be the most appropriate for modelling the Si(100) surface. MNDO predicts poor Si-Si bond lengths, and the implementation of PM3 was found to give entirely unphysical results.

2.5.3 HF and DFT

Basis sets

The exact solution of the single-electron hydrogen atom is an exponential Slater-type orbital (STO), with a cusp at the position of the nucleus. However, the integrals arising from HF and DFT methods are difficult to evaluate when using exponential basis functions. For this reason, it is more common to use basis sets constructed from Gaussian functions.

Minimal basis set — STO-3G The minimal, all-electron, Gaussian basis set is *STO-3G*. Each orbital that can be doubly-occupied ($s, p_x, p_y, p_z, d_{xy}, d_{yz}, d_{xz}, d_{z^2}, d_{x^2-y^2}, ...$) is represented using a single basis function, and each basis function is a linear combination of three Gaussians (3G). The linear coefficients and Gaussian exponents are obtained by fitting the basis functions to Slater-type orbitals. The resulting basis set has two main limitations, in that all orbitals are constructed in terms of functions that describe a sphere, and that the basis functions are centred about the nucleus, in order to minimise the number of basis set parameters. A consequence of the former limitation is that the minimal basis set can yield

artificially high energies for systems in which atomic environments are far from spherical. The latter limitation implies that STO-3G can behave poorly when modelling highly delocalised systems.

Split-valence basis sets — 3-21G and 6-31G The Pople-style *split-valence* basis set addresses the first of the limitations of STO-3G. Basis sets of this type are labelled as c-$v_1v_2...v_n$G: a single basis function of c Gaussians is used to model core-level orbitals, and valence orbitals are represented using n basis functions, each of which consists of v_i Gaussians. Describing the valence orbitals in terms of multiple components allows the system to move away from spherical symmetry, enabling a more accurate description of, for example, different components of the same p orbital involved in σ- and π-bonding. Two split-valence basis sets were used in the work presented here: 3-21G and 6-31G. The linear expansion coefficients and Gaussian exponents in both of these basis sets are determined by minimisation of ground-state atomic energies from HF theory.

Polarisation basis sets — 6-31G* The nucelocentric deficiency of STO-3G can be addressed through the inclusion of *polarisation* functions in a basis set. Polarisation of an orbital can be modelled if that orbital is taken to be some function expressed in terms of a Taylor series. In practice, this is achieved through the inclusion of p-type functions in s-orbital basis functions, and d-functions in those of p-orbitals, since the first derivative of an orbital with angular momentum quantum number $l = a$ has the form of an orbital with $l = a+1$. Pople-style basis sets which include polarisation functions for p-orbitals are denoted by a single '*' (e.g. 6-31G*), and those with polarisation functions for both s- and p-orbitals by '**' (e.g. 6-31G**).

Pseudopotential basis sets — LANL2DZ A number of pseudopotential, or ECP, basis sets (section 2.4.1) were considered for this work, but only one proved to suitable for the study of organic–silicon systems: the *Los Alamos national laboratory* 2^{nd} *double-*ζ (LANL2DZ) [52,53] basis set. LANL2DZ is identical to 6-

31G for first row elements; for second row elements and beyond, core electrons are replaced with an effective core potential, and the valence electrons treated using a *double-ζ* basis set. The 'double-ζ' refers to the fact that each STO function, ζ, in the minimal STO-3G basis set is replaced by two such functions.

HF implementation and density functionals

The HF and DFT work presented here has been executed using *Q-Chem* [54]. The DFT work has involved the use of two functionals: the widely used B3LYP, and a novel functional, called EDF1.

Becke-3 Lee, Yang and Parr — B3LYP B3LYP is a combination of the *Becke three-parameter* (B3) [55] exchange and *Lee, Yang and Parr* (LYP) [56] correlation functionals. The B3 functional is a hybrid exchange functional, involving a linear combination of exchange energies from HF theory (the 'exact exchange'), the LSDA and the GGA. The LYP correlation functional is gradient corrected.

Empirical Density Functional 1 — EDF1 EDF1 [57] was developed from a linear combination of the *Becke* [33] and LYP [56] functionals, the linear coefficients of which were fitted to the G2 [58] experimental data set, using the 6-31G basis set. The fitting process resulted in the loss of the exact exchange component from HF theory; as such, EDF1 has a computational advantage over hybrid functionals such as BLYP and B3LYP. Elsewhere, it has been used to calculate atomisation energies, ionisation potentials and proton affinities for a wide range of small systems, in superior agreement with experimental results than B3LYP, when used with smaller basis sets [57, 59]. However, until this work, the performance of EDF1 in the calculation of other physio-chemical properties, such as adsorption geometry, adsorption energy and vibrational structure, had not been tested.

CHAPTER 3

Experimental techniques and materials

In this chapter, the methods and materials used in the experimental work, presented in subsequent chapters, are introduced. In particular, techniques employing synchrotron radiation are described. This is followed by discussions of the structure of various silicon surfaces, the structure of C_{60}, and the behaviour of this molecule at these surfaces.

3.1 Synchrotron Radiation

An accelerating charge produces synchrotron radiation. High-energy electrons can be contained in a storage ring, in which *bending magnets* are used to direct the electrons along a closed path. At the bending magnet, the electrons experience an acceleration and emit radiation which has a continuous spectrum and is very intense over a wide range of photon energies. In the relativistic limit, the light emitted by an accelerating charge is focused into a beam in the forward direction

of motion, with an angular extent which varies as $1/\gamma$ where

$$\gamma = \frac{1}{\sqrt{1 - \frac{v^2}{c^2}}} \tag{3.1}$$

in which v is the velocity of the charge and c is the velocity of light in a vacuum. Thus, radiation from a synchrotron light source is strongly linearly polarised in the plane of the ring. Other devices, such as *wigglers* and *undulators*, can be used to modify the path of the electrons more dramatically, producing light of a greater intensity, and may offer additional polarisation states and a high level of coherence. For example, with a helical undulator, the polarisation state of the radiation is almost entirely tunable between linear, elliptical and circular states. Finally, this light can be directed down a *beamline*, which incorporates various mirrors to direct and focus the light, and (in the energy range of interest in this thesis) some form of diffraction grating to produce highly monochromatic light with a tunable wavelength.

The variable photon energy offered by a synchrotron facility enables the use of techniques such as near-edge X-ray absorption fine structure (NEXAFS). This technique may also exploit the polarisation of synchrotron radiation in order to gain further insight into the structure of a physical system, beyond a simple picture of the overall density of states (DOS), towards information concerning the spatial distribution of those states. Other measurements, such as photoemission spectroscopy (PES), which can be carried out using monochromatic light sources (for example, He lamps and X-ray tubes), benefit greatly from the higher intensity available from synchrotron radiation. Furthermore, the fact that photon energy can be varied continuously over a given range facilitates the investigation of interesting phenomena, such as photoelectron diffraction and resonant photoemission, and enables element-specific measurements, through exploitation of the variation of photoabsorption cross-section with photon energy.

3.2 Photoemission Spectroscopy

Photoemission spectroscopy is a very powerful technique, the basis of which is the photoelectric effect. This effect was first observed in 1887 [60], but not explained until 1905 [61]. PES did not become a useful technique until the development, in the 1950s, of a spectrometer capable of resolving the kinetic energy of electrons [62].

PES can be applied to the study of gases, liquids and solids as a probe of electronic structure. Applied to surfaces, the technique can reveal information concerning the relative abundances (and, to some extent, position) of atomic species and their chemical environment, including the formation of bonds and the degree of charge transfer between species. Very high surface sensitivity can be achieved. Depending upon the choice of photon energy, PES may be referred to as ultraviolet photoemission spectroscopy (UPS), typically employed in the investigation of electronic structure in the valence band region, or X-ray photoemission spectroscopy (XPS), more useful for the study of core-level structure.

In a photoemission event, a photon of energy $h\nu$ is absorbed by an atom within the sample. The photon energy is transferred to an electron, which is excited to a higher state. If the excitation is sufficiently energetic, the electron is no longer bound to the solid and may be emitted as a photoelectron, with some definite kinetic energy, and detected at a spectrometer, or *electron analyser*. A photoelectron spectrum, or *energy distribution curve* (EDC), can be obtained by sweeping a range of kinetic energies with the electron analyser.

From this intuitive consideration of the photoemission process, it can be determined that the kinetic energy of an emitted photoelectron is given by

$$E_k = h\nu - E_B - \phi_W \tag{3.2}$$

in which E_B is the binding energy of the electron in its initial state, and ϕ_W is a constant resulting from the work function of the analyser and any applied sample–analyser bias. This may be determined from the kinetic energy cutoff, below which the analyser detects no electrons; the secondary electron background

(described below, in section 3.2.1) is useful for this purpose. In order to prevent the accumulation of charge on the sample and spectrometer, both must be grounded. They are therefore in electrical contact and , in the absence of any applied sample–analyser bias, their Fermi levels are aligned. Since energy is conserved in equation 3.2, features of the occupied density of states of the sample are reproduced in the EDC.

3.2.1 Features in a photoemission spectrum

In the simple conceptualisation given above, it is clear that the form of the EDC depends explicitly upon the energy of initial states of photoemitted electrons. When probing low binding energies, the EDC will map the occupied DOS within the valence band; at higher energies, it will contain peaks at well defined energies corresponding to the atomic orbitals of core-level electrons. The relative intensities of such peaks depend, principally, upon the relative abundance of elemental species and the probability that a photon of given energy will be absorbed, resulting in emission of a photoelectron from a particular state. This probability is quantified by the photoelectron capture cross-section, σ_c, which is specific to each energy level and element and varies with $h\nu$.

The chemical environment of an atom alters the initial state of its electrons. Any chemical interaction causes a rearrangement of electrons in the valence region and this, in turn, affects the potential experienced by core-level electrons and thereby produces a shift in the core-level energies. At a surface, reconstruction to minimise surface energy and the presence of dangling bonds result in different chemical environments, producing so-called *surface core-level shifts* (SCLS).

Effects of relaxation

Photoemission from an N electron system results in an excited $N-1$ electron system. If the photoelectron is emitted from a core-level, the excited state contains an unstable *core hole* and decays to a more stable configuration within a finite time — the *core-hole lifetime*. The energy from the decay may be emitted as a

photon, or may be transferred to an outer-level electron which is in turn emitted. The latter, non-radiative process is known as *Auger emission* and results in peaks at well-defined *kinetic* energies, which are independent of the incident photon energy. In either case, the core-hole lifetime is finite, and this causes a Lorentzain broadening of core-level peaks, arising due to the uncertainty principle.

Final state effects

The nature of the final state also affects the EDC. The most evident final state effect is that of the binding energy, which is defined as the difference between the energies of the initial N-electron and final $(N-1)$-electron states. If it can be assumed that no final-state relaxation occurs during the course of a measurement (i.e. the detection of a photoemitted electron), then Koopmans' theorem implies that the binding energy will be equal to that of the atomic, or molecular, orbital from which the photoelectron was excited. However, photoemission is a quantum-mechanical process and, as such, the nature of the final state can have a significant effect on the EDC.

The coupling of spin and orbital angular-momentum, s and l respectively, is evident in core-level spectra. After the removal of an electron from a doubly-occupied orbital, the remaining electron can adopt either a spin-up or spin-down state. The magnetic interaction of the electron's spin and orbital angular momentum lifts the orbital's degeneracy, producing multiplet terms for the different spin states, with discrete energies. Such terms are apparent in the EDC, with relative intensities proportional to their degeneracies,

$$2j + 1 \tag{3.3}$$

in which

$$j = |l + s| \tag{3.4}$$

$$s = \pm\frac{1}{2} \tag{3.5}$$

resulting in a *branching ratio* of

$$[2(|l-s|)+1] : [2(|l+s|)+1] \tag{3.6}$$

Clearly, this effect is only apparent for electronic orbitals with $l > 0$.

Further quantum-mechanical treatment of the photoemission process is possible at various levels of sophistication, resulting in a variety of descriptions of possible final states. Common to most models is the idea that final states are determined by multiple scattering of the photoelectron wavefunction. Absorption of energy from a photon excites an electron into a photoelectron state, above the Fermi level, which is delocalised across the system. The resulting wavefunction is scattered at atomic sites, and the scattered waves are in turn scattered at all other sites. Interference of these multiply scattered waves determines the amplitude of the photoelectron wavefunction at any given point, and thus determines the probability of excitation and other observables. The precise nature of the final state then depends on the assumptions used in the formalism of a particular model.

The *one-step* and *three-step* models of photoemission are the simplest quantum mechanical descriptions of the photoemission event, and employ the single-particle approximation. Essentially, this assumes that an N electron wavefunction is expressible in terms of the product of N single-electron wavefunctions. The interaction of the electronic system and the photon is then treated as a perturbation Hamiltonian due to an electromagnetic field. The result of these two approximations is that only a single electron is involved in absorption of the photon and, after excitation, that electron does not interact with the remaining $N-1$ electrons.

The one-step model considers excitation of the outgoing electron, its propagation to the surface, emission and detection as a single process, whilst the three-step model considers these stages independently. The former model is more rigorous, whilst the latter has the advantage of being physically more transparent. In these models, the probability of detecting a photoelectron with a given kinetic energy and momentum depends upon a single-electron matrix-element between

the initial and final states, clearly indicating that the EDC is dependent upon both initial and final states. Between them, these models account for effects such as the angular dependence of photoemission peak intensity and the refraction of outgoing photoelectrons at the surface of a solid. However, the use of the single particle approximation means that the results from these models become questionable in cases where the interactions of the photoelectron with the remaining bound electrons, phonons and the core-hole become large.

An alternative to the single-particle approximation is the assumption that, upon excitation, a photoelectron is immediately decoupled from the remaining $N-1$ electron system. This is known as the *sudden* approximation: the entire electronic system plays a part in photon absorption, but this absorption instantaneously creates an $N-1$ electron state, which is not necessarily an eigenstate of the Hamiltonian defining the ground state. Resulting measurements are then a projection of this state onto fully relaxed $N-1$ electron eigenstates. Again, this is not physically transparent. An analogy in terms of an addendum to the three-step model is useful: an outgoing photoelectron loses some kinetic energy in exciting some outer-level electron (*shake-up*), which may result in emission of a low-energy valence electron (*shake-off*). The result is then clear, in that additional peaks can be seen in the EDC on the lower kinetic energy side of a principal photoemission peak. It must be remembered, however, that this is only an analogy: the three-step model in no way predicts this behaviour.

More sophisticated treatments, which do not rely upon the sudden approximation, predict even more complex phenomena, connected with the dynamics of photoelectron excitation and relaxation of the system following photoemission. The only effect predicted by such treatment that is of interest here is *polarisation screening* [63]. Relaxation of an electronic system after photoemission can produce domains of electronic polarisation. The distribution of electrons within these polarised domains differs from that elsewhere, and atomic centres which are equivalent, in terms of their position in a structure, are in different screening environments. This may result in additional core-level components arising from regions of enhanced or reduced screening.

Photoelectron diffraction

Outgoing photoelectrons may be diffracted as a result of scattering by atomic centres [64, 65]. The scattered components and directly-transmitted component interfere at the point of detection; the nature of this interference (constructive or destructive) is dependent on the relative phase of these components at that point. As a result, for a fixed atomic geometry, the relative intensities of peaks in the EDC corresponding to diffracted photoelectrons may be seen to oscillate as the photon energy is varied.

Inelastic scattering

In any medium other than a perfect vacuum, photoelectrons have a finite mean free path (MFP), determined by the probability that a photoelectron will be involved in some inelastic scattering process. In the case of solids, the MFP limits the *escape depth*: the depth of material that a photoelectron can traverse before escaping the solid and being detected.

At low kinetic energies, photoelectrons have insufficient energy to excite scattering processes, and at high energies, the cross section for scattering events is low. The escape depth is therefore large at both very low and very high kinetic energies. At kinetic energies between 5 eV to 2 keV, the escape depth is sufficiently small that almost all photoelectrons emitted from a solid originate from only a few of the outermost atomic layers. As a result, PES is a highly surface sensitive technique.

Surface sensitivity can be increased by choosing experimental parameters such that the photoelectrons of interest are emitted with a kinetic energy of around 50 eV, since the escape depth from many materials demonstrates a minimum at this energy. Alternatively, surface sensitivity can be altered by adjusting the experimental geometry. In order to maximise the count rate and improve signal to noise ratio, it is usual to position the sample such that the analyser detects photoelectrons which leave the solid normal to the surface: the *normal emission* geometry. If the sample is rotated away from normal emission, the depth of

material between the analyser and a given point within the sample is increased. The signal from deeper layers is attenuated and surface sensitivity increased, at the expense of overall count rate. When the emission angle is far from normal, the experimental geometry is described as *grazing emission*.

In addition to limiting the escape depth, inelastic scattering events can cause the liberation of valence electrons from participating atoms. These *secondary electrons* can undergo further scattering, and invariably some escape the sample and are detected, producing a broad background upon which all other features of the EDC are superposed. The secondary-electron yield at a particular energy is dependent on the inelastic scattering, and therefore availability, of primary electrons of higher kinetic energy. Thus, the secondary electron background makes little contribution to an EDC at high kinetic energies, but may dominate the spectrum at lower energies.

3.2.2 Analysis of photoemission spectra

A kinetic energy spectrum can expressed in terms of binding energy through the use of a suitable energy reference. It is typical to use the Fermi edge of a metallic part of the sample holder. If this can not be observed at a certain photon energy, then a core-level peak can usually be aligned to a measurement of the same core level at a different photon energy, at which the Fermi edge can be observed.

Background subtraction

The secondary electron background must be taken into account, otherwise relative peak areas may be incorrect as the background contributes more strongly at lower kinetic energies than at higher. Within the region of a peak, the background increases in a smooth step, described as a *Shirley background*, which can be estimated using an iterative numerical technique involving the original data [66].

It has been observed here that subtraction of the resulting background alone may sometimes be insufficient: in some cases, there remains a smoothly varying gradient, which steadily increases from higher to lower kinetic energy. The gradi-

ent can be eliminated through the use of a different style of background function. This function consists of the sum of a proportion of the Shirley line shape, evaluated across the entire range of the experimental data, and a polynomial of order three, the parameters of which are chosen to match the *gradient* of the raw data far from photoemission peaks.

During the course of this work, it has been observed that the gradient remaining after subtraction of an approximated Shirley background can cause difficulties in obtaining physically meaningful results during subsequent stages of data analysis. When the alternative background function is used, and the gradient eliminated, meaningful results can be obtained far more readily. This suggests that the gradient is inherent to the background, rather than some other physical effect, and remains, in the former case, due to poor background treatment: the secondary electron background at a given energy depends upon the intensity of *primary* photoelectrons at *all* higher kinetic energies; the numerical approximation to the Shirley background, however, relies upon original data in the spectrum, and this only covers a finite range of energies and includes secondary electrons. The result is that the residual gradient is far more severe in spectra obtained at lower kinetic energies.

Core-level fitting

Core-level spectra contain many contributions arising from shifts due to different chemical environments in the bulk, at surface reconstructions and in the presence of adsorbates. These contributions may be complicated due to effects such as spin-orbit splitting but, given sufficiently high experimental resolution, decomposition into a number of components is possible. This decomposition is achieved through curve fitting, after subtraction of the secondary electron background, but the model function must be physically reasonable if the results are to be meaningful.

For semiconductors and insulators, each component in a core-level spectrum has a Lorentzian spectral form of finite width, due to the finite lifetime of the core-hole produced by photoionisation. For metals, additional excitations lead to

an asymmetric line shape, but such details are beyond the scope of this work. Thermal effects, such as local interactions of the electronic system with phonons, can also broaden discrete initial states into a Gaussian distribution. Furthermore, the characteristics of the apparatus used to obtain the spectrum cause additional broadening, arising from imperfect monochromatisation and a finite electron analyser resolution, which may also be described by a Gaussian function. Each component in a core-level spectrum is, therefore, a convolution of the intrinsic Lorentzian form of the spectral function with a Gaussian function, modelling thermal and instrumental broadening. The result of such a convolution is a Voigt function, which can be defined in terms of its position E, intensity I, Lorentzian width Γ_L, and Gaussian width Γ_G.

The fitting function for a core-level photoemission spectrum consists of a sum of one Voigt function for each component. For even simple systems, spin-orbit splitting and the presence of bulk and surface components can lead to a large number of fitting parameters. This is not useful, as a large parameter space can lead to fits which have very low residuals whilst having only a tenuous physical basis. Physical considerations can be employed to reduce the number of truly distinct parameters.

Certain physical properties can be determined by independent means, with a high level of confidence. These include: core-hole lifetimes, and therefrom the Lorentzian spectral widths; the energy separation between multiplet terms within a core-level (the *spin-orbit split*); the degeneracy of those multiplet terms, and thence the relationship between their intensities (described by the *branching ratio*). Lorentzian widths can be fixed in the fitting process, or at least tightly constrained, and the positions and intensities of multiplet terms expressed in reference to the position and intensity of some (arbitrarily chosen) primary term. Furthermore, it can be expected that the multiplet terms of a single core-level component will share common Gaussian and Lorentzian widths.

These considerations may result in a significant reduction in the number of explicit fit parameters, but this is rarely sufficient to ensure that the results of a fit are physically reasonable. The parameter space may be further reduced by

the imposition of reasonable limits on individual parameters. Estimates for core-level shifts, and even Gaussian widths, can be obtained by reference to studies of systems with similar features, and confidence in those estimates increases with the simplicity of the reference systems.

Even so, the reliability of a fit may be questionable. There are a number of factors that may indicate an unreliable or unphysical fit: the irreproducibility of a fit; excessively large peak widths; core-level shifts smaller than the limit of experimental resolution; the convergence of multiple parameters to hard limits. Essentially, great care must be taken when interpreting the results of a curve fit to a core-level spectrum, as the quality of a fit can not be judged from the fit residuals alone. That having been said, if due care is taken, decomposition through curve-fitting can give useful insights into the physics and chemistry of a system.

Analysis of photoemission spectra presented in this work was carried out using Wavemetrics' *Igor Pro*. Code was specifically written to simplify the fitting process, in particular the manipulation of fit parameters and their limits

3.3 Near edge X-ray absorption fine structure

Near edge X-ray absorption fine structure (NEXAFS), otherwise known as X-ray absorption near edge structure (XANES), is another technique which employs synchrotron radiation to probe electronic structure. The technique relies upon the variability of photon energy, as X-ray absorption is measured as a function of the photon energy. The resulting spectrum contains various resonances, at energies where the absorption of photons is just sufficient to excite a core-level electron to some empty state, just above the Fermi level.

X-ray absorption may be measured directly, by detecting the transmitted radiation. However, this approach requires samples in the form of very thin foils, and X-ray scattering, due to effects such as diffraction, can contribute significantly to results and prove problematic: the separation of scattering-related contributions and those due to electronic excitations may be difficult to distinguish. Further-

more, transmission measurements are sensitive to processes occurring throughout the extent of the sample in the direction of X-ray propagation, and are therefore not appropriate to the study of surfaces.

The excited state created by photon adsorption is unstable, and will undergo some decay process, for example, spectator- or observer-Auger decay (the latter is schematically illustrated in figure 3.1). A photoelectron spectrometer, or electron analyser, can be used to measure the flux of electrons emitted from a particular Auger process. The variation of this flux with photon energy gives a direct measure of the variation in X-ray absorption. However, detection in this manner is critical on the correct selection of the photoelectron energy that is monitored. Furthermore, the acceptance solid-angle of photoelectron analysers is typically quite small, which can result in a poor ratio of signal to noise.

A proportion of outgoing electrons from an Auger decay process will undergo inelastic scattering, producing a cascade of secondary photoelectrons with lower kinetic energies. These may be detected using a total electron yield (TEY) detector, or partial yield detector (PYD). The secondary photoelectrons dominate the signal obtained with such a detector, and originate from some average depth into the sample. The PYD offers the benefit that, to a certain extent, surface sensitivity may be increased by rasing the low energy cutoff, as lower energy

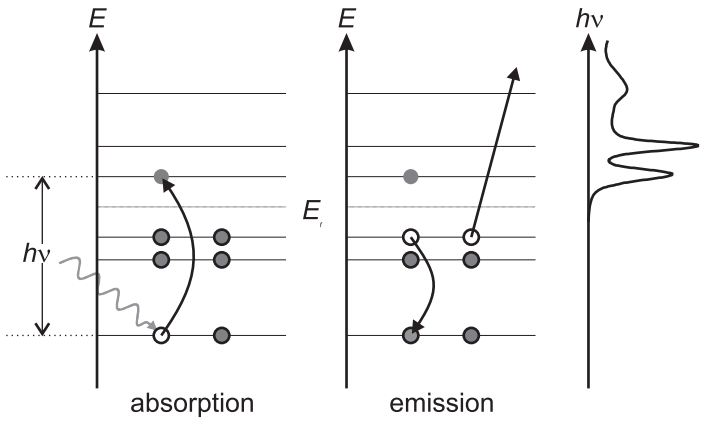

FIGURE 3.1: A schematic illustration of NEXAFS measurement by detection of Auger electrons, emitted as a result of X-ray absorption.

secondary-electrons generally originate from deeper within the sample.

3.3.1 Typical form of a NEXAFS spectrum

In contrast to spectra obtained using PES, those obtained via NEXAFS primarily contain information concerning unfilled electronic orbitals within a system. It is important to understand, however, that the unfilled orbitals probed by NEXAFS are those of an excited state, due to the presence of the core hole — they are not identical to those available in the system's ground state. Typically, the unoccupied orbitals of the excited state are similar to those of the ground state, but orbital energies are shifted slightly. A full excursus of this matter, and of the theory underlying NEXAFS, is unnecessary here; treatment of such issues can be found in reference books, of which [67] is an excellent example. A brief discussion of the origins of spectral features follows.

For monatomic systems, the consideration of aspects of the electronic structure that produce spectral features is quite straightforward, and is illustrated in figure 3.2. X-ray absorption increases when the photon energy is equal to the separation between a core level and some unoccupied state (in the monatomic case, some Rydberg state). Above a particular photon energy, the core-level electron will be excited into a state within the continuum above the vacuum level. The spectrum therefore consists of a series of resonances followed by a step-like

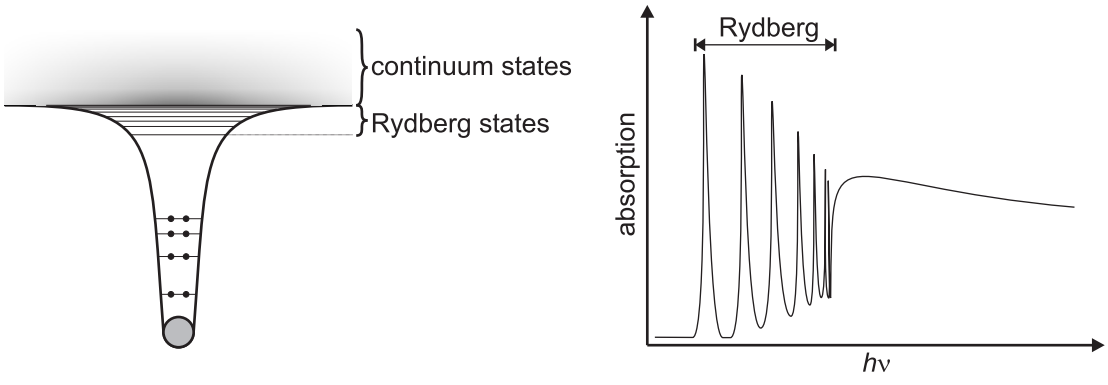

FIGURE 3.2: The electronic structure and NEXAFS spectrum of a model monatomic system.

increase.

For di- and polyatomic systems, the presence of multiple nuclei complicates the electronic potential surface, introducing centrifugal barriers between multiple potential wells and delocalised MOs. The model situation for a diatomic molecule is illustrated in figure 3.3. In the ground state, unfilled π^* and σ^* MOs lie above the vacuum level. After excitation of a core-level electron, however, lower-energy π^* orbital energies are typically pulled below the vacuum level due to the presence of the core hole. Higher-energy σ^* states may still reside within the continuum above the vacuum level, but are stabilised by the presence of the centrifugal potential barrier. The NEXAFS spectrum for such a system includes sharp resonances, corresponding to the excitation of electrons from a core-level to the π^* states, and broader σ^* resonances. The broadness of σ^* resonances can be attributed to at least two physical causes. Firstly, since these states lie above the vacuum level, an occupying electron can readily decay into some continuum state, giving a short σ^* lifetime and therefore large width. Secondly, σ^* orbitals are oriented along internuclear axes, and are therefore particularly sensitive to variations in internuclear separation; the motion of nuclei in molecular vibrational modes occurs on a time scale which is much shorter than the electronic excitation process, and thus the σ^* resonance in a NEXAFS spectrum is a result of sampling various internuclear separations.

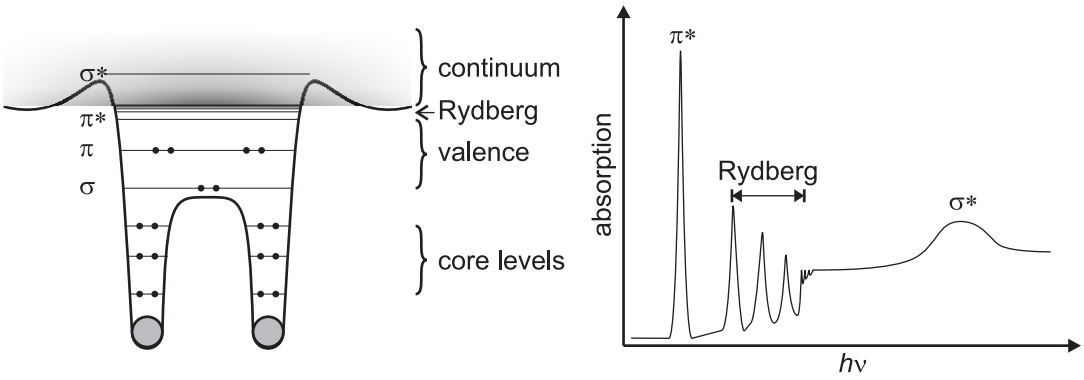

FIGURE 3.3: The electronic structure and NEXAFS spectrum of a model diatomic system.

Additional features may also appear in a NEXAFS spectrum, such as shake-up and shake-off satellites and other multi-electron excitations. Details of such excitations are beyond the scope of the work presented here, but may be found elsewhere (see [68] and references therein) .

A particularly powerful aspect of NEXAFS spectroscopy is the ability to exploit the linear-polarisation of synchrotron light obtained from bending magnets. In such radiation, the direction of the electric field is well defined and, by adjusting the experimental geometry, the degree of overlap between the electric field vector and particular orbitals can be modified. As this overlap increases, the intensities of resonances related to that orbital will also increase, relative to other resonances in the spectrum, reaching a maximum when the electric field vector and orbital are well aligned. It is therefore possible to determine the orientation of non-spherical orbitals, of bonds and hence of adsorbates at a surface. However, this capability is not particularly useful when applied to the study of fullerenes, due to their high symmetry and lack of variety in the constituent elements.

3.4 Experimental systems

All of the data obtained via PES and NEXAFS spectroscopy presented in this thesis were obtained using the UK synchrotron radiation source, at Daresbury Laboratory. A number of beamlines were employed, and a brief description of each facility follows.

3.4.1 Beamline 4.1

Beamline 4.1 [69] is situated on bending magnet 4 of the Daresbury SRS. The beamline uses a grazing-incidence, spherical-grating monochromator, which has three interchangeable gratings, manufactured from Au-coated quartz, offering photon energy ranges of 15–45 eV, 45 –130 eV and 130–220 eV. The monochromator has both entrance and exit slits, the former to minimise the footprint of the incident beam on the monochromator, and the latter to control the spectral resolution of the beam incident at the sample. Beam focusing is achieved using

three mirrors. Two of these lie before the monochromator, and decouple the focusing action into the horizontal and vertical directions. A post-monochromator mirror allows for small focusing adjustments. All mirrors are manufactured from Pt-coated Glidcop (dispersion-strengthened Cu). Baffles along the length of the beamline also allow limitation of the photon flux and, to a lesser extent, spot size.

The beamline has a fixed ultra-high vacuum (UHV) end-station, pumped using turbo-molecular pumps. The chamber features an ion source for sample sputtering, ablation and the deposition of gases, LEED optics, a He lamp, a Mg-k_α X-ray source, a sample transfer system with fast-entry load lock, a cold trap, a mass spectrometer for residual gas analysis (RGA), a Scienta SES200 hemispherical electron analyser and, more recently, a VG Clam analyser. Two sample manipulators are available for use with the end station. The first offers four degrees of freedom (translation along x and y, in the plane of the incident beam, along z, perpendicular to the xy plane, and rotation about z) and resistive-heating of the sample through the direct application of current. The second manipulator offers motion along the x, y and z axes, rotation about z and azimuthal orientation control, and facilitates sample annealing via electron-beam heating.

Given the photon energy range available, the beamline is suitable for photoemission studies of the valence band region and shallow core-levels. In addition, the beamline may used for studies of circular dichorism, exploiting the circularly polarised nature of light from the bending magnet above and below the plane of the stored electron beam. For photoemission measurements, the equipment on the beamline affords an overall experimental resolution of, typically, 200 meV; this value is subject to a significant increase, however, when working at the limits of the photon energy ranges provided by each diffraction grating.

3.4.2 Beamline 5u1

Synchrotron radiation on beamline 5u1 [70, 71] is obtained using a 1 metre, ten period, variable gap, permanent magnet undulator. When set to the minimum

gap width, the undulator produces a fundamental synchrotron resonance at 60 eV. Higher harmonics and the variability of the undulator gap result in a quasi-continuous spectrum up to around 2 keV. Light from the undulator passes directly to the monochromator (there are no entrance slits), which consists of a plane mirror and plane diffraction grating, followed by a spherical mirror. All elements within the monochromator are manufactured from Pt-coated SiC films, deposited by chemical vapour deposition onto a graphite substrate. The energy of outgoing photons is determined by the orientation of the plane mirror and diffraction grating; the spherical mirror focuses light onto the monochromator exit slits. Finally, an ellipsoidal mirror directs and focuses the beam into an experimental chamber.

It is worthy of note that, due to the lack of monochromator entrance slits, the resolution of outgoing light is critically dependent upon the degree of extension of the source, i.e. the vertical height of the electron beam within the storage ring. The lack of entrance slits also poses an additional problem: should there be problems with beam steering, resulting in the vertical displacement of the stored electron beam, the area over which light is incident at the diffraction grating may change dramatically, thus producing significant variation in photon energy. For this reason, the necessity for the acquisition of regular energy references when using beamline 5u1 can not be understated.

Beamline 5u1 does not have a fixed end-station, since the large photon energy range and high flux mean that the line is suitable for use as a light source for a variety of very different experimental techniques. A number of experimental chambers that are compatible with this beamline exist; all measurements presented here that were carried out on beamline 5u1 were executed using the Daresbury laboratories surface science group's SURF1 end station. In its standard configuration, this chamber includes LEED optics, an electron gun, an ion source, RGA system, cold trap and a VG omniax manipulator. Several modifications to this standard configuration were used in obtaining the data presented here. The standard manipulator enables sample heating using a thermal-electron beam; however, in the investigations presented here, a replacement was used, offering direct sample heating and four degrees of freedom (as per the direct

heating manipulator described in described in section 3.4.1). Additions to the experimental chamber included a fast-entry load lock to allow sample transfer, a 120 mm hemispherical electron analyser from PSP [72], used for photoemission measurements, and a TEY detector for NEXAFS measurements.

3.4.3 Beamline MPW 6.1

Beamline MPW 6.1 [73] is based on a multipole wiggler insertion device, providing photons of energies from 40 eV to 500 eV. The layout is similar to that of beamline 4.1. Two mirrors, manufactured from Au-coated silicon, are responsible for the horizontal and vertical deflection and focusing of light from the insertion device onto the monochromator entrance slits. The monochromator contains three gratings, which operate in the ranges of 40–80 eV, 80–160 eV and 160–320 eV. The gratings are based on fused silica substrates; the two lower-energy gratings are coated with Au, whilst the high-energy grating uses Ni. After monochromatisation, the light passes through exit slits and onto a final deflection and post-focusing mirror. All mirrors in the beamline are Au-coated fused silica.

As for beamline 5u1, MPW 6.1 has no fixed end station. Work presented here was obtained using the Daresbury laboratory / UMIST [1] ARUPS10 chamber, equipped with LEED optics, ion source, VG omniax manipulator offering resistive heating, sample transfer system, RGA system and an in-chamber hemispherical electron analyser, mounted on a two-axis goniometer.

3.5 Silicon surfaces

Silicon is a group IV metalloid, with electronic configuration [Ne].$3s^2.3p^2$ in the atomic form. This element is highly abundant, constituting approximately 25 % of the Earth's crust, and is commonly found in the form of SiO_2.

Single crystals of silicon can be grown by the Czochralski technique. The bulk material has a diamond-lattice crystal structure: a face-centred cubic lattice with a two-membered primitive unit cell, such that each silicon centre is tetrahedrally

[1] University of Manchester Institute of Science and Technology

Property	Value	Unit
Atomic mass	28.0755	
Melting point	1414	°C
Boiling point	3265	°C
Density	2.33	g / cm^3
Covalent Radius	1.11	Å

TABLE 3.1: Properties of silicon at room temperature and atmospheric pressure.

bonded to four neighbours. The valence band is formed from the combination of the occupied $3s$ and $3p$ states, and the conduction band from the unoccupied $3p$ and $4s$ states, with an indirect band gap of 1.12 eV. Other properties of silicon are summarised in table 3.1.

Cleaving a bulk silicon crystal to expose a low-index surface reveals unfilled valances, or *dangling bonds*, and therefore a highly reactive surface. Under atmospheric conditions, such surfaces react readily with available oxygen, producing a layer of native oxide. Under UHV conditions, this oxide can be thermally removed; surface reconstruction then occurs in order to minimise the number of dangling bonds and lower the surface free energy. Two reconstructions of the clean Si surface have been used in this work, namely Si(100)–(2×1) and Si(111)–(7×7), in addition to the less reactive Ag:Si(111)–$(\sqrt{3} \times \sqrt{3})$R30° surface.

3.5.1 Si(111)–(7×7)

The Si(111)–(7×7) reconstruction has a complicated geometry involving a large unit cell. STM images and PES reveal much about the surface which is consistent with the *dimer adatom stacking-fault* (DAS) model [74], shown schematically in figure 3.4. The topmost layer of this reconstruction consists of twelve *adatoms*, each of which is bound to three atoms in the second layer, resulting in one partially filled dangling bond per adatom. The second layer contains 42 atoms, six of which are triply co-ordinated *rest atoms*. The remainder form dimers surrounding the triangular adatom subunits. Below this lies a silicon bilayer, with the same structure as the (1×1) bulk termination. Vacancies exist at the corners of the unit cell. These *corner holes* contain one dangling bond from the Si bilayer.

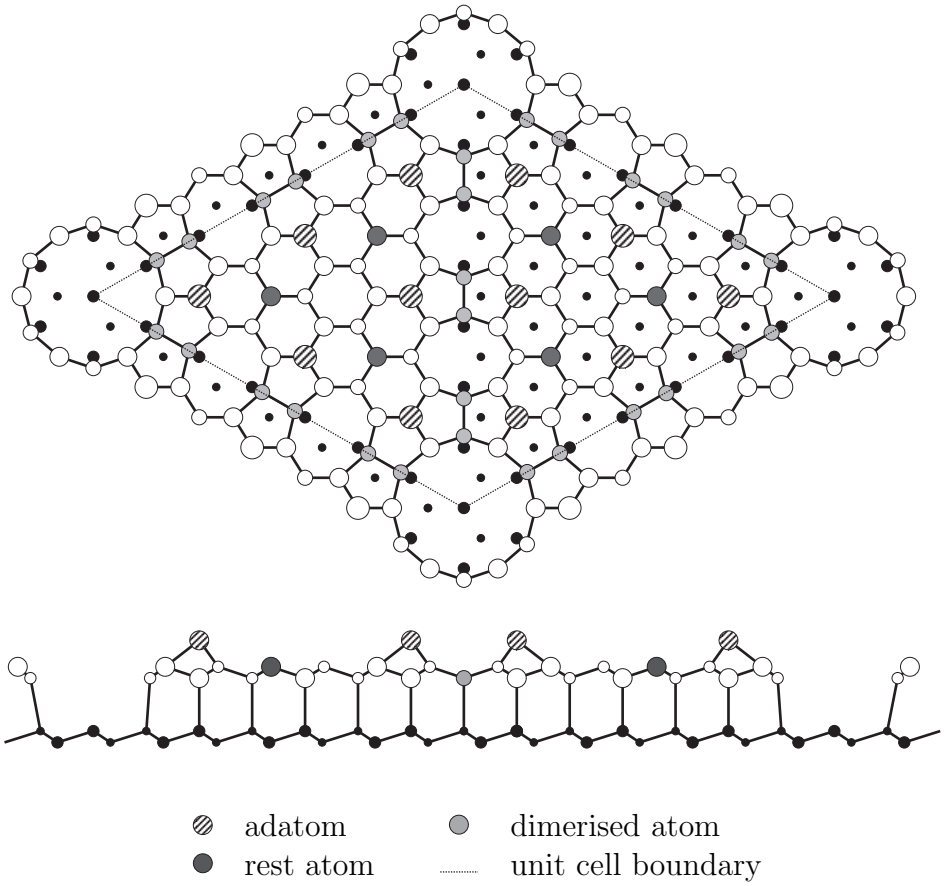

FIGURE 3.4: The dimer adatom stacking (DAS) model of the Si(111)–(7 × 7) reconstruction, after [74].

Each unit cell of the (7 × 7) reconstruction contains nineteen dangling bonds, which is a significant reduction from the 49 that exist on an equivalent area of the unreconstructed surface.

The DAS model contains a stacking fault in one half of the unit cell. This can be seen clearly in the schematic. The right-hand half of the unit cell is unfaulted: atoms are stacked regularly, such that the first atom directly beneath an adatom resides in the fourth layer. Conversely, the stacking fault in the left-hand half of the unit cell results in second-layer atoms lying directly beneath adatoms.

Experimentally, the Si(111)–(7 × 7) reconstruction can be produced by flash-annealing to 1200°C under UHV conditions. As the surface cools, it undergoes a phase transition at around 860°C from the unreconstructed (1 × 1) termination to

the (7×7) reconstruction. After preparation of the surface in this manner, both filled- and empty-state STM images show twelve protrusions and one depression per unit cell. The protrusions correspond to the dangling bonds on adatoms, visible in both imaging modes since they are partially filled. The depression corresponds to the corner hole. Additionally, in the filled-state image, one half of each unit cell appears to be lower than the other. This can be attributed to the presence of the stacking fault.

Measurements from scanning tunnelling spectroscopy and valence band photoemission indicate that the Si(111)–(7×7) surface is metallic in character [78]. A valence band spectrum for this surface is shown on the right hand side of figure 3.5. A state exists close to the Fermi edge, and this is associated with the (7×7) reconstruction adatoms. The Si $2p$ core-level spectrum is shown on the left hand side of figure 3.5, along with a deconvolution into six components, which are clearly apparent in high resolution, low temperature measurements carried out elsewhere [77, 79]. The strongest component in the bulk-sensitive, normal-

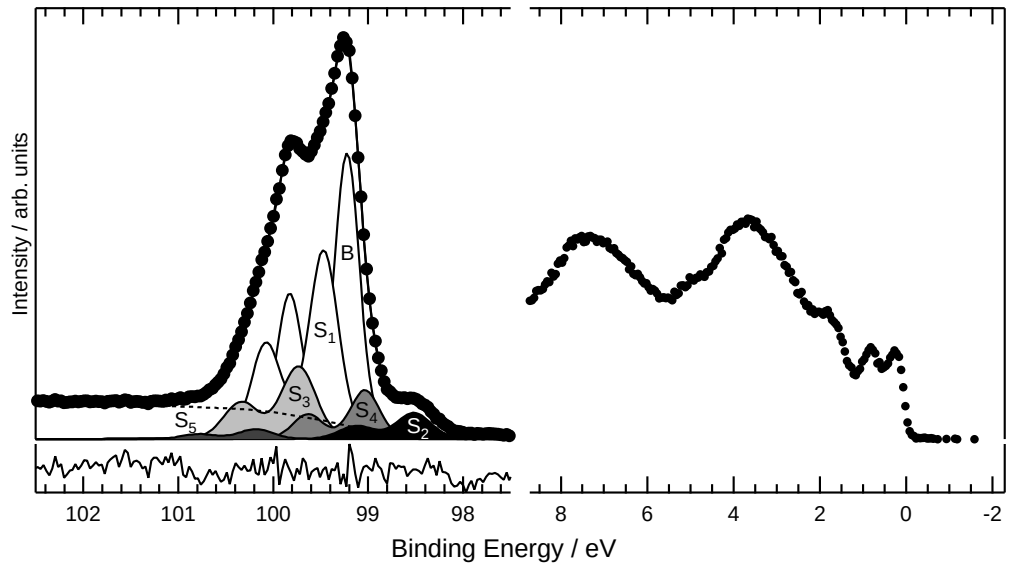

FIGURE 3.5: Si $2p$ core-level (left) and valence band (right) photoemission spectra for the Si(111)–(7×7) surface, obtained using $h\nu = 140$ and $h\nu = 21.2$ eV. The core-level has been decomposed into six components, after [75–77]; the residual trace has been expanded by a factor of 10^3.

emission spectrum (labelled B in figure 3.5) is due to bulk silicon; those labelled S_1 to S_4 correspond directly to elements of the DAS model (pedestal atoms, rest atoms, adatoms and second-layer atoms, respectively), whilst S_5 is attributed to surface defects, such as vacancies and step edges. Both the adatom feature, in the valence band, and rest-atom state, in the core-level spectrum, disappear with only a small amount of surface contamination. As such, these features provide a useful guide for gauging the quality of the surface reconstruction during PES experiments.

3.5.2 Si(100)–(2×1)

The Si(100) surface is of great technological importance, since it the most commonly used surface in device fabrication. The unreconstructed surface consists of equivalent atoms, each of which is bound to two subsurface atoms and possesses two dangling bonds. The surface can undergo reconstruction to either a (2×1) or $c(4 \times 2)$ structure. The unreconstructed surface, (2×1) and $c(4 \times 2)$ reconstructions are shown schematically in figure 3.6.

In the (2×1) reconstruction, adjacent surface atoms dimerise to tie up two of the dangling bonds, with a single partially-filled dangling bond remaining on each surface atom. The dimers align to form *dimer rows*, which run perpendicular to

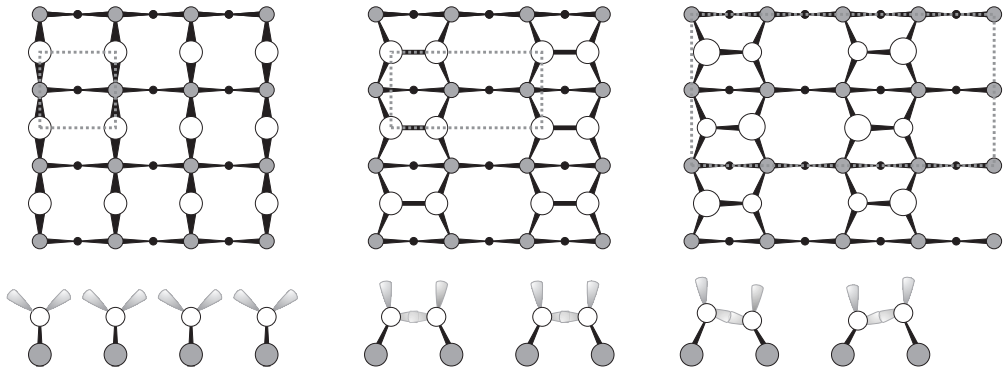

FIGURE 3.6: Reconstructions of the Si(100) surface. In each case, the surface unit cell is indicated by a broken line.

the dimer bond direction. Terraces are common on Si(100) surfaces, with a step height of $a_0/4$ (1.36 Å), and dimer rows on the upper terrace run perpendicularly to those on the lower. The presence of dimer rows and the fact that they change direction from one terrace to the next enables the formation of two types of step edge. If the dimer rows on the upper terrace run parallel to the step edge, then the edge is smooth. Alternatively, if the dimer rows on the upper terrace run perpendicular to the step edge, then the edge is rougher and less stable.

The $c(4 \times 2)$ reconstruction is similar to the (2×1). Surface atoms dimerise and align to form dimer rows, but a Jahn-Teller distortion results in buckled dimers, in which there is a partial charge-transfer from the lower to the upper dimer member. Adjacent dimers buckle in an anti-correlated manner, possibly to reduce surface strain.

Experimentally, the Si(100) surface can be made to undergo reconstruction through a similar thermal flash-annealing process used to bring about the Si(111)–(7×7) surface reconstruction. STM images after such treatment clearly show the

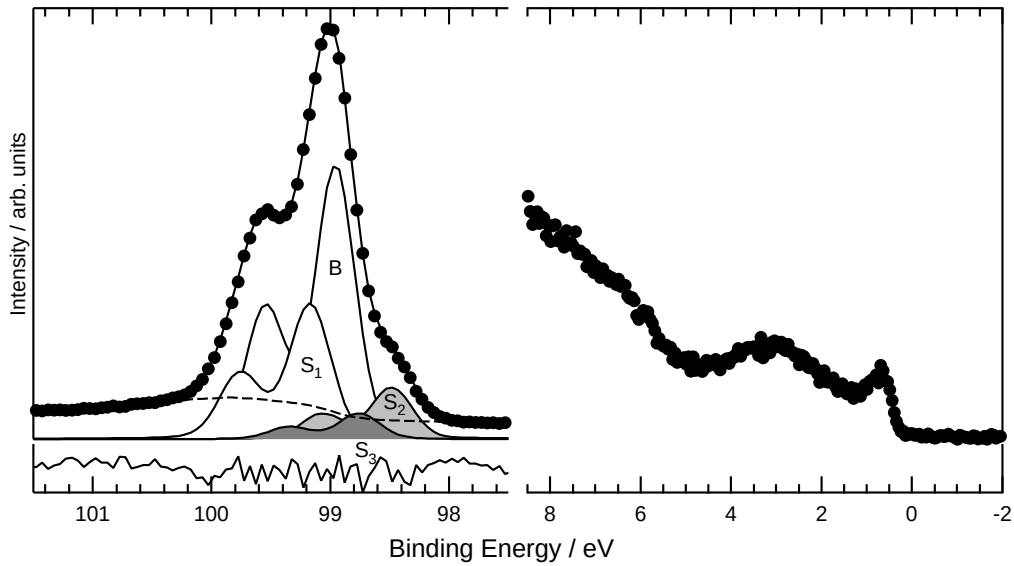

FIGURE 3.7: Si $2p$ core-level (left) and valence band (right) photoemission spectra for the Si(100) surface, obtained using $h\nu = 140$ and $h\nu = 21.2$ eV. The core-level has been decomposed into four components, and the residual trace expanded by a factor of 10^3.

surface dimers, dimer rows, rough and smooth terrace steps and the change in dimer row orientation from one terrace to the next. Additionally, both symmetric and buckled dimers can be seen. Core-level and valence-band photoemission spectra for the reconstructed (100) surface are shown in figure 3.7. A dimer-related surface state lies close to the Fermi edge. The core-level deconvolution presented here shows four discrete components. The dominant component is due to bulk silicon. Other components, the positions of which are given in brackets as relative binding energies (RBE) with respect to the bulk line, correspond to dimer states (-0.45 eV), second-layer atoms (+0.45 eV), and a combination of third-layer atoms and surface defects (-0.2 eV) [80]. A fifth core-level component with a RBE of +0.06 eV has been observed, but can not be resolved from the bulk line in figure 3.7. This fifth component is also related to dimer states. The presence of two dimer-related components is attributed to the presence of buckled dimers: the component with a small, positive shift corresponds to the 'up' atoms in such dimers, and that with a negative shift to 'down' atoms; the charge transfer from the lower to upper atom is responsible for the significant separation of these two components.

Dimer buckling

The presence of buckled dimers at the reconstructed Si(100) surface is an issue subject to considerable controversy. Theoretical investigations have provided mixed results concerning the ground state structure of this surface [81–86] . Some calculations predict that a symmetric dimer (2×1) geometry is more stable, whilst others favour the buckled dimer and therefore the $c(4 \times 2)$ reconstruction. It is not clear which calculations are more reliable, and the controversy surrounding theoretical treatment of this issue is compounded by the fact that the stability of one state over the other can depend critically on the choice of physical constraints used in the calculation [87].

It has been suggested that the presence of buckled dimers in STM images is an artefact of the technique. However, as discussed, various components in

the Si 2*p* core-level spectrum from PES have been attributed to the 'up'- and 'down'-atoms in a buckled dimer, ruling out the possibility that buckled dimers arise solely due to a tip–sample interaction in STM.

An alternative suggestion is that the room temperature state of the (100) surface consists of buckled dimers, but that these dimers oscillate between the two possible buckled states at a frequency of the order of 5 THz [88], i.e. on the femtosecond timescale. If this oscillation occurs on a timescale much less than that associated with a particular measurement technique, the technique will give a time-averaged measurement. STM samples the surface at the millisecond timescale, producing a time-averaged image of the dimers which therefore appear symmetric. This is supported by the fact that buckled dimers in room-temperature STM images appear near defect or adsorption sites, which may pin the dimers into one buckled state. Furthermore, low temperature STM and LEED studies have shown that the c(4×2) reconstruction is dominant at temperatures below 200 K [89]. It is possible that the oscillation of buckled dimers is frozen out at such temperatures, due to insufficient thermal energy to overcome the barrier between the two buckled states. This model is currently widely accepted.

The characteristic lifetime of a photoionisiation event followed by subsequent core-hole relaxation is typically of the order of femtoseconds. Thus, the the possibility of time averaging in PES and NEXAFS measurements is not so certain. However, the component with a RBE of -0.25 eV in the Si(100)–(2×1) Si 2*p* core-level spectrum may incorporate some intermediate dimer-atom states, as it lies half way between the up- and down-atom states. The implications of dimer buckling for theoretical investigations will be discussed in the relevant chapter.

3.5.3 Ag:Si(111)–$(\sqrt{3} \times \sqrt{3})$R30°

The Ag:Si(111)–$(\sqrt{3} \times \sqrt{3})$R30° reconstructed surface can be prepared by depositing Ag onto a clean Si(111)–(7×7) surface held at around 450°C. STM reveals the real-space structure of the Ag:Si(111)–$(\sqrt{3} \times \sqrt{3})$R30° reconstruction as a honeycomb structure, and the honeycomb-chain-trimer (HCT) model [90] has

become the accepted model of this reconstruction. A schematic representation of this model is given in figure 3.8.

Within the unit cell of the HCT model, Ag and Si trimers are formed, such that the former surround the latter in a hexagonal ring. Ag trimers are situated above second-layer Si atoms, and each Ag atom participates in bonding to a member of a Si trimer. In this reconstruction, Ag atoms occupy all Si dangling bonds, with the exception of those formed at step edges and the boundaries between different phases of the reconstruction, resulting in a much lower reactivity than that of the Si(111)–(7×7) surface.

The valence band and Si $2p$ core-level spectra obtained from the Ag:Si(111)–$(\sqrt{3} \times \sqrt{3})$R30° surface are given in figure 3.9. A decomposition of the core-level spectrum is not given, as it beyond the scope of the work presented here. High-resolution PES studies of this surface, however, reveal the presence of five components in the Si $2p$ core level, corresponding to bulk Si, Si atoms in the trimers bound to Ag at the surface, second-layer atoms, Si in a buckled third layer, and a small contribution associated with the formation of islands of excess Ag [91].

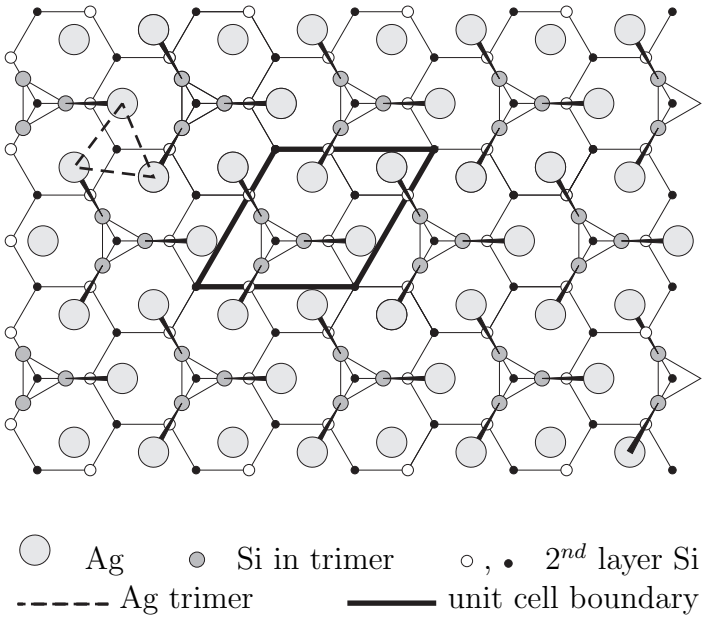

FIGURE 3.8: The honeycomb-chain-trimer (HCT) model of the Ag:Si(111)–$(\sqrt{3} \times \sqrt{3})$R30° reconstruction, after [90].

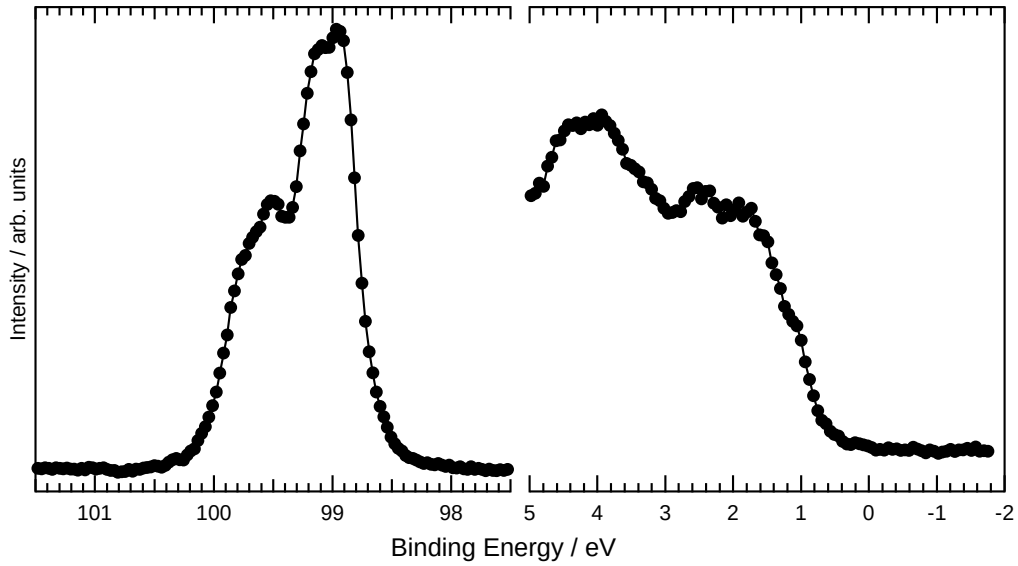

FIGURE 3.9: Si $2p$ core-level (left) and valence band (right) photoemission spectra for the Ag:Si(111)–($\sqrt{3} \times \sqrt{3}$)R30° surface, obtained using $h\nu = 140$ eV and $h\nu = 21.2$ eV.

The two dominant components are those arising from the bulk and the Si trimers: the intensity of these two components is similar, and they are separated by around 0.35 eV, resulting in the characteristic shape of the Ag:Si(111)–($\sqrt{3} \times \sqrt{3}$)R30° Si $2p$ core-level spectrum.

3.6 C_{60}

C_{60} is a 60-membered carbon cage, with icosahedral symmetry. Its structure is shown in figure 3.10, and consists of twelve pentagonal and sixteen hexagonal faces, with C atoms at the vertexes. The electronic structure of C_{60} is illustrated schematically in figure 3.11. 120 electrons occupy localised carbon core levels. The remaining 240 valence electrons are responsible for covalent bonding within the cage, and occupy a number of delocalised molecular orbitals of varying degeneracy. The character of this bonding lies somewhere between sp^2 and sp^3. In a carbon centre involved in covalent bonding to three neighbours, two $2p$ orbitals interact with the $2s$ orbital to produce three sp^2 hybridised orbitals lying in a

plane, with an angular separation of 120°. However, the curvature of the bonding system in C_{60} brings about sp^3 character.

The lowest unoccupied molecular orbital (LUMO), highest occupied molecular orbital (HOMO) and next-highest occupied molecular orbital (HOMO−1) are each 3–, 5– and 9–fold degenerate, accommodating 6, 10 and 18 electrons, respectively. In an isolated C_{60} molecule, the HOMO–LUMO gap is around 1.9 eV. In bulk C_{60}, however, formation of conduction and valence bands occurs, with a band gap of around 1.6 eV, resulting in an intrinsic semiconductor. The valence band of bulk-like C_{60} (a thick film deposited onto an Si(111)–(7×7) surface until the Si $2p$ core level can no longer be observed at $h\nu = 140$ eV) is shown in figure 3.12.

3.6.1 C_{60} at silicon surfaces

There is some debate as to whether deposition of C_{60} onto the Si(111)–(7×7) and Si(100)–(2×1) surfaces results in chemisorption or physisorption of the first monolayer [92–102] . It is generally accepted that further layers are weakly physisorbed, and can be desorbed by annealing a multilayer sample to around 300°C. A chemisorbed monolayer remains, either because this layer is chemisorbed before annealing, or covalent bonds are formed during annealing.

Under UHV conditions, C_{60} can be deposited from a Knudsen cell or tantalum envelope heated to a temperature above 350°C. At a given photon energy, the C $1s$ to Si $2p$ core-level ratio increases with C_{60} coverage. After obtaining this ratio

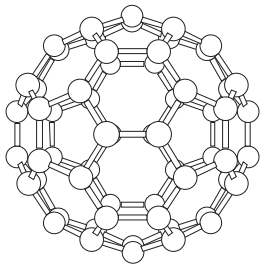

FIGURE 3.10: The geometric structure of C_{60}.

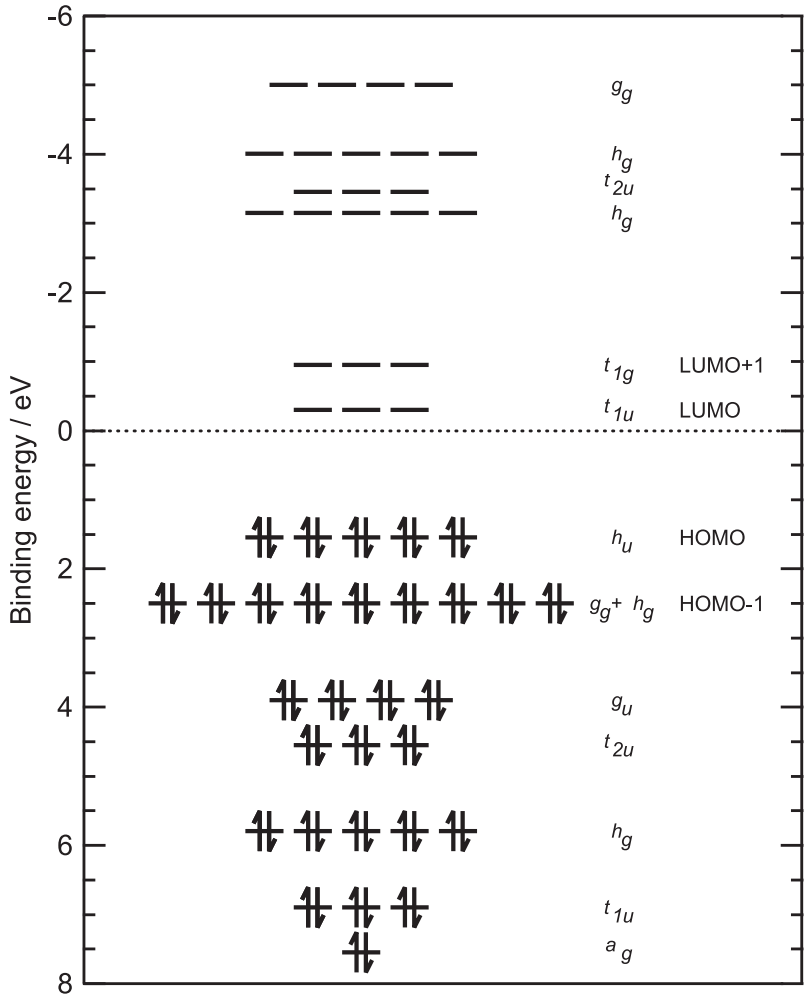

FIGURE 3.11: The electronic structure of C_{60}, with the symmetry of each level indicated using Mulliken symbols. The first and second of each of the highest occupied and lowest unoccupied orbitals are also labelled.

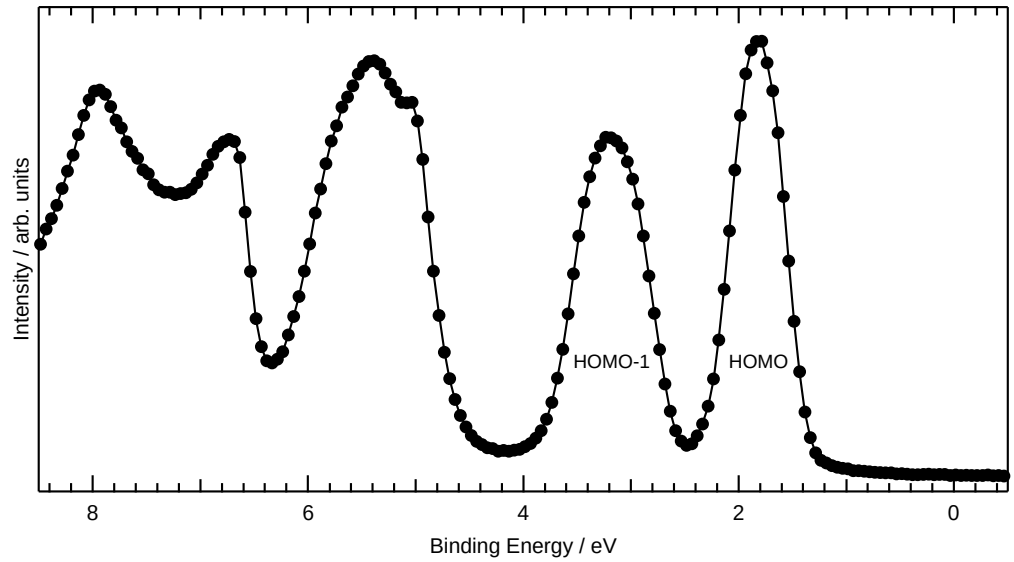

FIGURE 3.12: The PES spectrum of the valence region of bulk C_{60}, obtained using $h\nu = 21.2$ eV.

for an annealed monolayer, it is possible to grow a monolayer without annealing, by careful monitoring of the C 1s to Si 2p ratio during a series of sub-monolayer depositions. This may be exploited in order to calibrate the deposition rate of the C_{60} source.

Figure 3.13 shows valence band and Si 2p core-level spectra for the clean Si(111)–(7×7) surface, a thick film of C_{60} at this surface and monolayers produced by three different methods: growth in sub-monolayer steps without annealing, and annealing to 300°C by e-beam and direct heating. Compared to the valence band observed for a thick film of C_{60}, each monolayer valence band shows considerably more structure in the HOMO, and greater HOMO and HOMO-1 widths. The presence of the monolayer also produces in significant changes in the Si 2p core-level, compared to that observed for the clean surface. For monolayers produced by all of the methods considered, the rest-atom peak is absent, the dip in intensity in the middle of the core-level is more pronounced, and there is an increase in intensity on the higher binding-energy side of the spectrum. Comparing the curve fits to this spectrum to that for the clean surface, it can be seen that the fitted peak which lies roughly 1 eV above the bulk line is more intense in the

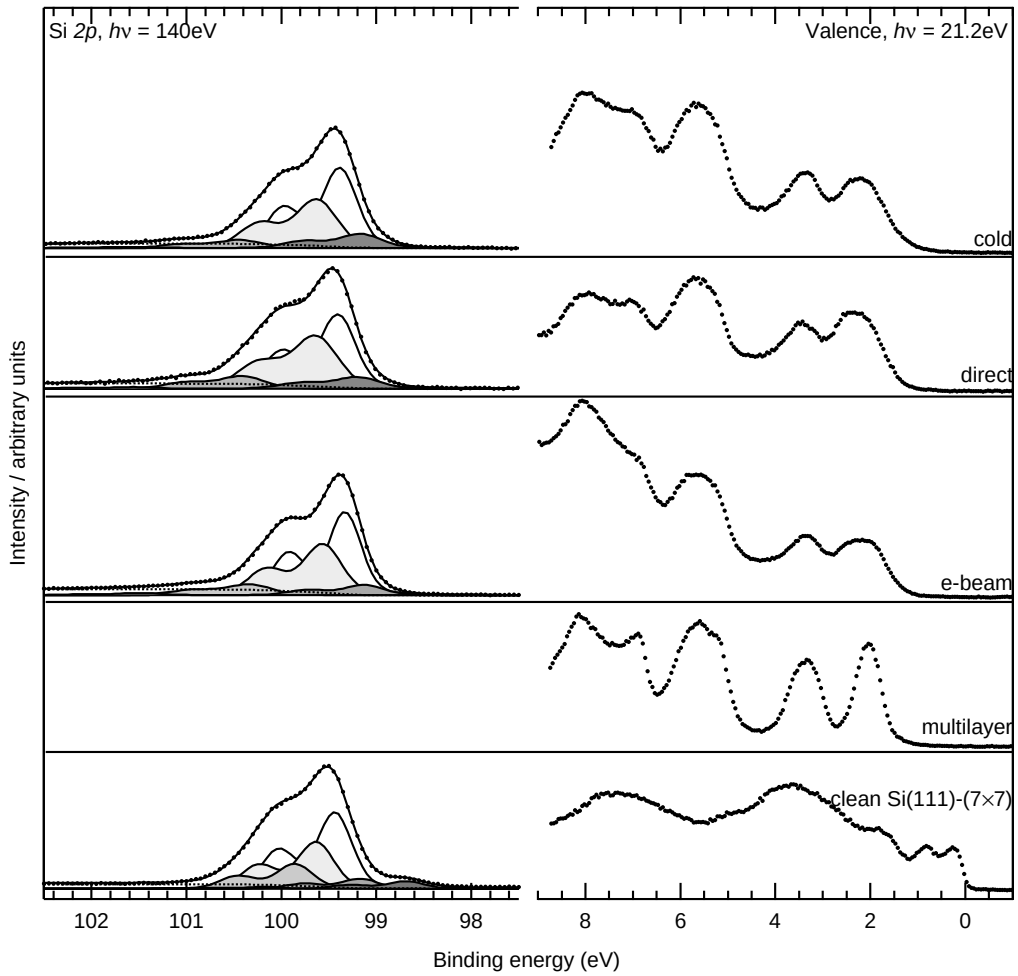

FIGURE 3.13: The valence band and Si 2p core-level spectra for the clean Si(111)–(7×7) surface, a thick C_{60} film and monolayers produced by annealing with e-beam & direct heating, and without annealing.

monolayer spectrum, and lies at a slightly lower binding energy. For the clean surface, this peak is associated with surface defects. Annealing the Si(111)–(7×7) surface to 300°C in the absence of fullerene does not increase the density of surface defects and, besides, the changes in intensity and position of this peak are observed for both annealed and cold monolayers. The changes in this peak are therefore attributed to the presence of a fullerene-related core-level component which is situated at a slightly lower energy than that due to surface defects — the separation between these two components is so small that they can not be resolved individually. A very small component also appears at around +2 eV. Its absence in the spectrum for the clean surface indicates that it is clearly fullerene-related. The presence of additional structure and broadness in the valence band, and appearance of new components in the core-level spectrum are indicative of a covalent interaction between the adsorbate and substrate [103].

There are some minor differences in the valence band and Si $2p$ core-level spectra between the two different methods of annealing. For the monolayer produced by resistive heating, components on the high binding-energy side of the Si $2p$ core-level, with RBEs of around +1 and +2 eV, are a little more intense and, in the valence band, there is some additional intensity at lower binding energies, around the HOMO. The two core-level components in question are related to a covalent interaction between the adsorbate and substrate. Stronger contribution from these components to the core-level for the directly-heated monolayer, and the corresponding changes in the valence band, are therefore attributed to the formation of additional Si–C bonds: the fullerene molecules are thought to 'bed-down' into the surface, with the result that a larger proportion of the cage participates in bonding to the surface. Why this effect should be more prevalent when using resistive- rather than electron-beam heating is uncertain. One possibility is that differences in resistivity between the bulk silicon and fullerene-covered surface result in higher temperatures at the surface, which are not detected using pyrometry. Alternatively, the higher heating rate achieved with direct heating may be the cause, particularly if the 'bedding-down' process is subject to significant kinetic limitations.

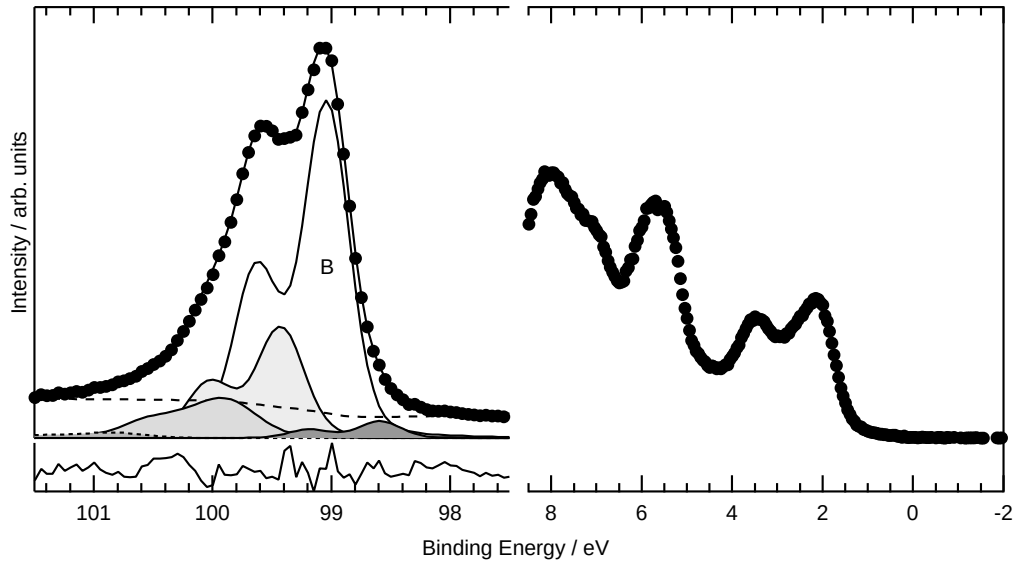

FIGURE 3.14: The valence band and Si $2p$ core-level spectra for just under a monolayer of C_{60} at the Si(100)–(2×1) surface, unannealed. The core-level spectrum has been decomposed into five components; the residual trace has been expanded by a factor of 10^3.

The Si $2p$ core-level and valence band spectra for just under a monolayer of C_{60} on Si(100)–(2×1) are given in figure 3.14. The presence of some intensity in the dimer-related component, with a negative RBE, indicates that the coverage of C_{60} has not quite saturated the surface. As for the Si(111)–(7×7) surface, upon adsorption of C_{60}, surface-related features in the valence band and core-level are attenuated, and fullerene-related components arise 1 eV above the bulk peak in the core-level. This is consistent with observations reported elsewhere [103], and again is indicative of the formation of covalent bonds between the fullerene and the Si surface. Again as per the Si(111)–(7×7) surface, monolayers prepared by annealing on the Si(100)–(2×1) surface demonstrate more intense fullerene-related core-level components, indicating stronger covalent bonding.

Upon adsorption of C_{60} at the Ag:Si(111)–$(\sqrt{3}\times\sqrt{3})$R30° surface, there is very little change in the core-level spectrum [104]. The lack of any apparent change in the core level indicates that the Ag:Si(111)–$(\sqrt{3} \times \sqrt{3})$R30° HCT reconstruction is preserved, and that there is not a strong interaction between the adsorbed C_{60}

and this surface. This is consistent with the fact that the C 1*s* core-level has only one component — there are no apparent chemical shifts [104]. It is therefore clear that C_{60} is only weakly physisorbed at this surface, and it may be expected that any annealing of the C_{60}/Ag:Si(111)–$(\sqrt{3} \times \sqrt{3})$R30° system would result in desorption of the C_{60}. However, during annealing the Ag also desorbs, and C_{60}–Si interactions play an important role. Depending on kinetic limitations, annealing leads to either desorption of the Ag, leaving a covalently-bound C_{60} monolayer on the (111) surface, or desorption of both the Ag and much of the C_{60}, resulting in a (111) surface on which step edges are decorated with C_{60} [105].

In summary, monolayer coverages of C_{60} on the Si(111)–(7×7) and Si(100)–(2×1) surface can be prepared either by annealing a multilayer to remove weakly physisorbed C_{60} overlayers, or by deposition of 1 ML of material from a calibrated source. There is strong evidence that cold monolayers are chemisorbed, and it is certain that annealing to around 300°C results in the formation of covalent bonds. At the Ag:Si(111)–$(\sqrt{3} \times \sqrt{3})$R30° surface, however, C_{60} is weakly physisorbed; annealing leads to desorption of the Ag resulting in covalently bound C_{60}, either in a monolayer or at step edges.

CHAPTER 4

Theoretical studies of adsorption

Ab initio computational chemistry is finding increased use in the field of surface science, particularly in the study of adsorption. However, computational expense limits the size of adsorbates and range of adsorbate-substrate interactions that it is feasible to investigate. This chapter considers the effectiveness of a new functional, EDF1, in reducing this computational expense without compromising accuracy.

Recent developments in the field of single-molecule devices [106–109] and the manipulation and self-assembly of larger molecules, most notably fullerenes and nanotubes [8, 9, 11, 14, 110, 111], at various surfaces have generated particular interest in theoretical studies of the adsorption of larger molecules. However, as the molecule under consideration becomes larger, the number of calculations required for a comprehensive investigation rapidly increases, due to the increased number of possible binding configurations. Furthermore, it is necessary to consider a

larger area of the substrate, which leads to a rapid increase in computational expense. For these reasons, it is desirable to ensure that the computational model used yields high accuracy for an acceptably low computational investment.

Adsorption may be modelled through the use of either plane-wave calculations, which employ a super-cell model of an area of the surface, or calculations based on Gaussian basis sets, which use a cluster model to represent the substrate. The accuracy of results as a function of computational expense in the latter case is considered here, as this method has been used with some success to investigate the adsorption of small organic molecules — ethene, ethyne, cyclohexane and benzene, to name a few — at the Si(100) surface [112–115].

4.1 General considerations

4.1.1 Cluster models of the Si(100) surface

Figure 4.1 shows a typical cluster model of the Si(100) surface. In this model, unfilled valencies at the periphery are capped with hydrogen, whilst those at the (100) surface are left unsaturated such that they may dimerise during geometry optimisation. In this way, isolated clusters may be treated as charge-neutral with singlet multiplicity in *ab initio* calculations. Importantly, the cluster incorporates several layers of silicon, permitting the study of both the adsorption of a species at the surface, and any resulting sub-surface relaxations.

Due to limitations of computational expense, few studies have employed cluster models of the Si(100) surface that contain more than a single dimer row. Multiple dimer-rows are required, however, if the model is to be used in the study of larger adsorbates or in the investigation of the longer-ranged effects of adsorption. It is in multi-row systems that a deficiency of the cluster model becomes particularly apparent: when optimised at any level of theory, the cluster undergoes relaxation resulting in curvature, as illustrated in figure 4.1.1, the radius of which is inversely proportional to the number of dimer rows. This most likely comes about due to an imbalance in tension at the upper and lower sur-

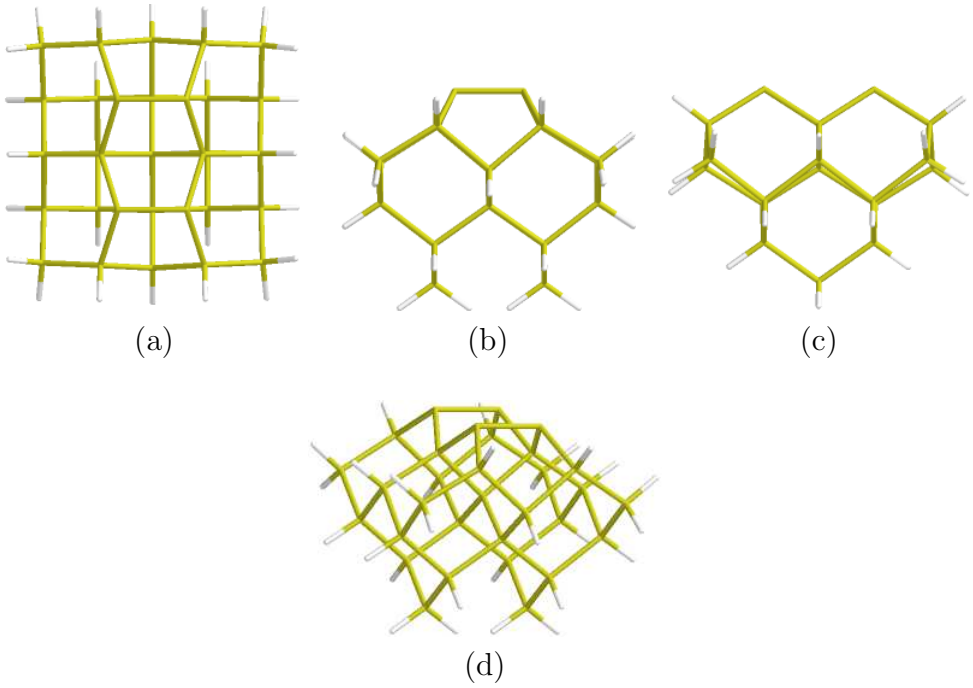

FIGURE 4.1: A cluster model of the Si(100) surface viewed from above (a), along the [110] direction (b) and [$\bar{1}$10] (c) directions, and in perspective (d).

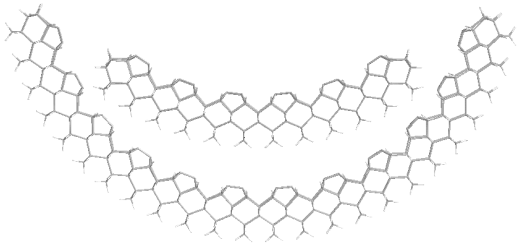

FIGURE 4.2: An illustration of the problem of cluster curvature.

faces, arising from the presence of dimers at only one of these. The curvature of the cluster involves the relaxation of a large number of bond lengths and angles, which may make the energy associated with this relaxation greater than that associated with the localised relaxation of surface dimers. Furthermore, the presence of an adsorbed species at the upper surface results in a change in the radius of curvature, and this implies that any binding energy determined from such a model will include some contribution arising from the difference in cluster curvature between the isolated and bound states.

As it stands, the multi-row cluster model is a poor representation of the Si(100) surface, in terms of both energetics and geometry. Although the curvature is less apparent in single-row models, it may certainly affect results. This issue must be addressed through the imposition of certain geometrical constraints to eliminate or, at least, minimise its effects in all clusters containing more than a single dimer. However, the validity of one set of constraints over another is a controversial issue, as a small change in the nature of these constraints can have significant effects on the model [87]. For this reason, a number of possible approaches were investigated.

Cluster constraints

The most self consistent approach to resolution of the cluster curvature issue is, unfortunately, the most computationally expensive. A multi-row cluster is extended to the maximum possible number of layers, such that the lowest consists of a single silicon atom, or row of atoms, the unfilled valencies of which are capped with hydrogen. This *extended* cluster is then used to represent the substrate in all calculations. Of course, the number of silicon centres that must be considered rises very rapidly with the number of dimers and dimer rows in the model. For any cluster larger than two rows containing two dimers each, the large computational expense renders this approach unfeasible.

Self consistency may be compromised to produce an approach which involves only one highly expensive step. The geometry of the extended cluster is optimised

at the same level of theory as that used, subsequently, to calculate adsorption geometries. Excess layers of silicon are then removed. The atoms of the lowest remaining layer are fixed in position, and their unfilled valences capped, giving a *cropped* cluster. The cropped cluster is used in all subsequent calculations, both in the presence and absence of adsorbates. Once again, however, this technique is not practical for clusters containing more than a few dimers or rows.

It is possible to conceive of a further compromise, in which the extended cluster is optimised at a lower level of theory. However, different levels of theory yield slightly different atomic co-ordinates in the lowest layer of the resulting cropped cluster. The results from one method are not readily justified as being more appropriate than those of another. Importantly, for a fixed calculation scheme, the relative positions of atoms in the lowest layer of a cropped cluster can vary slightly, as more dimers or dimer rows are added. Hence, the self consistency of this approach is lost, whilst overall computational expense remains high.

An alternative basis for the constraints on a cluster is that the lowest layer of silicon in the model should be representative of bulk-like silicon, resulting in an *empirical* cluster model. Positions of atoms in the lowest layer are determined from consideration of the experimentally obtained lattice constant of bulk silicon and its crystallographic structure. Unfilled valencies, with the exception of those on dimerising silicon centres, are capped with hydrogen, placed such that the H-Si bond length matches the empirical value observed in SiH_4, and tetrahedral bond angles are preserved. In all geometry optimisations, the lowest layer of silicon atoms are fixed in their original, empirical positions, in addition to those hydrogen centres that represent bonds to bulk-like silicon, namely the lowest two layers of hydrogen. Choosing the relative positions of silicon centres in this way is not theoretically self consistent, but it removes the need for the costly optimisation of an extended cluster and ensures that the structure of the bulk-like layer does not vary with the number of dimers in the model. This empirical cluster approach is far more desirable than others presented above, as it incurs no additional computational expense, and maintains a degree of self-consistency across cluster models of varying size.

The constraints of the empirical cluster model were employed in this research for all clusters containing more than a single dimer. The single dimer cluster itself is a special case, as only four layers of silicon are required to result in a single atom in the lowest layer, alleviating the necessity for geometric constraints. The four layer, single-dimer cluster therefore serves as an excellent system with which to compare different computational schemes, as its use ensures that calculations carried out elsewhere can be precisely reproduced.

4.1.2 Theoretical approach

Studies which have used cluster models of the Si(100) surface incorporating more than a single dimer row have typically involved some compromise in terms of the level of theory employed, in order to reduce computational expense. One popular compromise is the use of semi-empirical methods, such as AM1 and PM3 (§2.4.2 and §2.5.2). These semi-empirical methods are much less computationally demanding than *ab initio* techniques, but this is achieved through the neglect of many of the two-electron repulsion integrals and approximation of those that remain with some parametric form. Semi-empirical methods are parameterised by fitting the model to experimental data and, for historical reasons, this parametrisation is often biased towards agreement with experimental data for organic species. As a consequence, such methods frequently give poor results for inorganic systems, and may therefore not be appropriate for the study of adsorption at semiconductor surfaces.

An alternative approach to the reduction of computational expense involves the reduction of the number of electrons in a system that must be treated explicitly, and thereby of the number of costly two-electron integrals that need to be evaluated. This can be achieved through the use of ECP basis sets (§2.4.1). However, development of ECP basis sets has, in part, been driven by the need to reduce computational expense, and so the number of basis functions used in these sets to model the remaining explicitly treated electrons is typically quite modest. Coupled with the fact that popular density functions and HF theory

yield more accurate results when used in conjunction with a large basis set, as a result from their derivation in the limit of a complete basis set, their performance in conjunction with an ECP basis set can be poor, as results will show.

The empirical density functional, EDF1 [57], on the other hand, was developed with the use of smaller basis sets in mind. The starting point for the development of a density functional for computational chemistry is often the selection of a few exchange and correlation functionals, each of which is derived from consideration of a particular physical situation. Hybrid functionals, such as B3LYP [55,56], also include a contribution from the exact Fock exchange. The mixing coefficients for these various contributions are then adjusted such that the results from the functional agree exactly with those from experiment for a particular system, or with those from a more complex theoretical consideration of some system. EDF1 was constructed in this spirit, through the linear combination of a large number of density functionals and the Fock exchange functional. Its mixing coefficients were varied to fit results from the functional to the G2 [58] set of experimental data for small molecules, using the relatively small 6-31G basis set. In the fitting process, many mixing coefficients fell to zero, indicating that contributions from certain functionals are not beneficial within the limit of this basis set. Significantly, the exact Fock contribution is not required, eliminating the necessity for analytical evaluation of integrals. The nature of EDF1 therefore suggests that it may demonstrate superior performance in conjunction with smaller basis sets in comparison to other functionals, whilst at the same time offering a reduction in computational expense, in its own right.

Calculation scheme

A large number of computational schemes have been considered in the course of this research, but the results presented here concentrate on those achieved through combinations of the B3LYP or EDF1 functional with the all-electron 6-31G* or LANL2DZ [52, 53] pseudopotential basis set. The general approach to a cluster model study of adsorption is to carry out geometry optimisations of the

isolated cluster, isolated adsorbate and possible binding configurations.

The results of a geometry optimisation can depend heavily on the quality of the initial guess geometry. In order to maintain some degree of consistency across initial guess geometries, each was generated by the same method. This method begins with the isolated empirical cluster model, optimised at the required level of theory (e.g. B3LYP/6-31G*), with the lowest layer of silicon atoms fixed in their empirical positions, as required by the model. The adsorbate is then placed at the surface of the cluster, in a position and orientation approximating that expected in the bound state. Appropriate chemical bonds are defined, for the purposes of a partial optimisation using the low level MMFF94, in which only the positions of atoms constituting the adsorbate and the dimers to which it is bound are allowed to relax.

In many cases, this partial optimisation provides a reasonable first approximation to the adsorption geometry. However, MMFF94 is a very crude model and, as such, it demonstrates an energetic preference for silicon-silicon bond lengths which do not agree well with empirical values. As a consequence of constraining the majority of silicon centres in empirical positions, the molecular mechanics optimisation may detect strain in the system and try to minimise it by drastically altering the orientation of the adsorbate. In such cases, the results of the optimisation are rejected, and the adsorbate manually *constructed* at the surface. The geometry resulting from the MMFF94 optimisation, or the manual construction of an adsorbate, is then partially optimised using AM1, a semi-empirical method, using the same constraints as for the molecular mechanics stage. The model is then ready for the determination of the equilibrium geometry and bound state energy at a high level of theory, subject to the constraints required by the empirical cluster model.

The various stages of optimisation may appear to be unnecessary, but they all serve to reduce overall computational expense. MMFF94 calculations are inexpensive, and allow for large changes in the adsorbate position in order to lower energetic contributions due to strained bonds at the surface. Since molecular mechanics methods do not, in any way, consider electronic structure, electronic

behaviour which may affect the geometry is utterly neglected. *Ab initio* theories take such behaviour into account, but if large changes in the geometry result, this necessitates many optimisation cycles. It is therefore preferable to include the semi-empirical stage, which models electronic structure in a coarse but affordable manner.

4.1.3 Zero-point correction

It must be noted that the theoretical adsorption energies presented in this chapter have not been zero-point corrected: contributions to the adsorption energy due to differences in the ground state vibrational modes of the isolated and bound systems have not been accounted for. Crude investigations carried out using AM1 indicate that a correction of approximately -0.01 eV may be expected for each Si–C bond formed upon adsorption, perhaps corresponding to the damping of C–C stretch modes.

4.2 Cluster geometry

Experimentally, the Si–Si dimer bond is found to have a length of 2.24 ± 0.08 Å. All geometry optimisations using combinations of the LSDA [31], B3LYP and EDF1 density functionals with the 3-21G, 6-31G, 6-31G* and LANL2DZ basis sets found the dimer length in the single-dimer clusters to be 2.23 Å, with a standard deviation of 0.02 Å between calculation schemes, and bond angles on the lowest Si centres remaining close to a tetrahedral geometry. For the two-dimer cluster with empirical constraints, the average bond length remains at 2.23 Å, but the standard deviation increases to 0.05 Å. HF theory, when used with the same basis sets, generally permits a greater relaxation of bonds about the lowest Si centres and predicts shorter Si–Si bond lengths. Across basis sets, HF theory gives an average dimer length of 2.19 Å, with a standard deviation of 0.02 Å.

All cluster models considered — one- and two-dimer unconstrained, extended, cropped and empirical — predict a symmetric dimer configuration in the ground state at all levels of theory used here, despite much effort expended in attempts

to reproduce dimer buckling through subtle variations in geometric constraints. As discussed previously, the nature of the ground state of the Si(100) surface is not fully understood (§3.5.2). The controversy surrounding this issue merits a discussion of the effects of dimer buckling at non-zero temperatures (i.e. neglecting the energetic contributions from vibrational modes) on the binding energies and geometries obtained here.

Although the physical origins of dimer buckling are a subject of great debate, it is generally believed that the energetic difference between the buckled and symmetric dimer states is small ($\sim$ 0.1 eV) compared to adsorbate binding energies ($\sim$ 2 eV). This error is certainly of the same order as, or smaller than, that inherent in the use of HF theory or a density functional approach in the limit of an incomplete basis set. Should greater theoretical accuracy be required, it is plausible that the energetic effects of dimer buckling may be included as a perturbation. Secondly, room temperature STM images indicate that, upon the adsorption of a wide variety of molecular species, the dimers involved in adsorption drop out of the buckled state. From these considerations, it is possible to be fairly confident that, despite the widespread uncertainty concerning the Si(100) ground state geometry, the absence of dimer bucking observed here is not significant when considering either binding geometries or binding energies. It may, however, be important when considering adsorption pathways and the electronic structure of transition states.

4.3 Testing the model

4.3.1 Single-dimer cluster

Figure 4.3 shows the bound state of ethene and ethyne with the single-dimer cluster model. The binding energies obtained from various calculation schemes are presented in table 4.1. As stated, the single-dimer cluster is not subject to any geometric constraints, and therefore serves as an excellent test system; it is worthy of note that the binding energies obtained using B3LYP/6-31G* are

identical to those found elsewhere [114].

Experimentally, temperature programmed desorption (TPD) techniques have indicated binding energies of 1.65 eV and 2.00 eV for ethene and ethyne, respectively, at the Si(100) surface [116, 117]. For both ethene and ethyne, and for a given basis set, EDF1 agrees more closely with the experimental results than does HF theory, the LSDA or B3LYP. In the case of ethene, EDF1 is in close agreement with experiment when used with any but the smallest of these basis sets. The same may not be said when considering ethyne, as *all* calculation schemes predict binding energies which are significantly larger than that obtained experimentally.

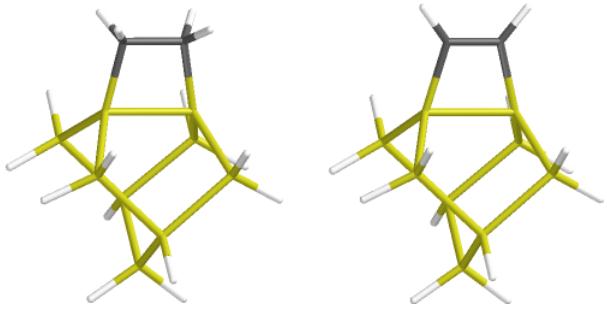

(a) (b)

FIGURE 4.3: Binding geometries for ethene (a) and ethyne (b) to a single-dimer cluster

Ethene; experimental binding energy = 1.65 eV [116].

	HF	LSDA	B3LYP	EDF1
3-21G	2.41	3.02	2.25	2.05
6-31G	1.98	2.58	1.82	1.61
6-31G*	2.22	2.72	1.99	1.75
LANL2DZ	2.11	2.66	1.97	1.74

Ethyne; experimental binding energy = 2.00 eV [117].

	HF	LSDA	B3LYP	EDF1
3-21G	2.89	3.56	2.83	2.69
6-31G	2.63	3.24	2.53	2.38
6-31G*	3.04	3.54	2.86	2.68
LANL2DZ	2.75	3.32	2.67	2.49

TABLE 4.1: Binding energies (in eV) of ethene and ethyne to a single-dimer cluster model, obtained using various functional/basis set combinations.

However, it is important to realise that the accuracy of TPD techniques when used in the determination of binding energies varies with adsorbate, as discussed in [114]. Applied to ethene at Si(100), TPD measurements may be expected to serve as an accurate probe of binding energy, since the majority of adsorbed molecules desorb intact. Ethyne at Si(100), on the other hand, demonstrates a preference for thermal decomposition: only a small proportion of adsorbed molecules are desorbed, and hence TPD may indicate a desorption energy which is significantly lower than that required to break Si–C bonds.

The general conclusion that can be drawn from these results is that both the LSDA functional and HF theory clearly yield less accurate results compared to those obtained using either B3LYP or EDF1. Additionally, the 3-21G basis set performs poorly in all cases, and EDF1 demonstrates performance comparable to that of B3LYP. Having compared these calculation schemes using the simplest possible model of adsorption, it is necessary to test the effectiveness of the cluster model with empirical constraints, and the performance of EDF1 and the LANL2DZ pseudopotential basis set applied to this larger system.

4.3.2 2-dimer cluster with empirical constraints

Computational expense becomes an issue when considering the 2-dimer cluster, as the size of this system is not insignificant, and so it is beneficial to reduce the number of necessary calculations. Given their inferior performance in the single dimer tests, it was considered unnecessary to perform further calculations involving HF theory, the LSDA functional or the 3-21G basis set. For the purposes of testing, the 6-31G* basis set was favoured over 6-31G, since the usage of the former is a standard in computational chemistry and it is therefore more prevalent in the literature. Additionally, the issues concerning the accuracy of experimental binding energies for ethyne at Si(100) suggest that comparison of these values to further theoretical results would produce very little that is conclusive.

Adsorption of ethene modelled with the two-dimer cluster is illustrated in figure 4.4, with theoretical binding energies given in table 4.2. With each calculation

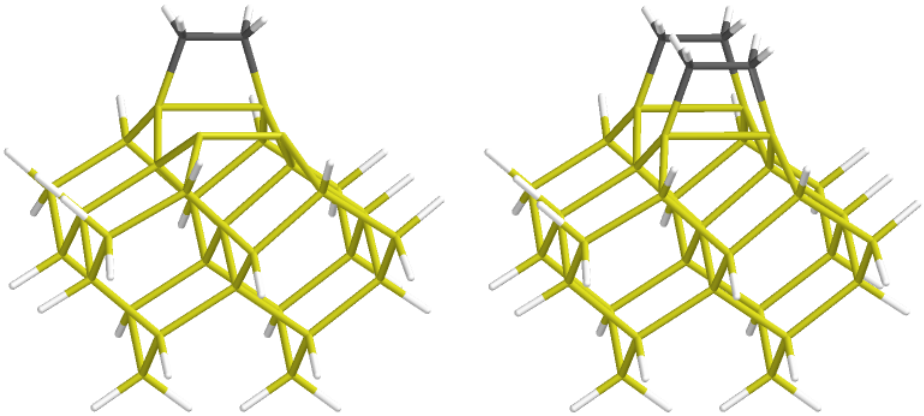

(a) (b)

FIGURE 4.4: Single (a) and double (b) adsorption of ethene on the 2-dimer cluster

	Binding energy / eV			
	EDF1		B3LYP	
	6-31G*	LANL2DZ	6-31G*	LANL2DZ
single	1.86	1.85	2.13	2.37
double	1.78	1.75	2.07	2.30

TABLE 4.2: Binding energy of ethene to a 2-dimer empirical cluster, single (0.5 monolayer) and double (one monolayer), obtained using B3LYP and EDF1 with both all-electron and pseudopotential basis sets.

scheme, it can be seen that there is a reduction in binding energy as the cluster coverage is increased from 0.5 ML to 1 ML (corresponding to single and double adsorption, respectively). This may be expected, as the energetic preference for adsorption is certain to decrease with the number of available binding sites, in the absence of any attractive adsorbate–adsorbate interactions.

Once again, in all cases, EDF1 predicts adsorption energies which are closer to the experimentally determined value of 1.65 eV. Importantly, there is only a very small change in the values obtained from EDF1 when pseudopotentials are introduced. The same may not be said for B3LYP: as the number of basis functions is decreased, the accuracy of this functional is reduced; this most likely results from the optimisation of this functional for use with larger basis sets.

Interestingly, the ethene binding energies obtained using EDF1/LANL2DZ

and the cluster model with empirical constraints compare more favourably with experiment than those obtained from periodic slab calculations [118]. The slab calculations predict a buckled dimer in the ground state, and yield binding energies of 1.89 eV and 1.93 eV for 0.5 ML and 1 ML coverages of ethene.

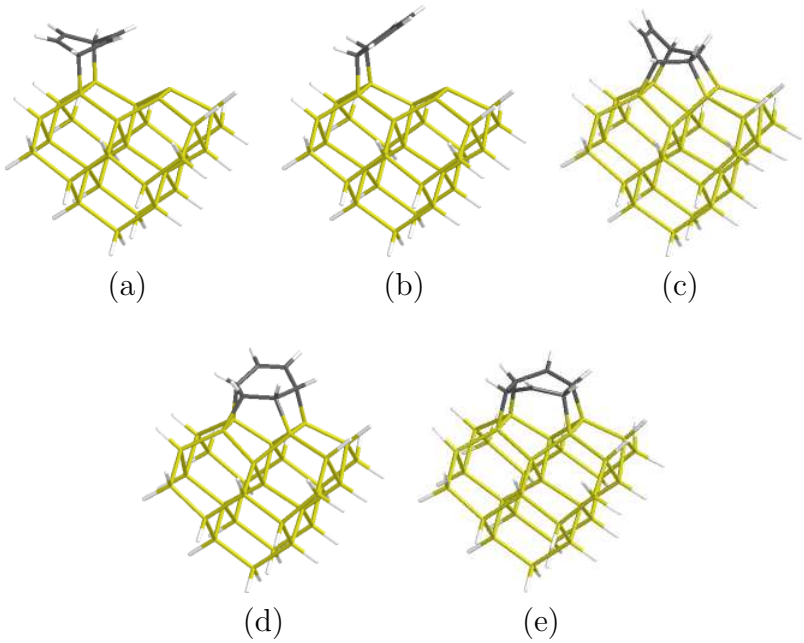

FIGURE 4.5: Binding geometries of benzene to the 2-dimer cluster model of the Si(100) surface: 1–4 or Deils-Alder configuration (a); edge bound (b); tight bridge (c); twisted bridge (d); symmetric bridge (e).

	EDF1/LANL2DZ	B3LYP/6-31G* [112]
Edge	0.52	n/a
1-4	1.04	1.04
Tight Bridge	1.44	1.12

TABLE 4.3: Binding energies for stable states of benzene on Si(100), obtained using EDF1/LANL2DZ.

4.3.3 Larger adsorbates

Benzene

Further testing of the model concerns its performance when considering larger adsorbates. Benzene serves as a good test system, since its adsorption at Si(100) has been studied extensively, using both theoretical and experimental techniques. Figure 4.5 shows five possible adsorption geometries for benzene on the two-dimer cluster. Using the nomenclature introduced in reference [119], these are termed: (a) the 1–4 or Diels-Alder configuration; (b) edge bound; (c) the tight bridge; (d) the twisted bridge; (e) the symmetric bridge. The first four of these configurations were treated as singlet states. The symmetric bridge, however, has lone pairs on the two carbon centres that are not involved in Si–C bond formation, and therefore has triplet multiplicity. EDF1/LANL2DZ indicates that of these five configurations, only three are stable. The binding energies for these stable configurations are given in table 4.3, and compared to results obtained elsewhere using B3LYP/6-31G*.

Experimental studies of benzene at Si(100) indicates two stable states at 1.21 eV and 1.39 eV [120]. From the EDF1/LANL2DZ adsorption energies, it is possible to assign the Diels-Alder and tight bridging configurations to these two states. EDF1/LANL2DZ predicts a small binding energy for the edge-bound configuration. It is conceivable that this may be a metastable state that occurs during desorption of the tight-bridging species.

Naphthalene

Of the fifteen possible binding configurations for naphthalene to a two-dimer cluster, EDF1/LANL2DZ, in conjunction with the empirical cluster constraints, predicts that six are stable. These are given in figure 4.6, along with their theoretical binding energies. Various spin states were considered, but all stable configurations were found to have singlet multiplicity. Analysis of the C–C bond lengths reveals that rehybridisation takes place, resulting in no unfilled valencies on any carbon centres.

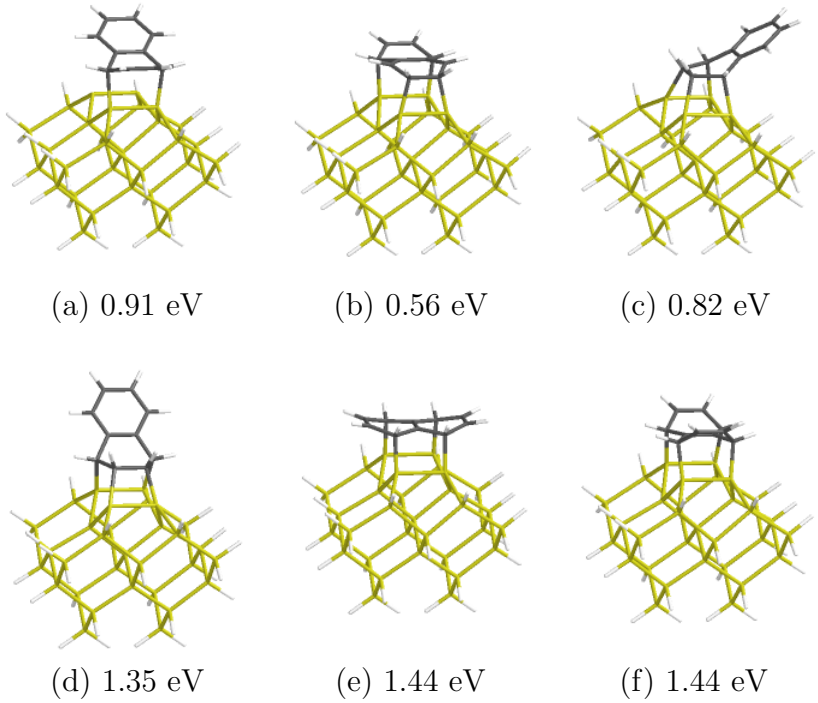

(a) 0.91 eV (b) 0.56 eV (c) 0.82 eV

(d) 1.35 eV (e) 1.44 eV (f) 1.44 eV

FIGURE 4.6: Binding geometries of naphthalene on the Si(100) surface

There are no experimental data available with which to compare these theoretical binding energies. However, the binding energy per Si–C bond is comparable to that obtained for the adsorption of ethene, acetylene and benzene, indicating that these results are reasonable.

4.3.4 Vibrational structure

The symmetric and antisymmetric H–Si stretch frequencies at the hydrogen-terminated Si(100) surface have been determined experimentally with a high degree of confidence. Table 4.4 shows the harmonic frequencies for these vibrational modes, obtained using both B3LYP and EDF1. In conjunction with the LANL2DZ pseudopotential basis set. The harmonic frequencies obtained using EDF1 match the experimental values more closely than those from B3LYP. The superior agreement with experiment of EDF1, applied to this silicon–hydrogen system, becomes even more apparent if the difference between symmetric and

Mode	Frequency / cm^{-1}		
	EDF1/LANL2DZ	B3LYP/LANL2DZ	Experimental [121]
Symmetric	2174	2202	2097
Antisymmetric	2166	2201	2088
Difference	8	1	9

TABLE 4.4: Vibrational frequencies of the Si-H symmetric and antisymmetric stretch modes at the H-passivated Si(100) surface.

antisymmetric stretch frequencies is considered.

4.4 Computational Expense

The principal purpose of this investigation was the determination of a method by which the computational expense of a study of adsorption could be reduced, without significantly compromising the accuracy of results. Pseudopotentials have been employed previously to achieve such a reduction, but when used with the popular B3LYP functional, the accuracy of results is compromised.

Table 4.5 shows the relative processing times required for evaluation of the SCF and its gradients, using combinations of B3LYP and EDF1 with 6-31G* and LANL2DZ, for a number of systems. In terms of these computational times, in the worst case the performance of EDF1 is comparable to that of B3LYP for SCF evaluation. At best, there is a reduction in expense when employing EDF1 as compared to B3LYP, whilst the results from the study of energetics indicate no significant loss in accuracy. EDF1 clearly demonstrates a lower computational cost for the evaluation of SCF gradients, due to the absence of the exact Fock exchange. It is also clear, in terms of both energetics and the SCF gradient evaluation times, that EDF1 is more tolerant of the use of pseudopotentials, which can be seen to yield a much greater cost benefit when larger systems are considered.

The significant reduction in computational expense offered by the use of EDF1 coupled with a pseudopotential basis set, without sacrificing the accuracy of binding energies and vibrational structure, makes this scheme an attractive approach

	B3LYP/ 6-31G*	EDF1/ 6-31G*	B3LYP/ LANL2DZ	EDF1/ LANL2DZ
Self-consistent field				
1-dimer cluster	3.48	3.70	1.00	1.29
1-dimer cluster + C_2H_2	3.07	2.84	1.01	1.00
1-dimer cluster + C_2H_4	2.86	2.18	1.00	1.02
1-dimer cluster + 2H	7.88	5.49	1.20	1.00
2-dimer cluster	11.45	2.79	1.20	1.00
Field gradients				
1-dimer cluster	5.23	2.79	1.13	1.00
1-dimer cluster + C_2H_2	5.09	2.51	1.15	1.00
1-dimer cluster + C_2H_4	5.05	2.46	1.15	1.00
1-dimer cluster + 2H	11.75	3.86	1.52	1.00
2-dimer cluster	23.51	2.13	1.62	1.00

TABLE 4.5: Relative computation times for SCF and field gradient evaluations, using various calculation schemes.

to the investigation of larger adsorbates in organic–silicon systems. For the study of fullerene adsorption, if long-range effects may be neglected, it may only be necessary to consider a two dimer by two row cluster model. However the reduction in computational expense offered by this calculation scheme, compared to that incurred by the use of B3LYP/6-31G*, is only of the order of a factor of ten. Although modelling such a cluster with EDF1/LANL2DZ is feasible, it would still require significant computational power, the level of which is currently only achievable through the use of parallelised code, a functioning implementation of which was unavailable at the time of this work. An alternative approach may be realised through the use of quantum mechanical / molecular mechanical (QM/MM) methods, which have been applied to the study of the Si(100)–(2×1) surface with some success [122, 123]. In a QM/MM calculation, the substrate model may incorporate a very large number of atoms, the majority of which are treated using inexpensive molecular-mechanical techniques; only those that are involved in bonding to an adsorbate, and some n nearest-neighbour atoms, are given a full quantum-mechanical treatment. Given the performance demonstrated here, EDF1 may be a highly suitable candidate for the quantum-mechanical por-

tion of such QM/MM calculations.

More positively, this work has been the first test of EDF1 applied to larger systems. Here, this functional has been shown to perform well in the treatment of larger systems whilst, elsewhere, it has been shown to yield excellent results for a wide variety of small systems [57]. It is therefore possible that EDF1 could be applied to great effect in other fields of study.

4.5 Binding of C_{60} to Si(100)

Preliminary calculations, concerning the binding of C_{60} to the Si(100) surface, have been carried out. STM studies indicate that, when deposited onto the Si(100)–(2×1) surface at room temperature, C_{60} adsorbs at one of two specific sites between dimer rows. Individual molecules adsorb such that their centres lie between four dimers. Intermolecular effects and annealing can lead to molecular centres positioned between two dimers. Higher temperature annealing can result in molecules adsorbing on top of dimer rows [101].

Calculations were carried out using the semi-empirical method AM1, employing a four-dimer cluster model, with two dimers in two rows, for inter-dimer binding configurations, and a two dimer cluster model for dimer-row configurations. All cluster models were subject to empirical geometric constraints. Two-dimer systems were considered using unrestricted (UHF) spin-orbitals. Calculations involving the four-dimer cluster used restricted (RHF) spin-orbitals: the use of UHF orbitals caused the calculation size to exceed that of the physical memory available, and the performance impact associated with the use of virtual memory rendered UHF calculations unfeasible. The binding energies for a number of configurations are given in table 4.6, and compared to those from a recent study employing DFT and periodic boundary conditions [124] [1]. The table contains schematic representations of bonding configurations, in which the carbon centres involved in Si–C bonds are highlighted. The dimers are not shown in the schemat-

[1] Reference [124] contains a printing error. In Figure 4, the labels (a), (b) and (c) should read (e), (f) and (g), in order to correspond to entries in Table 1. This adjustment is known to be correct from examination of a pre-print of the article in question.

ics, for reasons of simplicity. In all schematics, the dimer orientation should be taken as horizontal: the position of the dimers with respect to the adsorbate is then implicit from the number of Si–C bonds, and whether adsorption is on top of a dimer row or between rows, as in the examples in figure 4.7.

For geometries on the dimer row involving a single dimer, the agreement between the results from AM1 and the DFT investigation is very reasonable. Both studies predict the same order of stability, and the binding energy for each configuration is comparable across the two methods. Applied to dimer-row geometries involving two dimers, AM1 predicts higher relative stability for two geometries (e and g), with respect to the other configurations, and that one configuration (o), found to be stable in the DFT study, is unstable.

Considering adsorption between two dimer rows, both the AM1 and DFT investigations show that there are seven stable bound states. Four of these are common to both computational methods, and the remaining configurations are specific to each method. However, the difference between the two sets of stable states predicted by each method may be the result of an inexhaustive consideration of binding configurations. Certainly, the three additional stable states found in the DFT investigation were not amongst the sixteen that were considered using AM1. Whether or not the reverse is true can not be ascertained from the journal article detailing the DFT investigation. Comparing the binding energies of the stable states common to both methods, there is reasonable agreement for all four bound states. It must be noted that the AM1 binding energies shown here were obtained using restricted spin-orbitals. Further optimisation using unrestricted

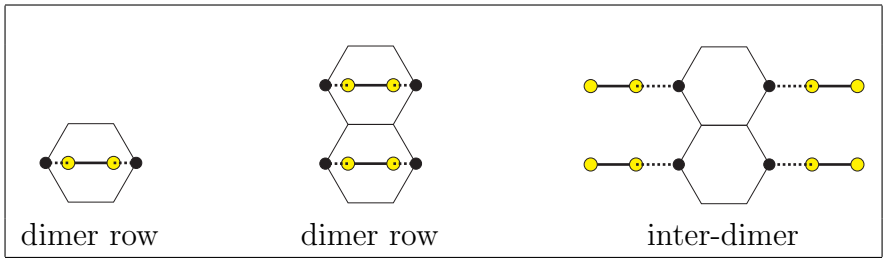

FIGURE 4.7: Schematic representations of C_{60} binding configurations, with dimer positions shown.

Binding geometries on the dimer row								
	E_B / eV			E_B / eV			E_B / eV	
Geometry	AM1	DFT	Geometry	AM1	DFT	Geometry	AM1	DFT
a 	3.65	3.57	*b* 	2.92	3.28	*c* 	2.47	2.90
d 	4.81	4.83	*e* 	4.53	4.15	*f* 	4.35	4.33
g 	4.12	3.94	*h* 	3.99	4.10	*i* 	3.62	—
j 	2.55	2.69	*k* 	2.49	—	*l* 	1.82	—
m 	1.76	—	*n* 	1.18	—	*o* 	—	3.13
Unstable	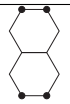						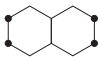	

Binding geometries between dimer rows								
	E_B / eV			E_B / eV			E_B / eV	
Geometry	AM1	DFT	Geometry	AM1	DFT	Geometry	AM1	DFT
p 	5.83	5.71	*q* 	5.23	—	*r* 	5.20	4.96
s 	4.41	4.85	*t* 	4.31	5.31	*u* 	4.21	—
v 	1.32	—						
Unstable	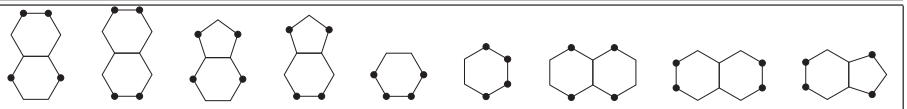							

TABLE 4.6: Binding energies, E_B, of C_{60} to the Si(100) surface, for various binding configurations. The values from AM1 are compared to those obtained in a DFT study, carried out elsewhere [124].

spin-orbitals would allow α and β orbitals to become spatially separate in order to lower the energy of the isolated cluster and bound states, and this could lead to significant changes in binding energy. Considering the RHF nature of the calculations, the agreement seen here is quite fortuitous.

During geometry optimisation of configuration *o*, the fullerene begins to rotate away from its original position, about an axis which is normal to the surface. It is possible that the instability of this configuration arises due to a mismatch between the empirical equilibrium Si–Si bond length, implied by the use of empirical geometric constraints, and that favoured by AM1. However, the rotation of the fullerene persists in the absence of any geometric constraints. The instability is therefore not due to the use of the empirical cluster model. It is not possible to conclude whether this binding geometry is physically unstable, arises due to the deficiencies of cluster models, in general, or due to approximations used in the AM1 semi-empirical method. Furthermore, it is not reasonable to rule out the possibility that the configuration is physically unstable, but was predicted as stable by the DFT investigation due to some deficiency of the numerical basis-set employed. The DFT investigation employed a simplified, numerical basis-set, in an effort to reduce computational expense. This basis set may be somewhat inflexible, as some results of the DFT investigation are questionable; in particular, one binding configuration that was found to be stable involves the formation of five bonds to one silicon atom. This is without precedent and, physically, highly unlikely.

Given the concerns outlined in section 2.4.2 and immediately above, regarding the limitations of semi-empirical methods and the numerical basis set employed elsewhere, the results of both the DFT and AM1 investigations are dubious in their reliability, despite their apparent agreement. It is difficult to have confidence in the absolute binding energies obtained using either method. Taken together, however, the studies may act as a useful guide to the relative stability of the various binding configurations. As such, it is possible to address the hypothesis that the adsorption of C_{60} at Si(100) may be modelled using molecules which represent fragments of the C_{60} cage, in order to reduce computational expense.

The order of stability of naphthalene-like states of C_{60} on the dimer row and the results for naphthalene, presented previously, do not agree in any way. Further investigations with AM1 have revealed that, upon adsorption, the relaxation of the fullerene cage differs greatly from that of various representative fragments, for instance corranulene ($C_{20}H_{10}$), differs greatly. Unfortunately, this renders an approach to the study of fullerene adsorption employing cage fragments unviable.

4.6 Valence bands from theory

Valence bands can be simulated by convolving the orbital energies obtained from a calculation, representing the initial states, with a Gaussian, modelling broadening processes. The results of such a treatment, employing energies from B3LYP/6-31G* and a Gaussian of width 0.4 eV, are shown in figure 4.8 for three different systems: isolated C_{60}, $(C_6H_5)_5C_{60}H$ and a C_{60} molecule bound to two silane groups (see figure 4.9). Experimentally determined valence-band spectra, obtained using PES with $h\nu = 60$ eV, for thick films of C_{60} and $(C_6H_5)_5C_{60}H$, and

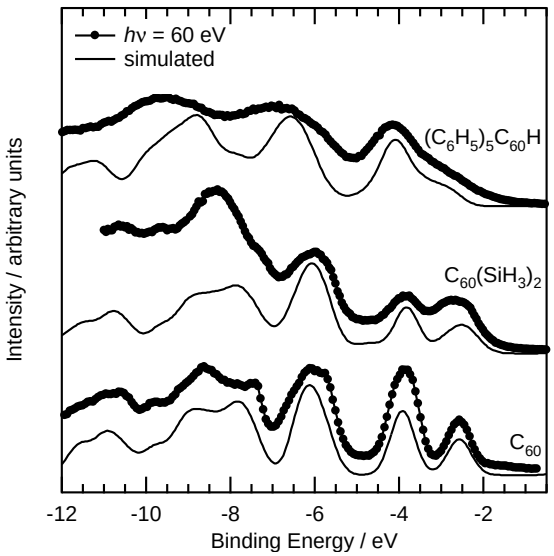

FIGURE 4.8: Experimental and theoretical valence-band spectra for three systems. Experimental results were obtained using PES with $h\nu = 60$ eV. Theoretical results were produced by convolving orbital energies from B3LYP/6-31G* with a Gaussian of width 0.4 eV.

a monolayer of C_{60} at the Si(100)–(2×1) surface are also shown, for the purposes of comparison.

The agreement between the experimental and theoretical results is quite remarkable, particularly as the calculations consider the ground state of the system, whilst photoemission is an excited-state measurement. Furthermore, final-state photoelectron diffraction effects, which can modulate the relative intensity of components in the valence band [64], are not considered in the calculation — the intensity of each peak in the theoretical valence bands arises simply from the degeneracy of each state. The agreement between the experimental and theoretical intensities must therefore be attributed to a fortuitous choice of photon energy for the experimental measurements. The divergence of the theoretical and experimental results at higher binding energy, in terms of absolute intensity, occurs due to the fact that the theoretical results do not include any contribution from the secondary-electron background.

Of particular note is the agreement between the experimental measurement for C_{60}/Si(100)–(2×1) and the results from a rather simplistic model of this system. The model involves silane groups bound to C_{60} at opposite vertexes of a hexagonal face, giving C–Si bonding as in many of the binding geometries found to be stable in the previous section. It is clear that much of the structure

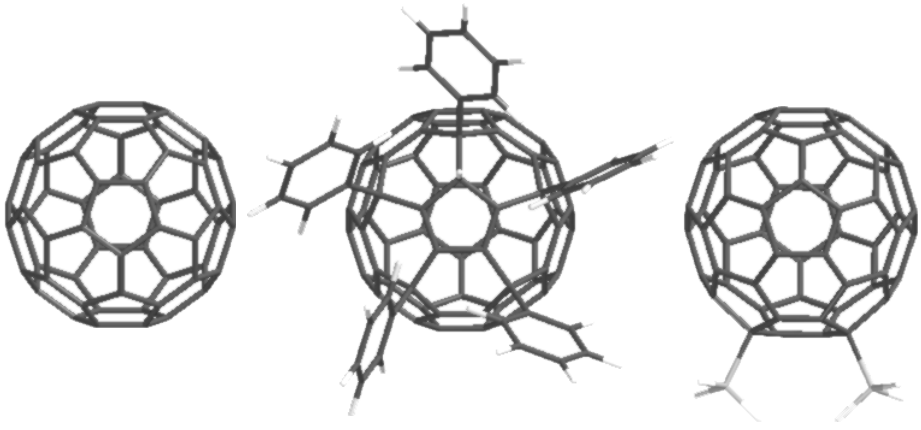

FIGURE 4.9: The geometries used in calculations to generate the simulated valence bands shown in figure 4.8.

in the experimental valence band arises solely due to the covalent interaction between Si and C_{60}; this is strong evidence for chemisorption of C_{60} at the Si(100)–(2×1) surface. Furthermore, since the simple model does not take into account the geometry of the (100) surface, it is possible to conclude that there is little strain in the C_{60}/Si(100)–(2×1) surface, as this would be sure to strongly affect chemical bonding, and therefore valence-band structure, such that the theoretical and experimental data would not demonstrate such excellent agreement.

CHAPTER 5

K-doped C_{60} films

This chapter concerns the role of strong covalent bonding in the alkali-metal doping of thin films of C_{60}. Results are presented from an experimental study of K-doping of C_{60} at the Si(111)–(7×7) and Si(100)–(2×1) surfaces, and a method for the determination of charge-transfer to the fullerene cage is discussed. There is evidence to suggest that the covalent interaction between C_{60} and these silicon surfaces causes rehybridisation within the fullerene cage, resulting in the splitting of the LUMO. A metallic state is seen at the Si(111)–(7×7) surface, but not at the Si(100)–(2×1) surface.

5.1 Introduction

There has been considerable work on the manipulation of C_{60} on semiconductor surfaces (see references in chapter 1) and the preparation of nanoscale contacts [125], motivated by the ideal of a nanoscale C_{60} 'wire'. In addition, the doping of C_{60} with alkali metals has been seen to dramatically alter its electronic structure

and transport characteristics [17, 126]. It is feasible that the transport properties of a nanoscale wire formed on a silicon surface [127] could be modified through similar doping methods; however, the role of the substrate must be understood. There has been much work to investigate the properties of alkali-doped C_{60} in the bulk (for a review, see [128]) and, to a lesser extent, in thin films supported on *metal* surfaces. However, there is little work concerning the influence of a reactive substrate. There have been two studies of K-doped C_{60} at Si surfaces [129, 130], but these have considered the Si–C_{60} interaction to be weak, which is a matter of controversy (§3.6.1). The strong covalent interaction between C_{60} and Si that is evident as a result of annealing provides an excellent opportunity to study the effects that may result from, for example, strong rehybridisation within the fullerene cage, or some interaction between the dopant and the substrate.

5.2 Experimental

The experimental measurements presented in this chapter were carried out at beamline 4.1 of the UK SRS (§3.4.1). The methods used for preparation of the clean Si(111)–(7 × 7) and Si(100)–(2 × 1) reconstructions are described in sections 3.5.1 and 3.5.2. C_{60} was deposited from a Ta-envelope dispenser, resistively heated to 450°C. Monolayers were prepared by annealing multilayer films to 300°C by direct heating, monitoring the sample temperature via pyrometry. Multilayer coverages were ensured prior to this annealing by deposition of C_{60} until the Si 2*p* core-level was no longer observable using a photon energy of 140 eV.

The potassium source used was a commercial alkali-metal dispenser, obtained from SAES Getters. A source current of 6.0 A was used for K-deposition, with the pressure maintained below 2.0×10^{-9} Torr. In order to ensure that no potassium-containing compounds, which may have collected on the outside of the source, were deposited onto the sample, the source was heated above deposition temperature (up to a current of 6.2 A) for 30 s, with no direct line of sight to the sample, prior to each deposition. Periodically, and before each sample was removed from the UHV chamber, an XPS survey spectrum was obtained using Mg Kα radia-

tion. The O 1*s* core-level region was examined closely in order to ensure that the sample had not become contaminated, due to the presence of the extremely reactive potassium.

5.3 K-doping of a thick C_{60} film

Figure 5.1 shows the evolution of the valence band as a thick film of C_{60} is doped with K. The valence band spectra were measured using a photon energy of 21.2 eV. The behaviour of the system is consistent with that observed elsewhere (see, for example, [126]). Upon exposure to potassium, all components in the valence band spectrum undergo a shift of 0.65 eV to higher binding energy. A feature between 0 eV and 1.3 eV binding energy develops as the exposure to potassium is increased. This feature corresponds to a band derived from the C_{60} LUMO, which becomes occupied by electrons donated from the potassium. As soon as this LUMO-derived band begins to fill, some DOS can be seen crossing the Fermi edge, indicating that the film has a metallic character. This is attributed to the presence of the conducting K_3C_{60} phase of K_xC_{60}. As more potassium is deposited, the LUMO-derived feature increases in intensity, and shifts to higher binding energy, reducing the DOS crossing the Fermi edge until, after 11 minutes of exposure to K, no metallic character remains. This corresponds to the insulating K_6C_{60} phase. It is therefore possible to estimate that the spectrum obtained after either $5\frac{1}{2}$ or 6 minutes of K exposure corresponds closely to the K_3C_{60} phase. The intensity of the DOS at the Fermi edge demonstrates a maximum in the 6-minute spectrum; this would be expected for the metallic K_3C_{60} phase.

At exposure times between 60 s and 6 minutes, there is a shoulder component on the low binding-energy side of the LUMO. This may be due to a Jahn-Teller distortion in the photoionised system [126], or the interplay between Jahn-Teller effects and LS-coupling in regions close to the metal-insulator transition [131], as a result of phase separation of different K_xC_{60} stoichiometries [132, 133].

In the spectra for exposure times in the region of 6 to 11 minutes, the HOMO

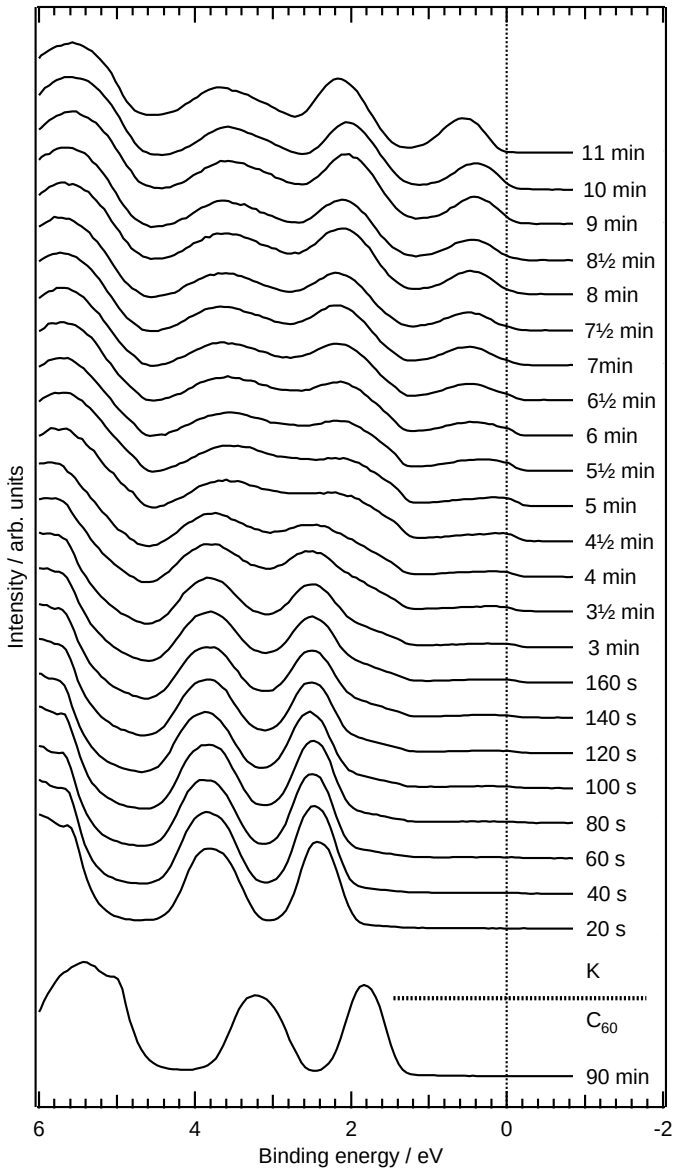

FIGURE 5.1: Evolution of the valence band as a thick C_{60} film is doped with K, obtained using $h\nu = 21.2$ eV.

and HOMO-1 are slightly broader than at either of these limits. This arises due to the fact that for $3 < x < 6$, the K_xC_{60} film consists of a mixture of the K_3C_{60} and K_6C_{60} phases: it has been shown that the valence band spectrum of K_xC_{60} with $3 < x < 6$ can be reproduced by combining the valence bands of the $x = 3$ and $x = 6$ phases, in varying proportion [126]. The onset of the shift of the LUMO-derived band to higher binding energy occurs when there is sufficient K within the system to produce the K_6C_{60} phase, and the LUMO moves away from the Fermi edge as the proportion of the film in this insulating phase increases.

5.3.1 Band occupation

A number of studies (for example [126,129,134]) have used the ratio of areas of the LUMO-derived feature and fullerene HOMO for calibration of K_xC_{60} phases or to estimate charge transfer from a substrate to the fullerene cage. This approach requires the assumption that the intensity of each component in the valence band spectrum is proportional to the occupied density of states. This is valid, provided that there is little difference in the photoionisation cross-section for each of the various states, and that final-state effects which modify measured intensities are uniform across a spectrum. If both of these conditions are met, then the ratio of the measured intensities of certain states will give a direct measure of the relative occupation of those states. However, the latter condition is not met in the case of fullerene films.

The relative intensities of components in the C_{60} valence band have been observed to vary with the photon energy used to probe the system, and this has been attributed to a final-state interference effect arising from the diffraction of outgoing photoelectrons [64]. The effect has also been observed in films of $C_{59}N$ [65, 135], suggesting that it is dependent upon symmetry in the arrangement of atomic centres, rather than in the electronic structure. As such, it may be expected that this effect will persist even when there is a strong interaction with a substrate, which may cause significant rehybridisation, as is the case here. It is possible that the strength of this diffraction effect may be dependent upon

the ordering of C_{60} at a surface, and be affected by the presence of other chemical species, such as K. The effects of photoelectron diffraction may, therefore, render the approach described above untenable. Furthermore, even without the complications due to photoelectron diffraction, it can be seen in figure 5.1 that, in several of the valence band spectra, it is difficult to isolate the peak related to the fullerene HOMO from that related to the fullerene HOMO-1.

A possible alternative could be to use the ratio of the area of the LUMO-derived band to the sum of the areas of the HOMO and HOMO-1. This eliminates the problem of discriminating between the HOMO and HOMO-1 peaks, and possibly the complications arising from the photoelectron diffraction effect, as the intensities of these two peaks oscillate in antiphase as the photon energy is varied [65]. To test this hypothesis, the ratios $L : H_0$ and $L : (H_0 + H_1)$, where L, H_0 and H_1 are the integrated intensities of the the LUMO-derived feature, fullerene HOMO and fullerene HOMO-1 peaks, were evaluated as a function of K doping of the C_{60} multilayer, and for spectra obtained using two different photon energies. The areas of the various components were obtained through

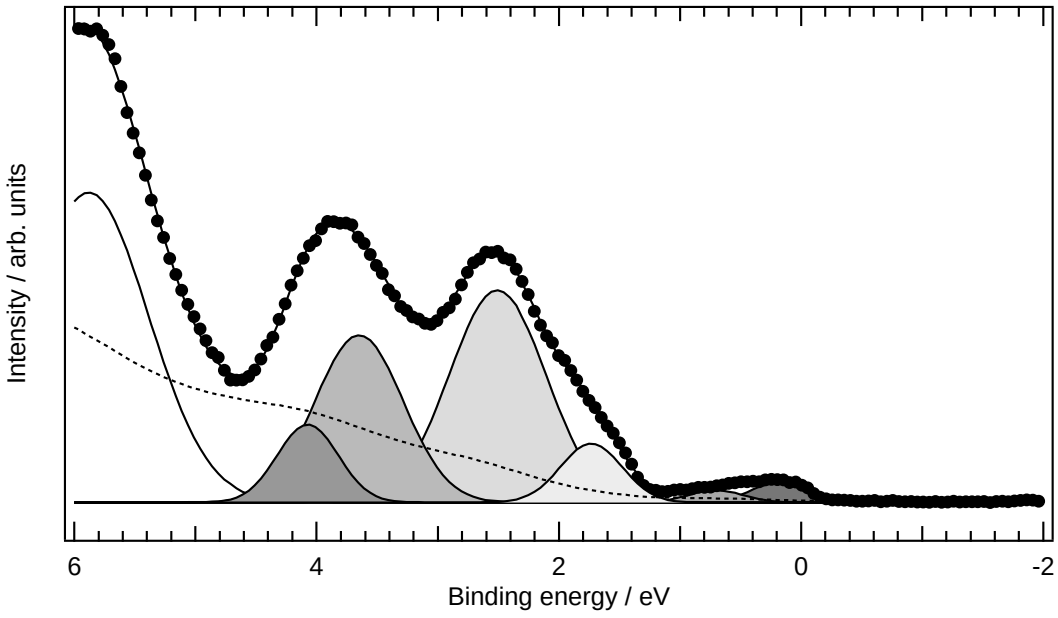

FIGURE 5.2: A curve fit, employing seven Gaussian components and 15 % integrated background, to a valence band spectrum of K_xC_{60}, for which $x \simeq 1.5$.

curve fitting to a region of each spectrum, beginning at 0.5 eV above the Fermi edge and ending at least 0.5 eV after the onset of the fullerene HOMO-3. A sample curve fit is given in figure 5.2. The function used to fit the valence band spectra is of the form:

$$f(E) = \sum_{i}^{n} A_i G_i \left(E - E_i, w_i\right) + B \int_{E_0}^{E} \sum_{i}^{n} A_i G_i \left(E' - E_i, w_i\right) \, dE' + C \qquad (5.1)$$

with n components, where:

G_i is a Gaussian function of width w_i, centred about E_i;

A_i determines the amplitude of each Gaussian contribution;

B is a constant to determine the background intensity;

E_0 is the lower bound of the region to which the fit is applied;

C is a constant offset from zero intensity.

The integral in the second term gives the correct Shirley background. However, the efficient implementation of this integral was not possible with the curve-fitting algorithm used here, resulting in very slow curve fits due to the necessity for evaluation of the integral once per point on each iteration. To a good approximation, this integral may be replaced with

$$\int_{E_0}^{E} \sum_{i}^{n} A_i G_i \left(E' - E_i, w_i\right) \, dE' \simeq \int_{E_0}^{E} I(E') \, dE' \qquad (5.2)$$

in which $I(E)$ is the measured spectral intensity at energy E. This expression is not dependent on any other parameters in the fit function, and so it need only be evaluated once for each spectrum. Its use greatly accelerates the curve-fitting process. A comparison of fits obtained using the two different expressions for the background showed no significant difference in the results. However, curve-fits executed using the original function were more strongly convergent, and more tolerant of the use of poor initial parameter guesses, due to the stronger dependence of the fit function on these parameters.

The LUMO-derived component, HOMO and HOMO-1 were each modelled with a pair of Gaussian functions, to allow for splitting and asymmetric broadening, with the width of each Gaussian matched to that of its partner to within 10%. The HOMO-3 was modelled using a single Gaussian, as only the onset of this peak was fitted. It was found that good fits could be obtained with a background contribution of between 8% and 18% of the integrated intensity.

The ratios of $L : H_0$ and $L : (H_0 + H_1)$ obtained using this curve fitting technique are presented as a function of K exposure time in figure 5.3, for valence bands measured using photon energies of 21.2 eV and 40 eV. The error bars shown in this figure are due to uncertainty in the contribution from the background function. The ratio of $L : H_0$ is clearly dependent on photon energy, whilst that of $L : H_0 + H_1$ is not. Furthermore, the latter ratio reaches a maximum value of 0.21 ± 0.05, achieved after 11 minutes of exposure to K, at which point the

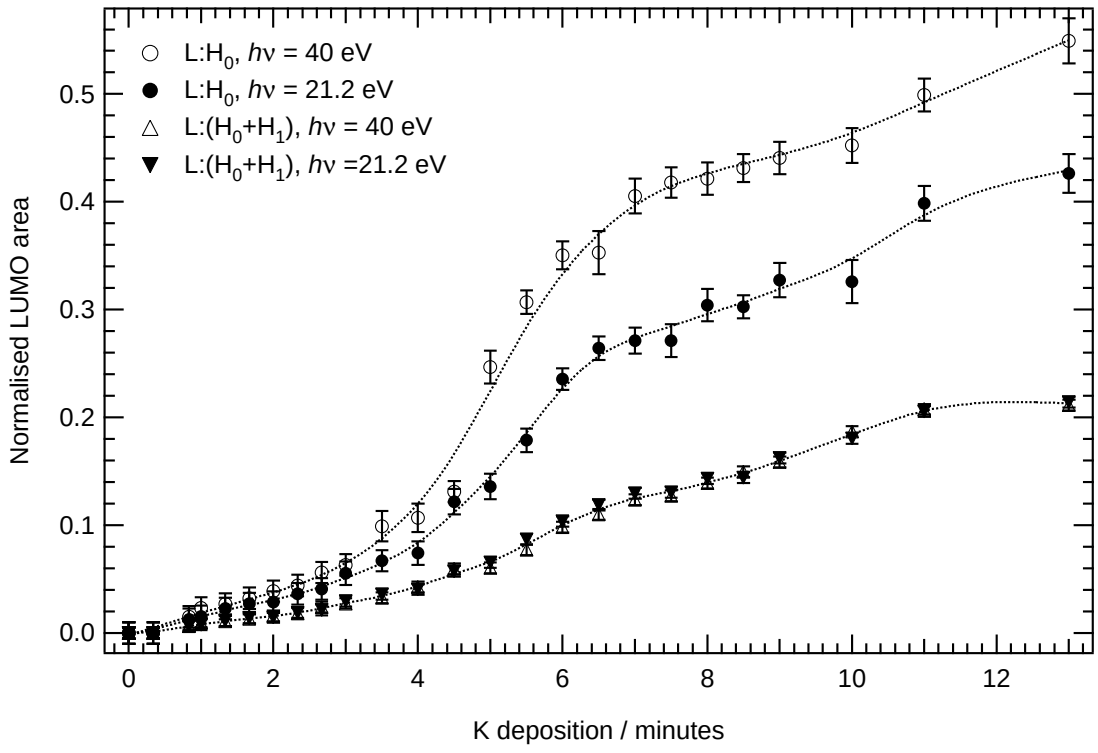

FIGURE 5.3: The ratios $L : H_0$ and $L : (H_0 + H_1)$ for a thick K_xC_{60} film, as a function of exposure to K, for photon energies of 21.2 eV and 40 eV.

film is predominantly made up of the K_6C_{60} phase. Of particular note is that this ratio is very close to the ratio of LUMO occupation to HOMO plus HOMO-1 occupation expected in this phase: six electrons in the LUMO, ten in the HOMO and eighteen in the HOMO-1 give an expected ratio of $6 : 28 = 0.214$. Averaging over multiple states has, therefore, apparently resulted in a rather fortuitous cancellation of final-state effects, such that the ratio of the integrated, measured intensities $L : H_0 + H_1$ gives a direct measure of the relative occupation of the states concerned.

5.4 K-doped C_{60}/Si(100)–(2×1) and C_{60}/Si(111)–(7×7)

Figure 5.4 shows the valence band spectra (obtained using $h\nu = 21.2$ eV) of annealed monolayers of C_{60} at the Si(100)–(2×1) and Si(111)–(7×7) surfaces, and the changes that occur as these monolayers are exposed to K. The rise in DOS beyond 0.5 eV above the Fermi level is a potassium core-level feature, excited by second-order synchrotron radiation. In both systems, all features in the valence band gradually shift to higher binding energy with increasing exposure to potassium, until the exposure time exceeds 250 s. In both the (100) and (111) case, after around 120 s of K-exposure, the LUMO-derived feature undergoes considerable broadening and, by an exposure time of 180 s, it is clear that this feature is split into two components. The major difference between the two systems is that, for low exposures to potassium, before the LUMO broadens and splits, the system on the (111) surface is metallic whilst no DOS crosses the Fermi level in the (100) system. Beyond an exposure time of 250 s, the valance band features shift to lower binding energy, such that there is some DOS close to the Fermi edge in the (100) case, and crossing it in the (111) case.

The development of DOS crossing the Fermi edge, after exposure to 250 s of K, is not accompanied by any significant change in the *shape* of the valence band spectrum. This suggests that the metallic character is not associated with any change from an insulating to conducting phase of the $K/C_{60}/Si$ system; it is more likely due to the formation of a metallic potassium overlayer after saturation of

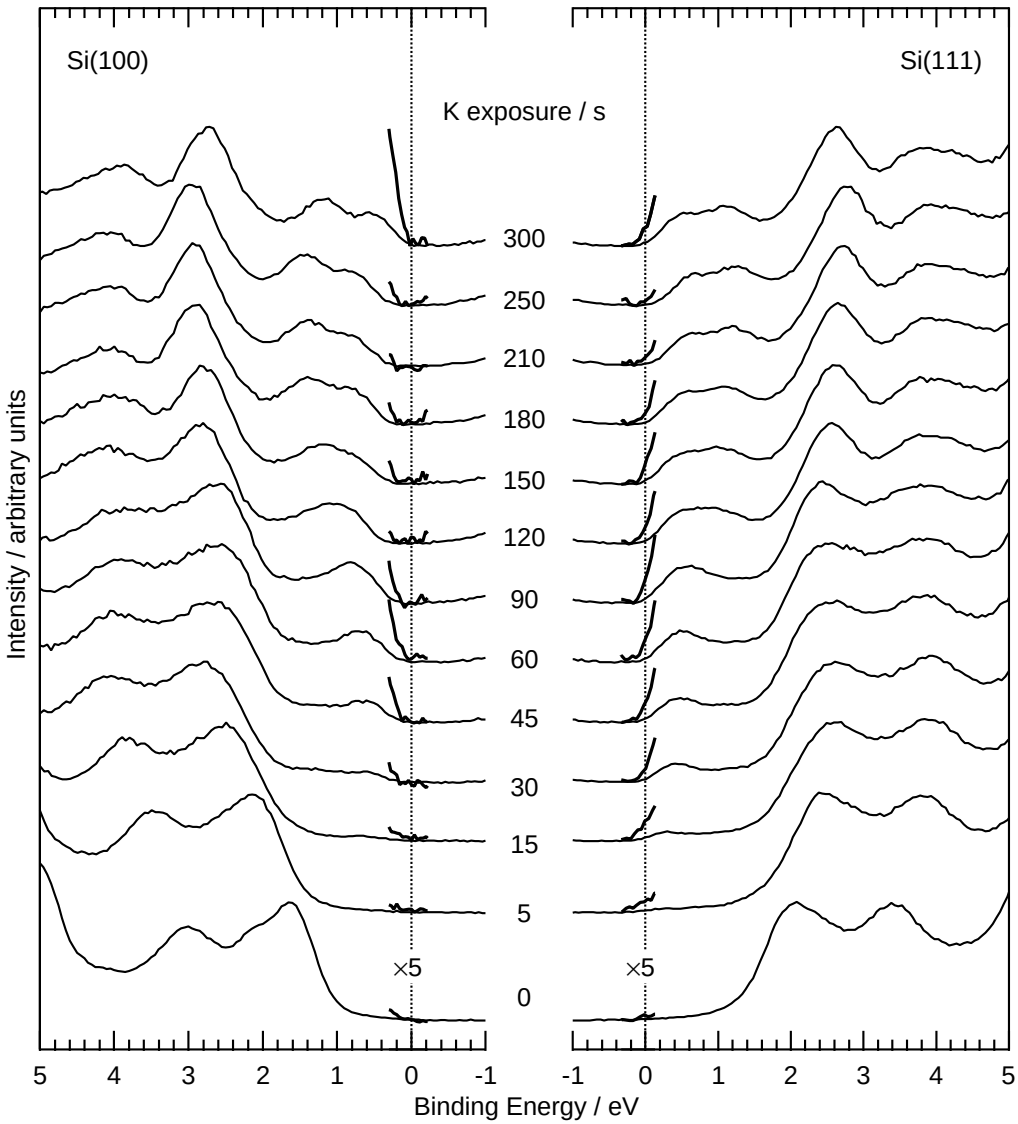

FIGURE 5.4: Valence-band spectra ($h\nu$ = 21.2 eV) of K-doped C_{60}/Si(100)–(2×1) and C_{60}/Si(111)–(7×7) with increasing K exposure.

the C_{60} monolayer.

The shape of the LUMO-derived feature for exposure times exceeding 120 s is remarkably similar to that observed by Jiang and Koel [136], for C_{60} deposited onto potassium films. In that work, the shape of this feature was attributed to the existence of phases of K_xC_{60} with $6 < x < 12$, and therefore to filling of a t_{1g}-derived band following maximum occupation of the t_{1u} band. It was suggested that such phases were possible due the potassium-rich environment. It seems unlikely that filling of a t_{1g}-derived band can account for the shape of the LUMO seen here, for the $K/C_{60}/Si$ systems. If anything, the formation of covalent bonds between C_{60} and the Si substrate would be expected to limit the co-ordination of K to C_{60}, rather than facilitate higher co-ordination to form phases of K_xC_{60} with $x > 6$. Furthermore, if such phases can be formed with C_{60} monolayers on Si, then one could expect that similar phases would be seen at the surface of C_{60} multilayers, after saturation of the bulk and development of a potassium overlayer. There is no evidence in the multilayer data to suggest this. It is more likely that the formation of covalent bonds lifts the degeneracy of the C_{60} LUMO, resulting in two discrete components.

The results observed here for low exposures of C_{60} monolayers to potassium, which show conducting behaviour at the (111) surface and semiconducting char-

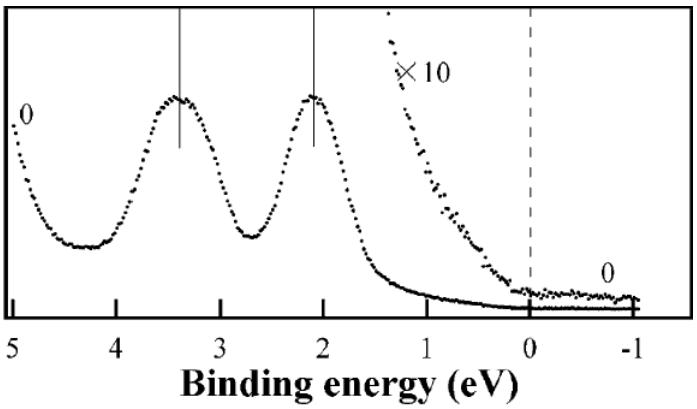

FIGURE 5.5: A valence band spectrum for an unannealed monolayer of C_{60} from [129].

acter at the (100) surface, are in direct contrast to results published by Sakamoto et al. [129] for 'physisorbed' monolayers of C_{60} at these surfaces. However, in that publication, the valence band spectra for the undoped C_{60} monolayers, an example of which is given in figure 5.5, more closely resemble those seen for C_{60} multilayers than for unannealed, sub-monolayer coverages of C_{60} at Si surfaces. The 'physisorbed' character seen in these spectra may, therefore, be due to an underestimation of the real coverage of C_{60}. The degree to which coverage is underestimated is unlikely to be consistent across measurements using the (100) and (111) substrates; the results concerning the K-doping of C_{60} at the two surfaces may therefore, in fact, be made up of inequivalent mixtures of the behaviour at the surface of a C_{60} film, at the Si/C_{60} interface, and of an uncertain number of physisorbed C_{60} layers.

The results presented here, for annealed monolayers, may be understood through consideration of the ordering of C_{60} at the two different surfaces. The ordering of cold monolayers at the Si(111)–(7×7) surface is dependent upon kinetic limitations on the growth. As monolayer coverage is reached, it is possible for C_{60} molecules that are not pinned at the corner-hole sites of the (7×7) reconstruction to diffuse, forming ordered phases in registry with those pinned at corner-hole sites [137, 138]. In this ordered phase, adsorbed molecules are almost close-packed, with intermolecular separations comparable to those in the bulk material ($\simeq$ 10 Å). At the (100) surface, however, the arrangement of the dimers in the (2×1) and $c(4 \times 2)$ reconstructions results in only local ordering of adsorbed C_{60} [138]. The molecules are packed into rhombohedral units, forming $c(4 \times 4)$ and $c(4 \times 3)$ regions [139] with an intermolecular spacing of around 12 Å. This arrangement is very different from that in bulk C_{60}. Annealing to around 300°C can promote diffusion, and therefore ordering, at the (111) surface. At the (100) surface, however, the relatively disordered arrangement of $c(4 \times 4)$ and $c(4 \times 3)$ regions is preserved after such annealing (for example, [95]). Furthermore, the absence of a metallic phase in Li_xC_{60} [140] and Na_xC_{60} [141] systems, and in studies of C_{60} doping with various other alkaline-earth metals [142], suggests that the stability of the metallic $x = 3$ phase may be dependent, at least in part,

upon the ratio of intermolecular separation to the ionic radius of the metal. It is possible that the metallic K_3C_{60} phase can stabilise at the (111) surface, since the ordering of molecules is similar to that in bulk C_{60}, whilst the very different packing at the (100) surface prevents such stabilisation. One would therefore expect a conducting state at the (111) surface, but not at the (100) surface, as is observed here. If this is the case, then it illustrates the point that the covalent C_{60}–Si bonding is considerably stronger than the ionic interaction between C_{60} and K.

5.4.1 LUMO occupation

The curve-fitting procedure described in the previous section was used to determine the ratio of $L : H_0 + H_1$, and hence the LUMO occupancy, for the C_{60} monolayers as a function of exposure time. However, neither the Shirley function (LHS of equation 5.2), nor the approximation to this function (RHS of equation 5.2), gave a sufficient description of the background contribution to the valence-band spectra of these thin films. This was the case for spectra obtained using

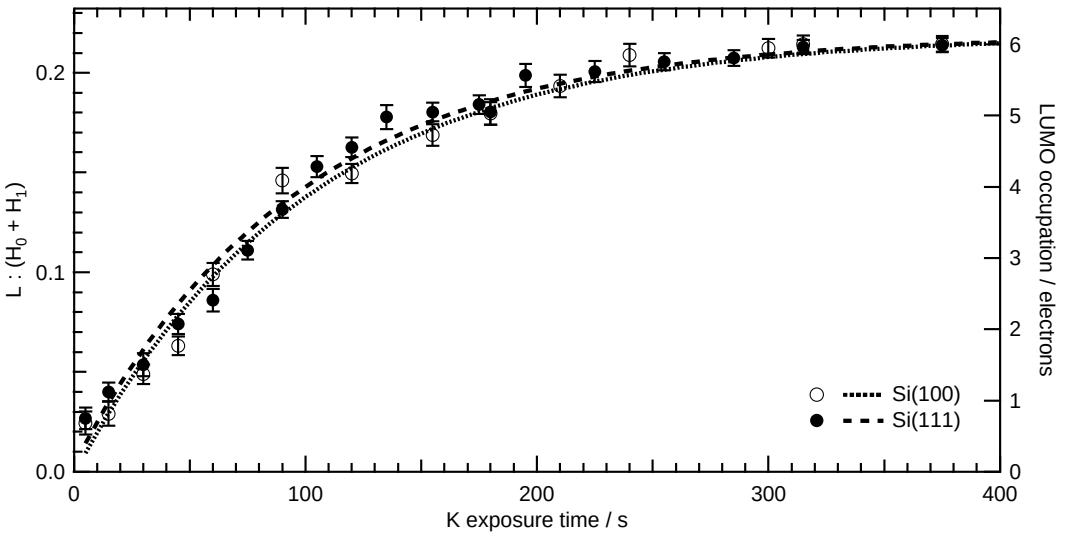

FIGURE 5.6: The electron occupation of the LUMO for C_{60}/Si(100)–(2×1) and C_{60}/Si(111)–(7×7) as a function of exposure to K, determined from $L : (H_0+H_1)$ for valence bands obtained using both $h\nu = 21.2$ and $h\nu = 40$ eV.

both $h\nu = 21.2$ eV and $h\nu = 40$ eV. At a photon energy of 21.2 eV, the $M_{2,3}VV$ Auger transition of K ($E_k \simeq 6.5$ eV) [143] is visible in the valence region, but this can not explain the poor description of the background by a Shirley function in the $h\nu = 40$ eV case. Futhermore, the presence of this peak did not appear to strongly affect results for the K-doped thick film, possibly due to the small proportion of K in the system, and the fact that very little of this K is in a metallic state. It was therefore thought that the background must contain some significant contribution from the silicon substrate. Indeed, the use of a proportion of the valence-band spectrum from the relevant clean Si surface was found to accurately account for non-zero intensity between the Gaussian components in a curve fit, yielding more convergent fits and a lower χ^2. The value of $L : H_0 + H_1$, obtained using clean-Si valence-band backgrounds and fitting to both $h\nu = 21.2$ eV and $h\nu = 40$ eV spectra, is presented in figure 5.6 as a function of exposure time. The right-hand axis in this figure shows the LUMO occupation implied by this ratio, assuming that the HOMO and HOMO-1 accomodate a total of 28 electrons. As for the bulk data presented previously, the error bars are largely due to uncertainties in the level of background contribution.

It is rather remarkable that the LUMO occupation determined by this method converges to a value of exactly 6, indicating the formation of the stable K_6C_{60} stoichiometry, for both systems. The analysis method does not appear to suffer from the shortcomings of an incomplete model of the background, as the convergence of LUMO occupation would appear to be more than coincidental. Since the background is modelled using a spectrum from the clean and reconstructed surface, the loss of features due to surface reconstruction and contributions arising from the formation of Si–C bonds and the potassium Auger (in the $h\nu = 21.2$ eV case) do not appear to be significant. Furthermore, convergence to the upper limit of 6 occurs at an exposure time of around 250 to 300 s, supporting the hypothesis that the shift occuring between these times is not related to a phase change, but that the saturation dose of K has been achieved and subsequent exposure results in the growth of a metallic potassium overlayer.

Core-level data show an interaction of K with the substrate, producing a

silicide, in both the (111) and (100) cases. A comprehensive core-level study was not carried out, and so the relative rate of K–Si reaction at the two surfaces can not be determined directly. However, the level of commensurability between the C_{60} monolayer and the Si(111)–(7×7) reconstruction is higher than that with the Si(100)–(2×1) surface, resulting in a high degree of order in the monolayer at the (111) surface, and only local ordering into small domains of $c(4\times4)$ and $c(4\times3)$ regions on the (100) surface. As a result, more Si dangling bonds reamin beneath the monolayer of C_{60} in the (100) case. If these dangling bonds were saturated *before* the formation of potassium fulleride, then the two curves in figure 5.6 would be very similar in form, but offset. Such an offset is certainly not observed here, and this suggests that reaction of K with Si and C_{60} occurs simultaneously.

The data presented in figure 5.6 show that the rate of charge transfer into the LUMO may be slighlty lower at the (100) surface than at the (111) surface, although the difference is sufficiently small to fall within the realm of experimental error. If this difference is real, then it is consistent with the argument that K–Si and K–C_{60} reactions occur simultaneosly: the larger number of dangling bonds beneath the fullerene layer at the (100) surface would then result in a lower K–C_{60} reaction rate. It can not be conclusively stated that there is a significant difference in this reaction rate at the two surfaces, but there is sufficient evidence to suggest that the K–Si and K–C_{60} reactions are concurrent. This, in turn, indicates that the strengths of the K–Si and K–C_{60} interactions are comparable. Certainly, this is consistent with the fact that the strength of the former interaction is not sufficient to displace adsorbed C_{60}, and that the latter is not so strong as to inhibit the formation of a potassium silicide.

At the point at which the LUMO-derived feature is observed to broaden and split (after an exposure of around 180 s), the occupancy of this band just exceeds a value of 4. This is consistent with the suggestion, presented above, that the reduction in symmetry of the fullerene cage, resulting from the formation of covalent bonds to the substrate, lifts the degeneracy of the LUMO. Since the LUMO splitting is observed as its occupancy exceeds a value of 4, the data suggest that the LUMO is split into one twofold-degenerate state and one non-degenerate

state, separated by approximately 0.7 eV.

5.5 Conclusion

The shortcomings of using the measured areas of the LUMO-derived band and fullerene HOMO in determining the occupation of the former have been demonstrated, and attributed to final-state effects. An alternative method of analysis has been proposed, and the results suggest that this method gives a direct measure of LUMO occupancy.

The electrical characteristics of K-doped C_{60} monolayers at the Si(100)–(2×1) and Si(111)–(7×7) surfaces are clearly different, with a conducting phase present in the latter that is not present in the former. However, the evolution of structure in the valence band in these two systems is very similar, suggesting that the conductance of alkali-doped fullerene systems is not simply dependent upon charge transfer into the fullerene LUMO, but rather on the location of dopants within that system. It has been suggested here that differences in fullerene packing result in different stabilities of the conducting stoichiometry at the two surfaces.

The data suggest that the covalent C_{60}–Si interaction is comparable in strength to that of the K–C_{60} interaction. Furthermore, the LUMO of chemisorbed C_{60} is split into two components, separated by 0.7 eV at both the Si(111)–(7×7) and Si(100)–(2×1) surfaces. It is possible that this splitting occurs due to the reduction in symmetry caused by the formation of covalent bonds between the fullerene and the substrate. Even if this is not the case, it is certain that this splitting is related to the chemisorption of C_{60}, as it is not observed in studies of K_xC_{60} in bulk form or at noble-metal surfaces.

CHAPTER 6

Interaction of Ag and Au with C_{60}/Si(111)

This chapter is concerned with the noble-metal doping of C_{60} films at the Si(111)–(7 × 7) surface. Results are presented from experimental studies of Ag and Au adsorption at the C_{60}/Si(111)–(7 × 7) surface. The interaction between C_{60} and the substrate is seen to significantly limit charge transfer between the dopant and fullerene. Furthermore, in contrast to Ag, Au interacts very strongly with the underlying Si substrate, despite the fact that the silicon is encapsulated by C_{60}. A mechanism for this reaction is proposed.

6.1 Introduction

It has been shown in chapter 5 that, when potassium is deposited onto C_{60}/Si(100)–(2 × 1) and C_{60}/Si(111)–(7 × 7), charge transfer occurs from the metal to the fullerene cage. This is in stark contrast to the behaviour of silver deposited onto

C_{60}/Si(111)–(7 × 7), where no charge transfer is observed [144], despite the fact that significant occupation of a band derived from the fullerene-LUMO is observed for C_{60} adsorbed at Ag(111), Ag(100) and polycrystalline Ag surfaces [145, 146]. Rather than interact strongly with either the substrate or the fullerene, Ag forms clusters at the surface of the C_{60} monolayer [144]. This raises the question as to whether or not this behaviour is specific to silver, or whether it is common to other metals of a similar reactivity. Here, the interactions of Ag and Au with covalently bound monolayers at the Si(111)–(7 × 7) surface are presented and compared. The results consist of two studies of the independent adsorption of Ag and Au, and an investigation of co-adsorption.

6.2 Experimental details

The studies of independent adsorption were carried out at beamline 4.1 of the Daresbury SRS (§3.4.1). Valence bands were obtained using photon energies in the range of 21.2 eV to 55 eV, whilst the Si 2p and Au 4f core levels were probed using $h\nu$ = 140 eV. The Fermi edge of a Ta clip on the sample holder was used for calibration of binding energy, and an overall experimental resolution of around 250 meV was achieved. For the purposes of calibration of fullerene coverage, a Mg $k\alpha$ X-ray source was used to obtain C 1s core-level spectra, since the monochromator on beamline 4.1 does not provide sufficiently high photon energies to access this core level. The studies involving Ag used electron-beam sample heating, whilst those relating to Au employed direct, resistive heating, due to variation in equipment availability.

The co-adsorption study employed beamline MPW 6.1 of the Daresbury SRS (§3.4.3). As before, valence bands were obtained using photon energies between 21.2 eV and 55 eV, Si 2p and Au 4f core-level spectra at 140 eV. On MPW 6.1, the C 1s core-level is accessible using synchrotron radiation; measurements of this level were carried out using $h\nu$ = 350 eV. A better overall experimental resolution of 180 meV was achieved. Sample annealing was facilitated by direct sample heating.

		Deposition rate / ML min^{-1}	
	T / °C	adsorption	co-adsorption
Ag	860	1.0± 0.3	0.3 ± 0.1
Au	1065	6.0± 1.8	0.10± 0.03

TABLE 6.1: Deposition temperatures and rates of Ag and Au during the adsorption (beamline 4.1) and co-adsorption (beamline MPW 6.1) experiments.

All measurements used substrates of B-doped Si, with a dopant density of 10^{16} cm^{-3}. The Si(111)–(7 × 7) reconstruction was prepared as described in section 3.5.1. C_{60} was deposited from Ta envelope dispensers; monolayers were prepared by annealing a multilayer at 300°C, yielding an *annealed monolayer*, and by building up the C_{60} coverage via successive sub-monolayer depositions to give a *cold monolayer*. The deposition rate on both beamlines was found to be 0.1±0.02 ML min^{-1}. Au and Ag were deposited from Knudsen cells at 1065°C and 860°C, respectively. Deposition rates were calculated according to the parameters of the Knudsen cells and the experimental geometry of each beamline end station and, in the case of Ag, verified by *ex situ* atomic force microscopy (AFM). These rates are given in table 6.1.

6.3 Adsorption of Ag at C_{60}/Si(111)–(7 × 7)

Figure 6.1 shows the evolution of the valence band and Si 2*p* core level with increasing coverage of Ag on an annealed monolayer of C_{60} at the Si(111)–(7 × 7) surface. Spectra for the clean Si(111)–(7 × 7) surface and the annealed C_{60} monolayer are included for reference.

Upon deposition of 0.5 ML Ag, peaks in the valence-band region shift by 0.4 eV to higher binding energy. No further shift occurs with the deposition of additional Ag up to a coverage of 9.0 ML, but the peaks associated with the fullerene HOMO and HOMO-1 become less distinct. The loss of definition in these peaks occurs at high coverages of Ag due to the increased contribution to the spectrum from Ag valence states. The 0.4 eV shift of components in the valence band is the net result of two processes, as discussed by Owens et al. [147]

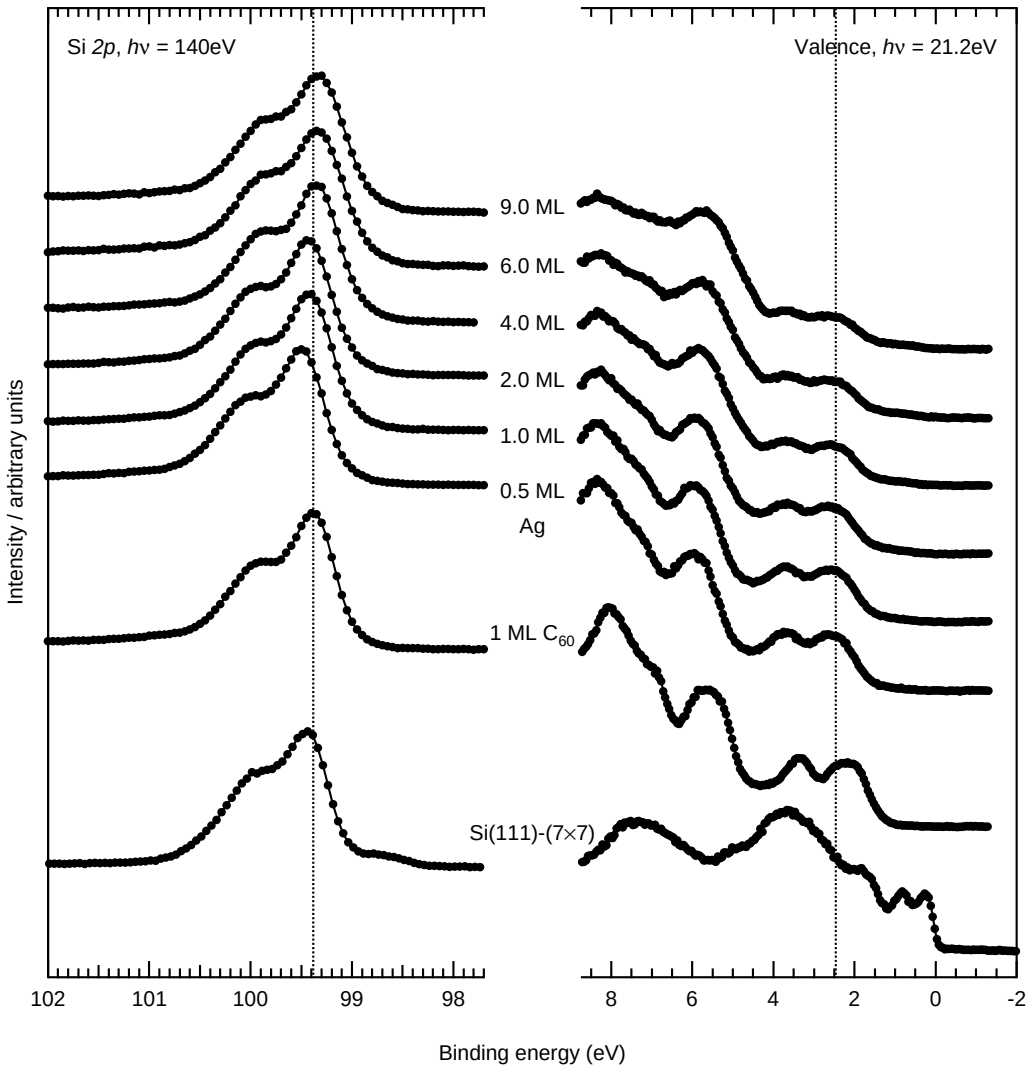

FIGURE 6.1: Valence band and Si $2p$ core-level spectra, as a function of Ag coverage.

for the case of Al adsorbed at the surface of thick C_{60} films. Electrons are donated from the adsorbed metal to the fullerene, occupy a band derived from the fullerene LUMO and cause movement of the Fermi level, resulting in a positive binding energy shift. These same donated electrons also enhance screening of outgoing photoelectrons from the fullerene system, producing a negative binding energy shift.

There is negligible density of states at the Fermi edge. Comparison of the Fermi-edge region at different photon energies suggests that the intensity here is largely due to metallic Ag. Figure 6.2 shows the Fermi edge after adsorption of 1 ML and 8 ML Ag, and measured at photon energies of 21.2 eV and 55 eV. The spectra are normalised to the intensity of the peak related to the fullerene HOMO. The relative cross-sections of the Ag valence states to those of C are considerably greater at 55 eV than at 21.2 eV, and it is clear that the intensity of the Fermi edge, relative to that of the fullerene HOMO-derived peak, is much greater in the spectra taken at 55 eV. The lack of significant fullerene-related density of states at the Fermi edge indicates limited charge transfer from the adsorbed Ag

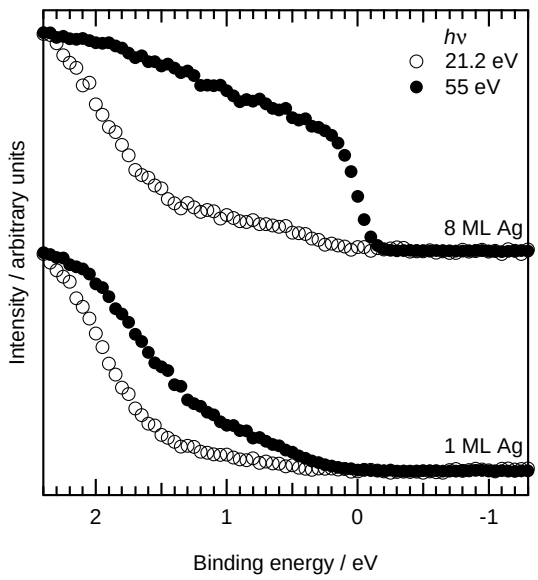

FIGURE 6.2: The Fermi edge of 1 ML and 8 ML Ag on an annealed C_{60} ML, obtained with photon energies of 21.2 eV and 55 eV.

to the fullerene, in stark contrast to that observed upon the adsorption of C_{60} at the Ag(111) surface [146]. This suggests that the valence band shift due to movement of the Fermi edge is small. The fact that an overall shift occurs to higher binding energy demonstrates that screening processes at the surface of Ag/C60/Si(111)–(7×7) system are rather inefficient.

The Si $2p$ core-level spectra presented in figure 6.1 are normalised to the intensity of the main peak. As Ag is adsorbed, small shifts in the position of the core level are observed, arising due to band bending. Up to 4.0 ML of Ag, there are no discernible changes in the line shape of the Si $2p$ core level, compared to that observed for the undoped, adsorbed C_{60} monolayer. At a coverage of 9 ML of Ag, small changes in the line shape can be detected. However, these changes are subtle and most likely arise from attenuation of the Si photoemission signal by the adsorbed Ag. This also accounts for the slight increase in the width of the core level as more Ag is deposited. Certainly, there are no features in the evolution of the Si $2p$ core level that suggest a significant interaction of the adsorbed Ag with the substrate. The lack of such an interaction is particularly noteworthy, as it suggests that the adsorbed Ag atoms reside on top of the C_{60} monolayer — adsorption is not localised at defects in the monolayer, where dangling bonds from the underlying substrate may be exposed. This is entirely consistent with STM studies, which show that adsorbed Ag atoms coalesce to form clusters at the surface of the C_{60} monolayer [144].

6.4 Adsorption of Au at C_{60}/Si(111)–(7×7)

Figure 6.3 shows the valence band and Si $2p$ core-level spectra of the clean Si(111)–(7×7) surface, 5.0 ML C_{60} and a monolayer of C_{60}, produced by annealing the multilayer using direct heating, before and after deposition of 5.0 ML Au. The Au $4f$ core-level spectrum, after deposition of the Au, is given in figure 6.4. There are some minor differences in the Si $2p$ core-level and valence band spectra for the monolayer annealed by direct heating, compared to that annealed using electron-beam heating; these have been discussed in section 3.6.

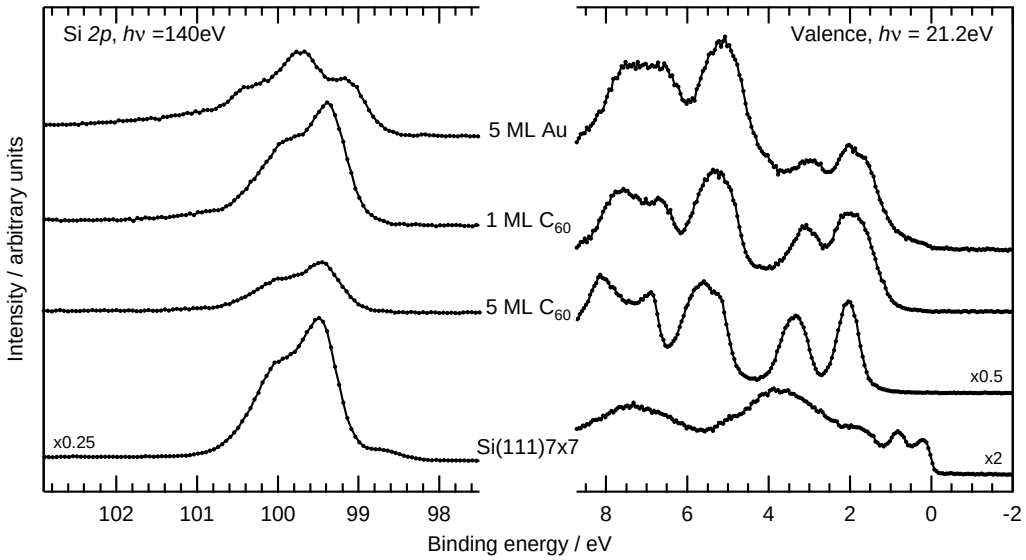

FIGURE 6.3: Valence band and Si $2p$ core-level spectra for 5 ML Au deposited onto an annealed C_{60} monolayer. Other spectra are included for reference.

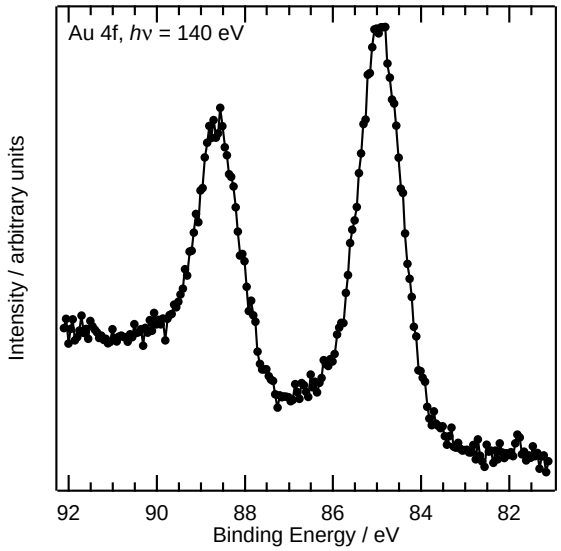

FIGURE 6.4: The Au $4f$ core-level spectrum for 5 ML Au on an annealed C_{60} monolayer.

After deposition of 5.0 ML Au onto the annealed monolayer, there is a dramatic change in the Si $2p$ core-level spectrum, indicative of a reaction of the Au with the underlying Si. There are also changes in the valence band, in the region of the fullerene HOMO. The behaviour of Au at the C_{60}/Si(111)–(7×7) surface observed here is very different to that of Ag; however, at this point, it may be that the difference in behaviour arises due to differences in the quality of the monolayer: defects in the C_{60} monolayer arising from its annealing may expose regions of the substrate, allowing the Au to react at these sites and form a silicide. In order to address this possibility, the experiment was repeated, using a cold monolayer of C_{60}, prepared without any annealing.

Figure 6.5 shows the valence band, Si $2p$ and (where appropriate) Au $4f$ core-level spectra for a series of depositions of Au onto a cold monolayer of C_{60}. The valence band spectrum for the C_{60} layer is consistent with that found in the

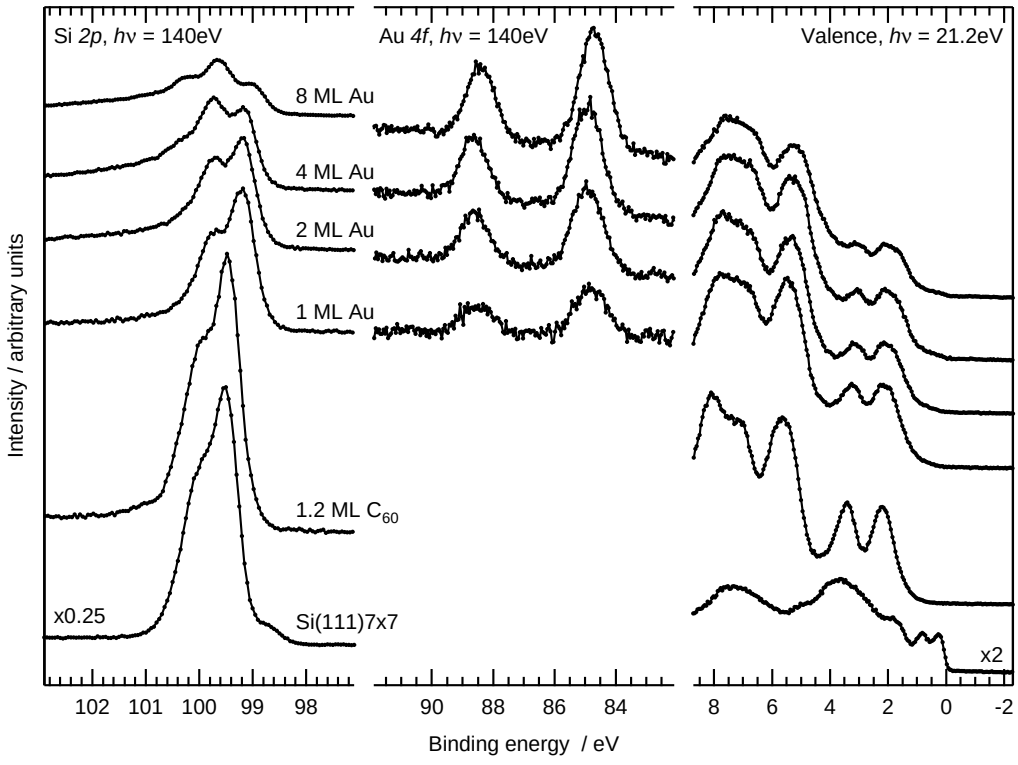

FIGURE 6.5: Valence band, Au $4f$ and Si $2p$ core-level spectra as a function of Au coverage on 1.2 ML unannealed C_{60}.

literature; a comparison of the valence band observed for this type of monolayer to those observed for monolayers produced by annealing is presented in section 3.6.1. The C_{60} coverage is, in fact, just over a monolayer (1.2 ML), as it was prepared by repeated sub-monolayer depositions. This is beneficial, as it ensures the presence of at least one complete chemisorbed layer of C_{60} at the Si surface.

Despite the fact that, in this system, saturation of the Si surface is guaranteed, and that there can be no thermally induced defects, a strong interaction of adsorbed Au with the Si substrate is still observed. After the first deposition of Au, the Si 2*p* core level undergoes a shift of 0.3 eV to lower binding energy. Such a shift is most likely due to the effects of band bending. The magnitude of this shift increases as further Au is deposited. At coverages of 4.0 ML of Au and beyond, the Si 2*p* core-level spectrum is dominated by a feature to higher binding energy, associated with the formation of a Au-silicide [148–150]. In the valence band, the HOMO broadens considerably as Au coverage is increased and, at higher coverages, it is apparent that it has split into two components; that at the lowest binding energy gradually shifts closer to the Fermi edge.

Figure 6.6 shows curve fits to the Si 2*p* core-level spectra of the 1.2 ML

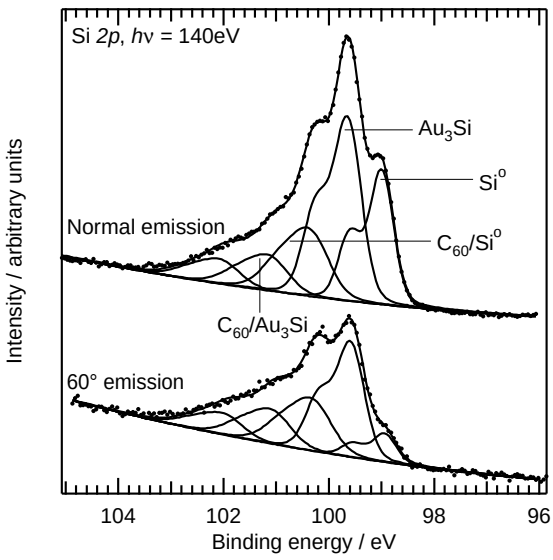

FIGURE 6.6: Curve fits to the Si 2*p* core-level spectra of 8 ML Au on 1.2 ML unannealed C_{60} at normal and grazing emission,

of unannealed C_{60} after deposition of 8.0 ML Au, at both normal and grazing emission. The fits involve five spin-orbit split Voigt-doublets. The branching ratio and spin-orbit split for these doublets were obtained from a fit to data for the clean Si(111)–(7 × 7) surface. The component (Si^0) at 99 eV is attributed to bulk silicon: the width of this component is consistent with that observed in the case of the clean surface, and its intensity is greatly reduced with the increased surface sensitivity of the grazing emission geometry. The dominant peak is broader than that associated with bulk Si, and lies at a RBE of +0.6 eV, with respect to the bulk line. This shift is consistent with that observed when gold silicide (Au_3Si) forms as a result of deposition of Au onto the clean Si(111)–(7 × 7) surface [148–150], and with results from thermodynamic calculations of core-level binding energies [151].

Three components are required to provide sufficient width in fitting the high binding-energy tail of these spectra. These components lie at RBEs of +1.0, +2.0 and +3.0 eV. Shifts of around +1 and +2 eV are observed upon the adsorption of C_{60} at the Si(111)–(7 × 7) surface [152]; in that system, they are attributed to the formation of Si–C bonds, and it is very likely that these bonds contribute to the +1.0 eV component and, at least in part, to that at +2.0 eV observed here. However, the relative intensity of the +2.0 eV component is considerably larger than that expected than if it were due to the formation of Si–C bonds, alone: there is clearly some contribution from some other chemical component in the system. Furthermore, the origin of the peak at +3.0 eV is not clear. It has been suggested that intensity in this region arises from the formation of non-stoichiometric Au_xSi, due to changes in the oxidation state of Si brought about by the presence of Au. Such an intense high binding-energy tail is not observed when gold silicide forms at the clean Si(111)–(7 × 7) surface, however. This suggests that the +3.0 eV component and additional intensity at +2.0 eV are fullerene-related, rather than intrinsic to the Au–Si system. Differences between the spectra seen here and those for C_{60}/Si(111)–(7 × 7), outlined in previous chapters, indicate that these components are also dependent on the presence of Au. They must therefore come about from some tri-special interaction of Au,

C_{60} and Si. It is possible to conceive of many combinations of these three species but, from the Si $2p$ core-level data presented, the chemical nature of the complex occurring here can not be unequivocally determined.

The Au $4f$ core-level spectra of a thick Au film, a thin film of Au on Si(111)–(7×7), and 8.0 ML Au on the cold C_{60} monolayer are compared in figure 6.7. The thick film spectrum can be fitted using a single spin-orbit split component, with a branching ratio of 1.5 and a split of 3.73 eV. The thin film on Si(111)–(7×7), however, contains two discrete spin-orbit split components: in the spectrum shown here, the smaller-intensity peak is due to unreacted, metallic Au; the larger peak has a RBE of +0.68 eV. This shift is attributed to the formation of gold silicide, and is consistent with published data [148–150]. The fit to data obtained from the Au/C_{60}/Si(111) system shows that the majority of Au exists in the silicide form. A small component to lower binding energy indicates the presence of a small amount of Au in the metallic state. It has been observed previously in Au/Si(111) systems that the first three monolayers of Au stabilise a surface silicide; additional Au nucleates below this silicide layer to form the metallic phase [148]. This may be the case here, with metallic Au residing at the

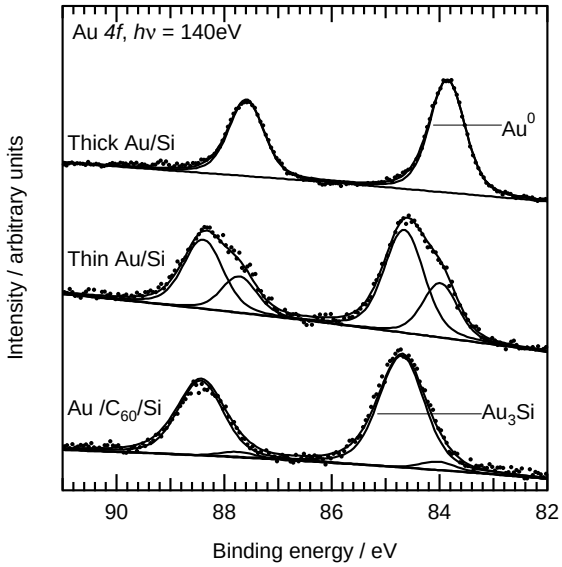

FIGURE 6.7: Curve fits to the Au $4f$ core-level spectra of thick and thin films of Au at the Si(111)–(7×7) surface, and of 8 ML Au on 1.2 ML unannealed C_{60}.

silicon interface, below the silicide and fullerene; however, further measurements are required to confirm this.

As for Ag on the C_{60}/Si(111)–(7×7) surface, there is little density of states at the Fermi edge, and that which can be seen is attributed to the presence of unreacted, metallic Au. Evidence for this is given in figure 6.8, which shows the Fermi edge region for 1.0 and 8.0 ML Au deposited onto the C_{60}/Si(111)–(7×7) surface, and measured using photon energies of 21.2 and 55 eV. The spectra in this figure are normalised to the intensity of the fullerene HOMO. Between photon energies of 21.2 and 55 eV, there is a significant reduction in the cross-sections for carbon-related photoelectron excitations, but not for those related to the Au. As for the case of Ag/C_{60}/Si(111)–(7×7), there is an increase in the intensity at the Fermi edge in moving from 21.2 to 55 eV, suggesting that intensity in this region arises due to the deposited metal, rather than occupation of higher states on the fullerene cage.

It is clear from the data presented here that, in contrast to the Ag/C_{60}/Si(111)–(7×7) system, there is a strong chemical reaction between the Si substrate and deposited Au, despite the presence of the C_{60}. The deposited Au penetrates the

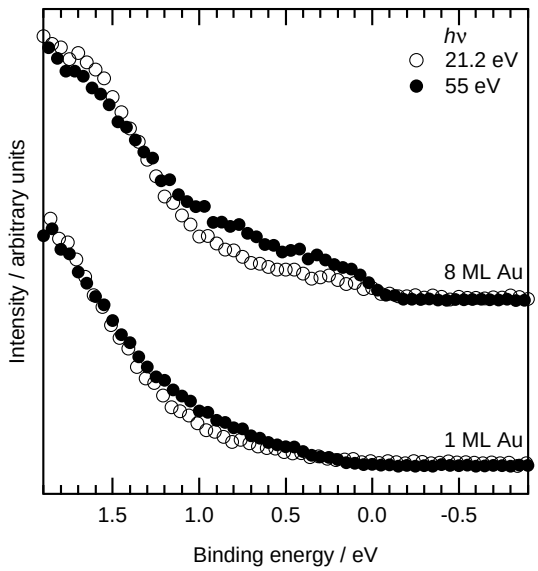

FIGURE 6.8: The Fermi edge of 1 ML and 8 ML Au on 1.2 ML unannealed C_{60}, obtained with photon energies of 21.2 eV and 55 eV.

layer of C_{60} by some mechanism (to be discussed later), such that the C_{60} layer rests above the resulting silicide. This is evident from the fact that considerable intensity arising from fullerene related states can still be seen in the valence band (figure 6.5), even after the deposition of 8.0 ML of Au.

6.5 Co-adsorption of Ag and Au at C_{60}/Si(111)–(7×7)

The studies of adsorption of Ag and Au at the C_{60}/Si(111)–(7×7) surface show that the two metals behave very differently. It is reasonable to suggest that the difference in observed behaviour may come about due to variations in the quality of the C_{60} monolayers used in each investigation. For this reason, the investigations discussed in the preceding sections were repeated, using a different beamline but identical sample preparation procedures; the results were consistent with those discussed in the preceding sections. However, this does not address the possibility that, even with identical preparation, the quality of a C_{60} monolayer may vary from sample to sample. In order to rule out the effects of such variation, measurements were carried out with Ag and Au co-adsorbed at a C_{60}/Si(111)–(7×7) surface.

Figure 6.9 shows a series of Si $2p$ core-level spectra for the clean Si(111)–(7×7) surface, an annealed monolayer of C_{60} at this surface in its clean state, and after depositions of Ag then Au. The monolayer was prepared by annealing a multilayer to 300°C, using direct heating. After deposition of 1.2 ML of Ag, there is little change in the core-level spectrum, which is consistent with the data from an e-beam annealed monolayer, presented in section 6.3. Subsequent depositions of Au, on the other hand, are seen to produce large changes in the core-level spectrum, again consistent those seen due to the formation of gold silicide, in section 6.4. This is a significant result, as it confirms that the very different behaviours of Ag and Au at the C_{60}/Si(111)–(7×7) surface are genuinely specific to each metal, rather than arising a result of variations in the quality of the C_{60} monolayer.

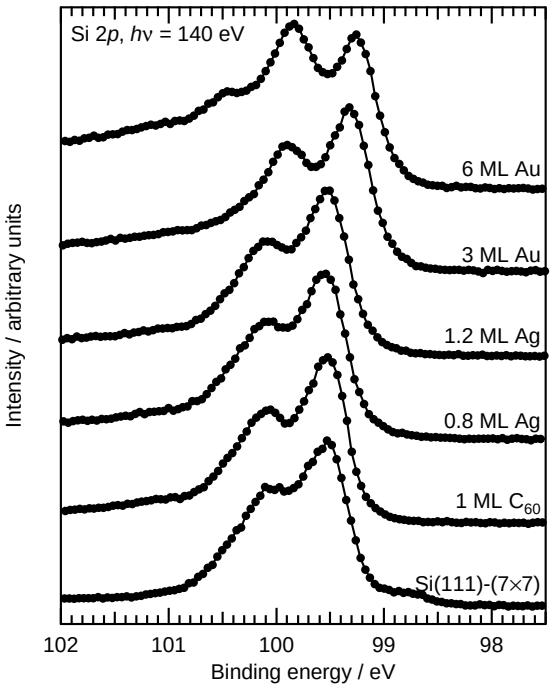

FIGURE 6.9: Development of the Si 2*p* core level upon deposition of 1.2 ML Ag, followed by Au.

6.6 Discussion

The data presented here clearly show the different behaviour of Ag and Au when deposited at the C_{60}-terminated Si(111)–(7×7) surface. In the case of Ag, there appears to be little interaction of the metal and the silicon substrate. In contrast, Au reacts with the substrate to form a silicide, despite the presence of the layer of C_{60}. This is hardly an intuitive result, since the 'encapsulation' of reactive surfaces using fullerenes has been shown to inhibit reactions involving the surface of the substrate, such as oxidation [152].

The interaction between C_{60} and Si(111)–(7×7) is strongly covalent, and involves little charge transfer, whereas that which occurs between C_{60} and Ag or Au surfaces is ionic, characterised by a strong charge transfer [145, 153–155]. In the case studied here, however, valence band spectroscopy reveals negligible charge transfer to the fullerene cage from either of the two noble metals. With respect to their interaction with the C_{60} in this system, both metals behave very

similarly: there is little interaction in either case. This metal-fullerene interaction can not, therefore, explain the very different behaviour of these two noble metals at the C_{60}/Si(111)–(7×7) surface, in particular why one of the metals penetrates the covalently bound fullerene layer, in order to react with the substrate, whilst the other does not.

An explanation for the different behaviours can be conceived if it is assumed that reaction of Au with the silicon substrate nucleates primarily at step edges and domain boundaries on the C_{60}-terminated surface. In such regions, silicon atoms may be exposed, and the behaviour of the deposited metal then depends solely upon the strength of its interaction with silicon. Below temperatures of 500 K, Ag does not readily react with silicon, preferring nucleation to form islands or clusters, followed by epitaxial growth. Au, on the other hand, readily forms a silicide. If this reaction nucleates at defects such as step edges, and if the strength of the Au–Si interaction is comparable to that of C_{60}–Si bonding, fullerene molecules may be displaced, disrupting the surface and making more silicon available for reaction with Au. Once a layer of silicide exists, additional Au is able to diffuse from the disrupted surface, into the sample and to the silicide–silicon interface.

6.7 Conclusion

The interaction of silver and gold at the C_{60}-terminated Si(111)–(7×7) surface differs greatly. Common to both metals is the lack of any strong interaction with the fullerene cage, which contrasts strongly with the high degree of charge transfer that is observed between noble metal surfaces and adsorbed fullerenes. The silver demonstrates inert behaviour, residing above the fullerene layer and forming nanoscale clusters. Conversely, gold penetrates the fullerene layer in order to react with the substrate. It is proposed that this reaction initiates at domain boundaries, step edges and defects within the C_{60} layer, and leads to the displacement of the fullerene molecules and the formation of Au_3Si. These contrasting results demonstrate that the deposition of metals, a conventional

method of doping, is subject to limitations when applied to the modification of the electronic structure of covalently-bound fullerene films: the intrinsic properties of the dopant or its interaction with more reactive components within the system may dominate, possibly due to the fact that the fullerene itself is rather inert.

In the case of Au, the nature of the interaction between C_{60} and the surface that results from the reaction of Au and Si is not clear. Certainly, the silicon core-level spectra reveal the presence of what are most likely C_{60}–Au–Si complexes. A detailed study of the states of carbon at this surface, using high-resolution PES to probe the C $1s$ core level, may provide further insight in this area. It is clear that, after deposition of several monolayers of Au, some metallic Au is present in the reacted system. The location of this metallic gold is not clear: it is possible that it resides between the silicon and the silicide, as has been observed in the case of silicide growth on clean Si(111)–(7×7). Whether or not this is the case in this system could be ascertained through a study of the Au $4f$ core-level by PES, at higher coverages of Au than those considered here, and at varying emission angles. A study of the topography of the resulting surface, using STM or AFM, may also be worthwhile. In particular, if the fullerene molecules can be removed by some non-aggressive means, it may interesting to compare the underlying silicide to that formed by straightforward deposition of Au onto the Si(111)–(7×7) surface: the presence of the fullerene during formation of the silicide may result in differences, perhaps due to some manner of surfactant-mediated growth.

CHAPTER 7

Multiphenylated C_{60}

In this chapter, studies of a multiphenylated fullerene, $(C_6H_5)_5C_{60}H$, are discussed. The key issue that is addressed is the effect of the phenyl groups on fullerene electronic structure and chemical behaviour. The results show that dramatic changes in the electronic structure of the fullerene cage result from phenyl functionalisation. The degeneracy of the electronic states is lifted, the HOMO–LUMO band gap widened, and there is some evidence to suggest profound changes in the chemistry of the fullerene cage itself, rather than the simple introduction of phenyl chemistry to the fullerene system. Results from PES also suggest that the presence of the phenyl groups enhances the polarisation screening seen in C_{60} films. Adsorption at the Si(111)–(7×7) surface is similar to that of C_{60}, involving the formation of covalent bonds, whilst at the Ag:Si(111)–$(\sqrt{3} \times \sqrt{3})R30°$ surface, $(C_6H_5)_5C_{60}H$ behaves as an electron donor.

7.1 Introduction

As discussed in some detail in previous chapters, the modification of fullerene molecules, through a variety of methods, offers the potential to tune various physical characteristics. The addition of functional groups to the fullerene cage is of particular interest. Functionalisation offers a far greater scope for modification than either doping, both exohedral and substitutional, or encapsulation, due to the large variety of functional groups available, and the possibility of varying the number of groups attached to a cage, and their locations. Through variation of such parameters, it is conceivable that the ordering of fullerenes, both within the bulk material and at surfaces, may be tuned. The ability to vary the intermolecular separation within the material is of particular importance, as it facilitates the investigation of the interplay of conventional delocalised band formation and electron correlation in fullerene systems. Furthermore, controlled modification of the lattice constant of a fullerene-based molecular system changes the density of states at the Fermi level. This, in turn, has important implications for the modification of the critical temperature of superconducting fullerides [128, 157], although, once again, the importance of electron correlation should not be overlooked — the on-site Coulomb interaction in fullerene solids is much larger than

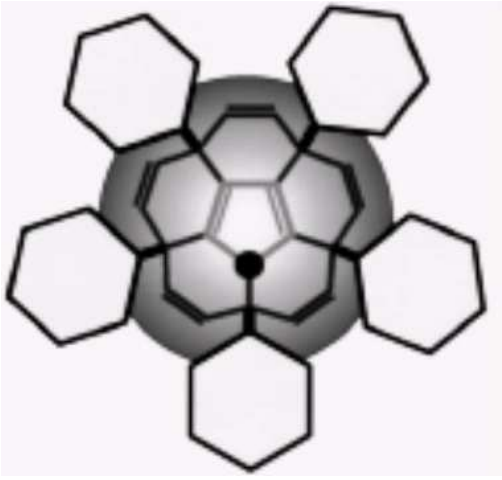

FIGURE 7.1: The bonding sites of the phenyl groups and hydrogen, represented by the filled circle, in $(C_6H_5)_5C_{60}H$ (after [156]).

the width of the conduction band. An important issue to address is whether cage functionalisation is an effective route to lattice constant variation. We must then ask not only how the presence of the functional groups affects molecular packing [158], but how the electronic structure of the fullerene molecule is modified. Moreover, there are also a variety of surface science issues to be addressed: how do the phenyl groups affect adsorption, specifically molecular orientation, and is there any possibility of surface functionalisation using fullerenes modified in this way?

The functionalised fullerene of interest in this study, $(C_6H_5)_5C_{60}H$ [156], is illustrated in figure 7.1. The five phenyl groups and single hydrogen cause rehybridisation of six of the carbon centres in the fullerene cage, from sp^2 to sp^3. This rehybridisation results in a change in the alternation pattern of double and single bonds around the cage, affecting at least 20 carbon centres.

7.2 Experimental

The experimental work presented here was carried out at beamline 5u1 (§3.4.2) of the Daresbury Laboratory Synchrotron Radiation Source. A 120 mm hemispherical analyser from PSP [72] was used for PES measurements, and NEXAFS was carried out in total yield mode. The monochromator and analyser afforded an overall experimental resolution of order 150 meV at a photon energy of 140 eV. All measurements were carried out under UHV conditions, and the samples were prepared *in situ*, as discussed in chapter 3.

$(C_6H_5)_5C_{60}H$ was deposited from a K-cell at a temperature of 350°C. Multilayer coverages were obtained by deposition of material until the Si $2p$ peak was not visible in core-level measurements obtained at a photon energy of 140 eV. STM results have shown that, as for C_{60}, annealing a multilayer of $(C_6H_5)_5C_{60}H$ at the Si(111)–(7×7) surface, at a temperature of 300°C, results in desorption of excess fullerene to leave one complete monolayer [158]. Sub-monolayer coverages were estimated by comparison of the Si $2p$ to C $1s$ total area ratio to that observed for the annealed monolayer.

7.3 Results

7.3.1 Bulk $(C_6H_5)_5C_{60}H$

The C 1*s* core-level spectrum of a thick $(C_6H_5)_5C_{60}H$ film is shown in figure 7.2, taken at both normal emission and 60° off normal emission. The figure also shows multivariate curve fits to the data, after the subtraction of a secondary electron background. The subtraction of a Shirley type background alone was not sufficient to eliminate all contributions due to secondary electrons — a steadily increasing gradient remained. For this reason, the backgrounds shown here were

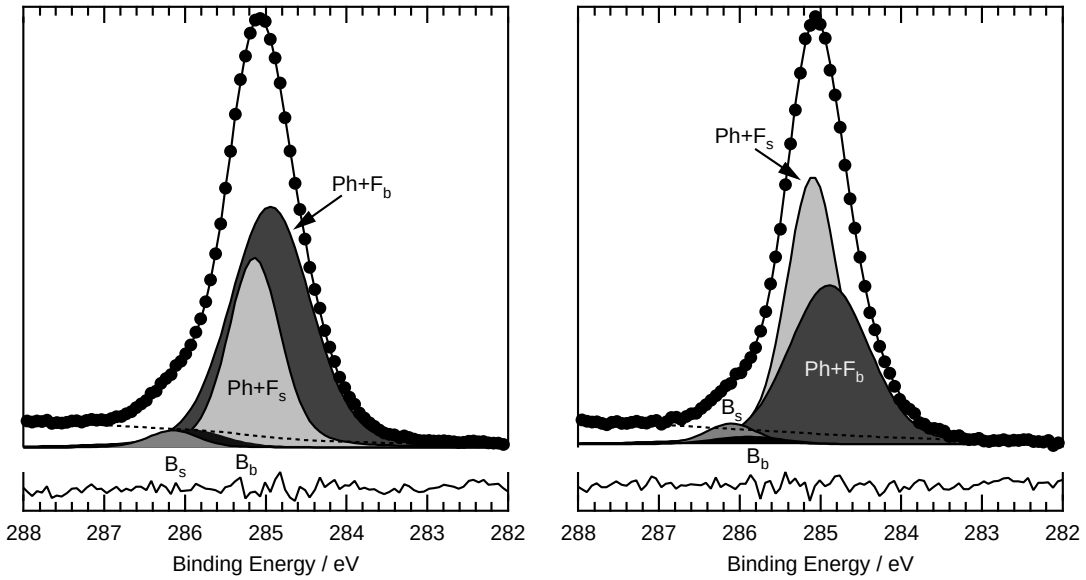

FIGURE 7.2: C 1*s* core-level of bulk $(C_6H_5)_5C_{60}H$ taken at normal emission (a) and 60° off normal emission (b).

Component	Energy / eV	Γ_G / eV	Total area/% NE	Total area/% +60°	Partial area/% NE	Partial area/% +60°
Ph+F_b	285.14	1.06	60	44	94	96
B_b	+1.01	0.88	4	2	6	4
Ph+F_s	+0.20	0.64	33	50	92	93
B_s	+1.21	0.61	3	4	8	7

TABLE 7.1: Fitting parameters for the curve fits shown in Figure 7.2. The Lorentzian width (Γ_L) was fixed at 215 meV.

obtained from the sum of a Shirley function and a polynomial of order three, the parameters for which were chosen to match the *gradient* of the raw data (rather than its intensity) far from the core-level.

A minimum of three Voigt components were required to obtain a good fit to these spectra. However, a physical justification of the characteristics of the components resulting from a three component fit is difficult. It is reasonable to expect discrete contributions to the C 1*s* core level from (at least) carbons of type sp^2 in the phenyl groups ('phenyl' — constituting 33% of all carbon in the molecule), sp^x where $2 < x < 3$ in the fullerene cage ('fullerene' — 60%) and sp^3 which take part in bonding from the fullerene cage to the phenyl groups ('bonding' — 7%). However, it is not likely that the separate contributions from phenyl and fullerene carbons may be resolved. The resolvable features would therefore include one component encompassing both the phenyl and fullerene contributions (*Ph+F*), and one due to the bonding carbons (*B*). The latter would lie at around 0.8 to 1.2 eV higher binding energy, due to the shift associated with sp^2 and sp^3 hybrids [159]. However, a splitting of the order of 0.1 eV between the surface and bulk related C 1*s* components has previously been observed [63] for C_{60} films. This splitting arises from the differences in total final-state energy, due to core hole induced molecular polarisation, for molecules at the surface and in the bulk of a fullerene thin film. Taking this difference in polarisation screening into consideration, two pairs of *Ph+F* and *B* components are expected, with one pair shifted by at least 0.1 eV to higher binding energy.

Four Voigt components were used in a simultaneous fit to the normal and grazing emission spectra. The Lorentzian width of each of these components was fixed at 215 meV [159]; their Gaussian widths and intensities were allowed to vary within physical limits. Initial positions were chosen to yield components representing the *Ph+F* and *B* components in the bulk (*b*) and at the surface (*s*). However, the separation between bulk and surface pairs is of the order of the experimental resolution. To compensate for this fact, the positions were constrained such that the separation between *Ph+F* and *B* components at the surface matched that in the bulk, to within 10%. Otherwise, the positions were

allowed to vary freely. In order to obtain a good fit to both spectra simultaneously, it was only necessary to allow the intensities and widths of the components to differ between normal and grazing emission: all other parameters were equivalent across both data sets. The parameters for the resulting fits are given in table 7.1.

There is considerable evidence to support the validity of this four-component fit. In moving from normal to grazing emission, surface sensitivity is increased; the fits show more surface character in the grazing emission spectrum. The relative intensities of the *Ph+F* and *B* components in both the bulk and at the surface are in excellent agreement with those expected (94% & 6% respectively, compared to 93% & 7%). The *Ph+F* components are considerably broader than their corresponding *B* components. This is as expected, as the *Ph+F* component contains both sp^2 and sp^x $(2 < x < 3)$ contributions, whilst the *B* component is solely due to sp^3 hybrids. Bulk components are broader than those at the surface, due to the presence of multiple scattering sites within the bulk of the material. Finally, it is worthy of note that the bulk and surface *Ph+F* to *B* separations are identical, despite the 10% tolerance permitted during the fit.

From these fits, it is possible to conclude that the rehybridisation of members of the fullerene cage in bonding to the phenyl groups produces a C 1*s* core-level shift of +1.0 eV. The local-field behaviour due to polarisation screening observed in C_{60} systems [63] is preserved, and its effect enhanced due to fullerene functionalisation and the concomitant differences in molecular packing, in this case producing a shift of +0.2 eV between bulk and surface contributions. Furthermore, the bulk and surface *Ph+F* to *B* area ratios are very similar, and there is very little change in their values between the normal and grazing emission spectra. The lack of any significant change in the *Ph+F*:*B* surface ratio, in particular, indicates that $(C_6H_5)_5C_{60}H$ does not occupy a preferred orientation at the surface of the multilayer. This is wholly consistent with observations from probe microscopy [158].

The VB-PES and NEXAFS spectra of the thick $(C_6H_5)_5C_{60}H$ film are presented in figure 7.3, along with those from a similar thick film of C_{60} and theoretical valence bands for both molecules. The theoretical valence bands were

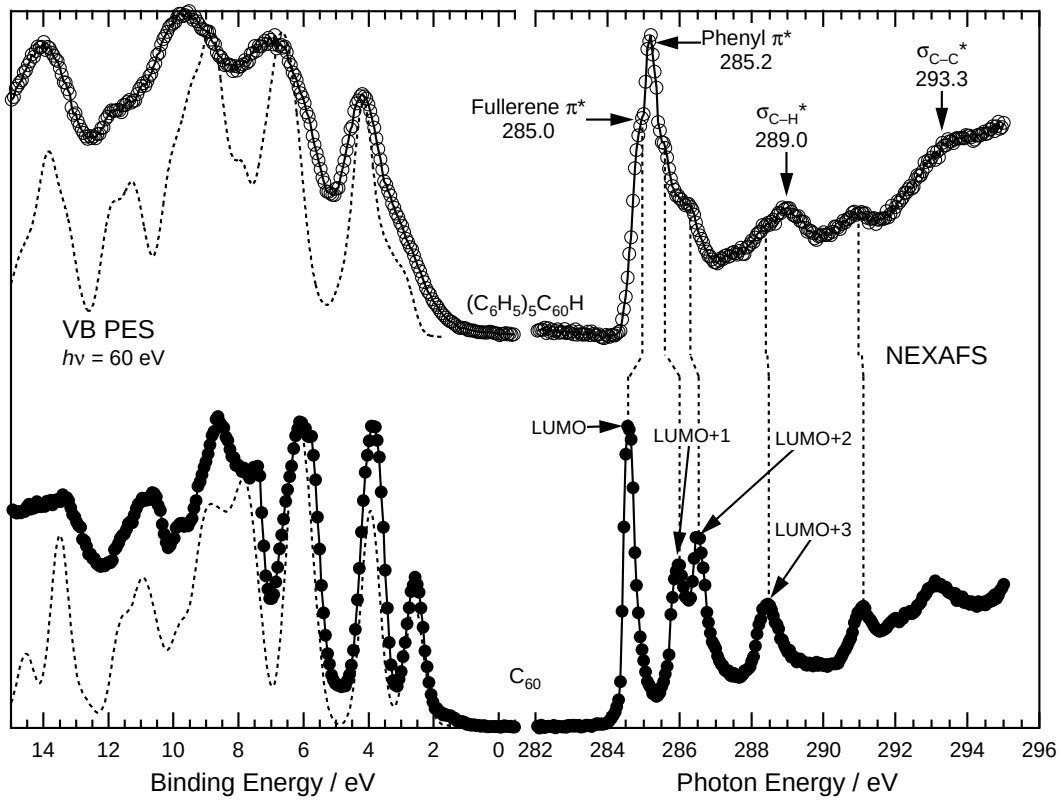

FIGURE 7.3: Valence band photoemission ($h\nu = 60$ eV) and NEXAFS spectra for thick films of C_{60} (filled circles) and $(C_6H_5)_5C_{60}H$ (empty circles), along with valence bands from theory (dashed).

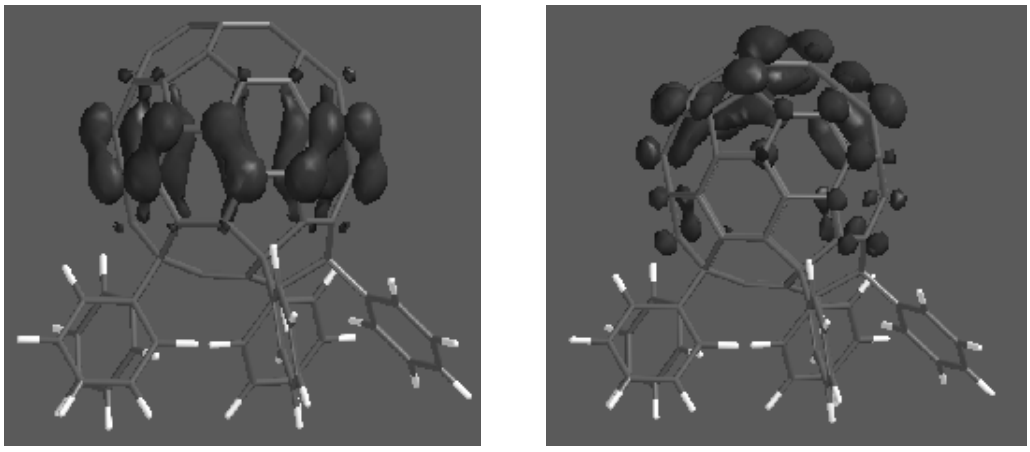

HOMO LUMO

FIGURE 7.4: The HOMO and LUMO of $(C_6H_5)_5C_{60}H$.

produced by convolving orbital energies from B3LYP/6-31G* electronic structure calculations with a Gaussian of width 0.35 eV. There is good agreement between these results and those obtained experimentally. The onset of the density of occupied states (valence band) of both molecules is comparable. The NEXAFS spectra show that the lowest unoccupied states of the fullerene are broadened and shifted due to the addition of the phenyl groups.

Although the onset of the valence band for both molecules is comparable, the NEXAFS measurements show that the edge of the unoccupied state density is shifted by ~ 0.75 eV to higher energy in $(C_6H_5)_5C_{60}H$. As theoretical calculations (see figure 7.4 and reference [156]) indicate that both the HOMO and LUMO are rather localised on the fullerene cage, we identify the shoulder at approximately 285 eV in the $(C_6H_5)_5C_{60}H$ NEXAFS data as arising from the fullerene cage. Following previous work [160–162], the intense peak at 285.2 eV is attributed to the phenyl π^* resonance. A second phenyl-derived resonance is located at 289.0 eV [160–162]. Other resonances are largely fullerene-derived, as indicated in figure 7.3.

Taken together, the valence band, NEXAFS and theoretical data shown in figures 7.3 and 7.4 illustrate that the phenyl groups make little direct contribution to the HOMO and LUMO in $(C_6H_5)_5C_{60}H$. The differences in the HOMO and LUMO spatial distribution for $(C_6H_5)_5C_{60}H$ as compared to the parent fullerene molecule are due to phenyl-induced changes in the on-cage electronic structure. Furthermore — and of particular importance for the adsorption studies described below — it is conceivable that bonding interactions between $(C_6H_5)_5C_{60}H$ and a surface are most likely to be driven by the cage-localised frontier orbitals rather than the phenyl groups.

No variation in the intensity of NEXAFS components was observed as a function of incidence angle. This gives little information concerning orientation or ordering within the multilayer — such a result could be expected in either an ordered or disordered case. A preferred orientation of the fullerene cage may be undetectable using NEXAFS due to its symmetry. If the $(C_6H_5)_5C_{60}H$ film were ordered, the phenyl groups could still occupy a number of different orientations,

by rotating to minimise both inter- and intramolecular phenyl–phenyl repulsions. All that can be concluded is that no interaction exists between molecules in the multilayer that causes alignment of the *phenyl* groups in a preferred orientation. This is, once again, consistent with scanning tunnelling microscopy studies of $(C_6H_5)_5C_{60}H$ films [158].

7.3.2 Adsorption at Si(111)–(7×7)

Si $2p$ core-level spectra for the clean Si(111)–(7×7) surface and 0.7 ML of $(C_6H_5)_5C_{60}H$/Si(111) are shown in figure 7.5, along with curve fits to the normal emission data. Normal and grazing emission C $1s$ spectra for the 0.7 ML coverage, both fitted, are presented in figure 7.6. Parameters for the Si $2p$ and C $1s$ curve fits are given in tables 7.2 and 7.3.

Seven components are present in the fit to Si $2p$ core level for the clean surface — one bulk component, and six due to surface core-level shifts, as detailed in section 3.5.1. The parameters for this fit compare well to those published elsewhere [76, 77].

After deposition of $(C_6H_5)_5C_{60}H$, the rest atom peak (S_3) is completely attenuated. All remaining surface components are broadened. This is to be expected with a sub-monolayer coverage of material, as an unsaturated monolayer results in a variety of chemical environments at the surface. In addition, a small peak, labelled F_2 in figure 7.5(b), appears at an RBE of approximately +1.0 eV. This peak, which is seen in the raw data as a small shoulder on the high binding energy side of the spectrum, arises from Si–C covalent bonds [163]. A second, very broad component is also observed at a RBE of around +2 eV; this component is labelled F_1 in figure 7.5(b). All of these changes are comparable to those observed after the adsorption of C_{60} on Si(111)–(7×7): fullerene related components appear at binding energies of around 1 and 2 eV above the bulk line [103, 164]. This suggests that there is a covalent interaction between the silicon surface and the fullerene region of $(C_6H_5)_5C_{60}H$, consistent with the localisation of the frontier orbitals of the molecule.

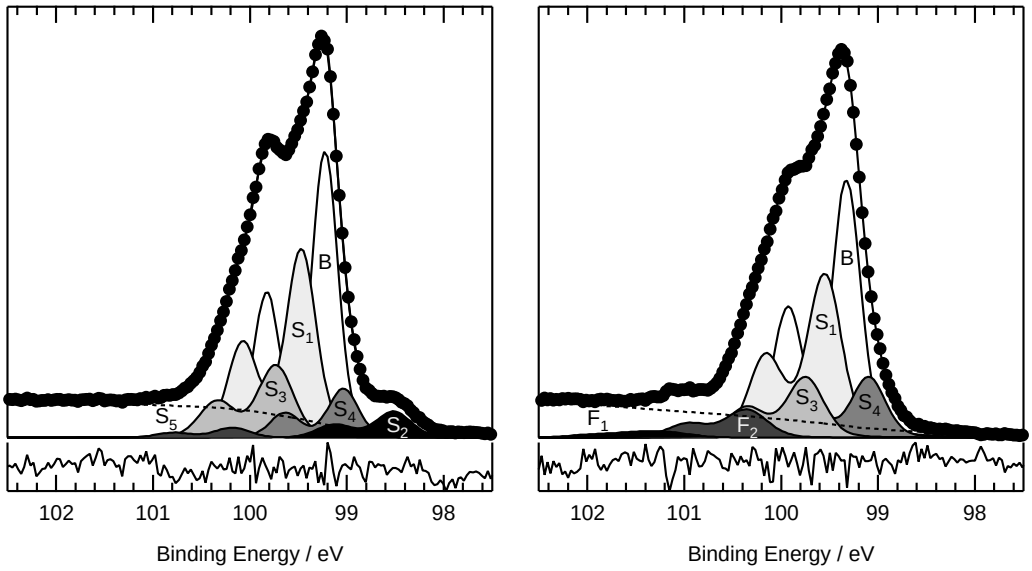

a b

FIGURE 7.5: Normal emission Si $2p$ core-levels of clean Si(111)–(7×7) (a) and 0.7 ML $(C_6H_5)_5C_{60}H$/Si(111)–(7×7) (b), with curve fits. The parameters for the curve fits are given in Table 7.2.

	Clean Si(111)–(7×7)			0.7 ML $(C_6H_5)_5C_{60}H$/Si(111)		
	Energy/eV	Γ_g/eV	Area/%	Energy/eV	Γ_g/eV	Area/%
Bulk	99.22	0.26	41	99.33	0.29	40
S_1	+0.25	0.32	31	+0.23	0.37	30
S_2	-0.71	0.38	5	-	-	-
S_3	+0.51	0.38	13	+0.43	0.40	11
S_4	-0.19	0.32	8	-0.23	0.37	11
S_5	+0.96	0.38	2	-	-	-
F_1	-	-	-	+1.95	0.65	2
F_2	-	-	-	+1.03	0.45	6

Common parameters:

Lorentzian width (Γ_L)	90 meV
Spin-orbit split	595 meV
Branching ratio	2.005

TABLE 7.2: Fitting parameters for Si $2p$ curve fits shown in Figure 7.5.

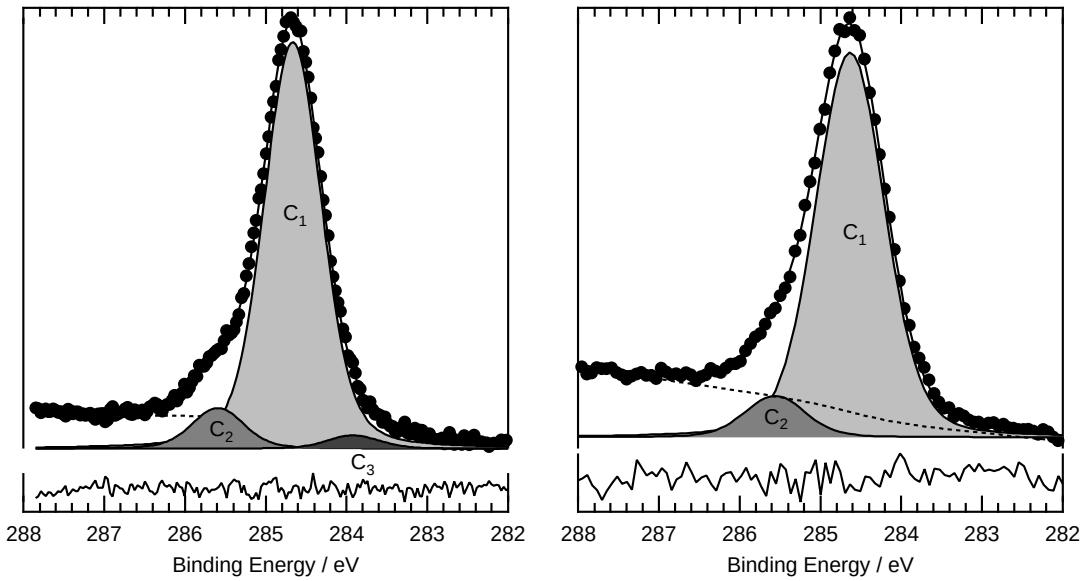

FIGURE 7.6: Normal (a) and grazing emission (b) C 1s core levels for 0.7 ML $(C_6H_5)_5C_{60}H$/Si(111), along with curve fits, the parameters for which are given in Table 7.3.

		NE		+60°	
	Energy	Γ_g	Area	Γ_g	Area
C_1	284.67	0.72	89	0.88	91
C_2	+0.93	0.64	8	0.76	9
C_3	-0.75	0.64	3	-	-

TABLE 7.3: Parameters for the C 1s curve fits shown in Figure 7.6. The Lorentzian width was fixed at 215 meV.

Three components are required to fit the normal emission C 1*s* spectrum. As before, the main peak is attributed to sp^x $(2 < x < 3)$ carbons in the fullerene cage and sp^2 carbons in the phenyl groups. The presence of two similar chemical states within this component account for its increased width, as compared to the other components. The component at +0.93 eV is due to sp^3 carbons involved in bonding between the fullerene cage and the phenyl groups. The shift of the third component (-0.75 eV) is comparable to that observed in the formation of Si-C bonds [165], again suggesting a covalent interaction between $(C_6H_5)_5C_{60}H$ and the substrate. Further evidence to support this assignment is found in the fact that the -0.75 eV component vanishes in the more surface sensitive grazing emission spectrum. There is no significant change in the ratio of the C_1 to C_2 areas. This indicates that $(C_6H_5)_5C_{60}H$ does not adsorb in such a way that all phenyl groups are directed either towards or away from the surface, consistent with investigations employing probe microscopy [158].

7.3.3 Adsorption at Ag:Si(111)–$(\sqrt{3} \times \sqrt{3})$R30°

Figure 7.7 shows the Si 2*p* core-level of the Ag:Si(111)–$(\sqrt{3} \times \sqrt{3})$R30° surface before and after deposition of $\sim$ 0.9ML of $(C_6H_5)_5C_{60}H$. Considering the clean surface spectrum first, we note that the line shape is in very good agreement with previously published Si 2*p* core-level spectra of the Ag:Si(111)–$(\sqrt{3} \times \sqrt{3})$R30° reconstruction [166]. However, compared to the clean Si(111)–(7×7) surface, we observe a somewhat smaller binding energy shift (0.25 eV) of the entire spectrum than reported in previous work. For example, Tong et al. [167] have observed a shift of the Si 2*p* spectrum by approximately 0.5 eV for the Ag:Si(111)–$(\sqrt{3} \times \sqrt{3})$R30° surface as compared to the clean Si(111)–(7×7) surface. It is possible that this discrepancy in absolute binding energy relates to a small amount of excess Ag present on the surface, as a result of the preparation procedure employed [91]. The presence of $\sim$ 0.1 ML of additional Ag yields a binding energy shift of approximately 0.3 eV [167] — much closer to the value observed here. It is worthy of note that, following Hecht [168], for the doping density of

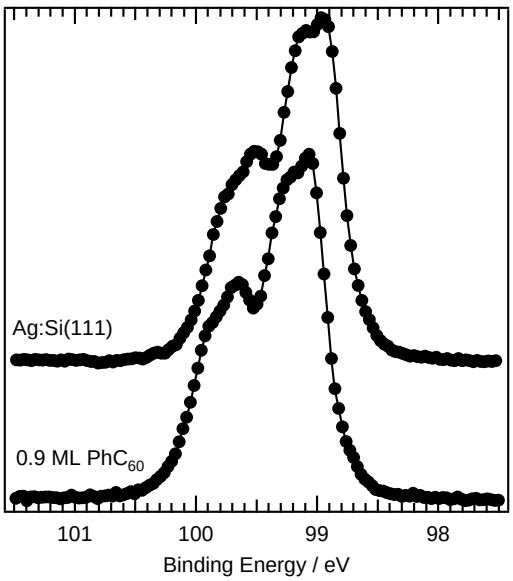

FIGURE 7.7: Si $2p$ core levels of the clean Ag:Si(111) surface and of 0.9 ML $(C_6H_5)_5C_{60}H$/Ag:Si(111).

the substrate used here (10^{16} cm^{-3}) and the photon flux obtained in the experiments, the possibility that this shift arises due to surface photovoltaic effects can be ruled out.

Following adsorption of 0.9 ML of $(C_6H_5)_5C_{60}H$, although there is no significant change in the Si $2p$ line shape (as also previously observed for C_{60} adsorption on Ag:Si(111)–$(\sqrt{3} \times \sqrt{3})$R30° [104]), the core level undergoes a wholesale shift of 0.2 eV to higher binding energy. The lack of change in the Si $2p$ line-shape strongly suggests that the interaction of the $(C_6H_5)_5C_{60}H$ molecule with the underlying Ag-terminated Si(111) surface is extremely weak and lacks the covalent character that is a feature of fullerene adsorption on clean Si(111)–(7×7) surfaces.

The shift of the Si $2p$ peak to higher binding energy is intriguing. No shift of the Si $2p$ spectrum is observed following C_{60} adsorption on the Ag:Si(111)–$(\sqrt{3} \times \sqrt{3})$R30° surface [104]. Hasegawa et al. [169] have proposed that C_{60} acts as an acceptor when adsorbed on the Ag:Si(111)–$(\sqrt{3} \times \sqrt{3})$R30° reconstruction, compensating conduction electrons in the S_1 surface state band [167, 170] of the substrate but, significantly, not promoting additional band bending. This

scenario is consistent with the lack of a Si $2p$ binding energy shift in the data published by LeLay et al. [104]. Adsorption of univalent atoms on the Ag:Si(111)–$(\sqrt{3} \times \sqrt{3})$R30° surface, however, produces Si $2p$ shifts to higher binding energy of order 200 meV. This shift arises from electron transfer into the S_1 band (~ 0.1 electron per adsorbed atom), depleting the hole concentration in the substrate space charge layer [167]. The results shown here suggest that, unlike the parent C_{60} molecule, $(C_6H_5)_5C_{60}H$ acts as an electron donor on the Ag:Si(111)–$(\sqrt{3} \times \sqrt{3})$R30° surface. Coheur et al., in a series of quantum chemical calculations, have shown that each phenyl group donates 0.03 ± 0.02 e^- to the fullerene cage, with the H atom donating 0.22 e^- [171]. The total excess charge on the unmodified (i.e. unfunctionalised) part of the cage was determined to be -0.176 e^-.

Previous STM measurements [158] have shown that $(C_6H_5)_5C_{60}H$ molecules adopt an orientation on the Ag:Si(111)–$(\sqrt{3} \times \sqrt{3})$R30° surface where one phenyl group and a hexagonal face of the cage are in contact with the substrate. That is, the molecule effectively lies on its side rather than adopting a geometry in which the phenyl groups are directed away from the surface or, conversely, where the unmodified part of the cage is separated from the surface by the phenyl groups. It is particularly interesting to note that this 'on-side' geometry will maximise the contact area of the equatorial belt of the molecule with the Ag-terminated Si(111) surface. As the molecular HOMO is localised around the equatorial belt, this provides a natural mechanism for charge transfer from $(C_6H_5)_5C_{60}H$ to the underlying Ag:Si(111)–$(\sqrt{3} \times \sqrt{3})$R30° surface.

7.4 Conclusion

The modification of C_{60} through the addition of phenyl groups causes major alterations to the electronic structure of the fullerene, resulting in significant changes to the chemical behaviour of the system. Interestingly, the presence of the phenyl groups appears to modify the chemical behaviour of the fullerene cage itself, as opposed to the mere introduction of phenyl chemistry to the molecular system. In the frontier region, the phenyl groups make little direct contribution

to the electronic structure — rather, they induce a lifting of the degeneracy in the structure of the fullerene cage.

Good fits to the C 1*s* photoemission data acquired from thick films of $(C_6H_5)_5C_{60}H$ can only be achieved by considering differences in polarisation screening for molecules in surface- and bulk-like environments. There is considerable evidence for a covalent interaction between $(C_6H_5)_5C_{60}H$ and the Si(111)–(7×7) surface, as for C_{60}. The interaction of $(C_6H_5)_5C_{60}H$ with the Ag:Si(111)–$(\sqrt{3} \times \sqrt{3})$R30° surface, on the other hand, is much weaker, and largely van der Waals in character. Nevertheless, a small amount of charge transfer to the substrate apparently plays a role in the adsorption process, in stark contrast to the adsorption of C_{60} at this surface, indicating fundamental changes in the fullerene chemistry upon addition of phenyl groups. This charge transfer interaction is consistent with the molecular orientation observed in previous STM measurements of $(C_6H_5)_5C_{60}H$ (sub)monolayers on the Ag:Si(111)–$(\sqrt{3} \times \sqrt{3})$R30° surface.

7.4.1 Future work

The charge transfer effect at the Ag:Si(111)–$(\sqrt{3} \times \sqrt{3})$R30° surface is particularly interesting. Recent photoemission studies of pentacene adsorption at this surface have observed a similar shift of the Si 2*p* core level peak position to higher binding energy [172]. In order to fully understand the nature of this shift, firstly, the role of excess Ag in the molecular adsorption process needs to be addressed. Secondly, the availability of a variety of modified fullerenes, in useful quantities and of high purity (for example, $(C_6H_5)_5C_{60}OH$, Ce@C_{82} and Tm@C_{82}), provides the opportunity to make a considerable contribution to the literature concerning the effects of adsorption on band bending at the Ag:Si(111)–$(\sqrt{3} \times \sqrt{3})$R30° surface.

CHAPTER 8

Conclusion

8.1 Summary of findings

Considering firstly the theoretical studies, discussed in chapter 4, the density functional EDF1 has been shown to perform well. When used in conjunction with moderate basis sets, it provides an accuracy that is comparable to that of B3LYP, at a reduced computational expense. Furthermore, when the size of the basis set is reduced, the accuracy of EDF1 is not as heavily compromised as that of B3LYP. Cluster models, on the other hand, have been shown to have limited use in modelling the Si(100)–(2×1) surface. This being the case, either plane-wave calculations, or methods involving Gaussian basis sets with periodic boundary conditions, employing a slab model of the surface may be more appropriate to the study of adsorption. However, a QM/MM method, using a large MM-treated cluster with a small adsorption region modelled using *ab initio* theory, may provide an alternative approach, in which EDF1 could act as an efficient QM component.

The theoretical investigations have also predicted a large number of stable binding geometries of C_{60} at the Si(100)–(2×1) surface. However, these results

were obtained using a fairly low level of theory. As such, the absolute binding energies are quite suspect, but the relative stabilities may be reliable. Such a large number of possible binding energies presents a challenge for further investigation at higher levels of theory. When concerned with the electronic structure of C_{60} adsorbed at Si(100)–(2 × 1), it may not be necessary to consider all of these configurations, as indicated by the excellent agreement between the results of a simple C_{60}–Si model with those from experimental investigations.

Alkali-metal doping of C_{60} adsorbed at silicon surfaces is possible, as the interaction strength of K with the adsorbate and the substrate is comparable. However, a difference in the molecular packing at these two surfaces results in the stabilisation of a metallic state on Si(111)–(7 × 7), but not on Si(100)–(2 × 1). There is evidence to suggest that a direct measure of the charge transfer to the fullerene LUMO can be obtained from the ratio of LUMO to HOMO plus HOMO-1 integrated areas. Such measurements have shown that the K_xC_{60} system saturates at $x = 6$, on both the Si(100)–(2 × 1) and Si(111)–(7 × 7) surfaces. The data also suggest that the covalent interaction causes the fullerene LUMO to split

Conversely, there is no significant charge transfer from either Ag or Au to C_{60} adsorbed at the Si(111)–(7 × 7) surface. Ag demonstrates little interaction with either the adsorbed fullerene or the silicon substrate, condensing to form clusters at the surface of the monolayer. Au interacts sufficiently strongly with the silicon substrate to displace adsorbed C_{60}, forming a silicide, the growth of which begins at defects in the C_{60} monolayer, such as step edges and domain boundaries. The results also indicate the presence of metallic gold and complexes of C_{60}–Au–Si and, although their location within the system has not been determined.

The addition of phenyl groups to C_{60} is seen to produce considerable changes in the electronic structure of the fullerene cage, itself. The interaction of $(C_6H_5)_5C_{60}H$ with the Si(111)–(7×7) surface is very similar to that observed for unmodified C_{60} — there is evidence to suggest the formation of covalent bonds with the fullerene cage. At the Ag:Si(111)–$(\sqrt{3} \times \sqrt{3})$R30° surface, $(C_6H_5)_5C_{60}H$ acts as a donor, in stark contrast to the behaviour of C_{60} at this surface, for which no significant

charge transfer is observed. Furthermore, the donor behaviour of $(C_6H_5)_5C_{60}H$ at the Ag:Si(111)–$(\sqrt{3} \times \sqrt{3})$R30° surface and the localisation of the highest occupied molecular orbitals, according to theoretical studies, are consistent with the preferred orientation of the molecule at this surface, as observed using STM.

8.2 Future work

The work presented here has begun to address the role of strong interactions with a reactive substrate, in particular covalent interactions with technologically important silicon surfaces, in determining the properties of thin films of modified fullerenes. As noted previously, further work is required to determine the nature of multi-special complexes formed in $Ag/C_{60}/Si$ systems. Additionally, the possibility of surfactant-mediated growth in C_{60}–Au–Si systems is worthy of attention, as the behaviour of fullerenes in this manner has not been observed in other systems.

Further work is also required to fully understand band bending and the behaviour of $(C_6H_5)_5C_{60}H$ as a dopant at the Ag:Si(111)–$(\sqrt{3} \times \sqrt{3})$R30° surface. Other functionalised fullerenes can be synthesised and purified; in reference to work presented here, a study of $(C_6H_5)_5C_{60}OH$ at Ag:Si(111)–$(\sqrt{3} \times \sqrt{3})$R30° may be particularly worthwhile. This molecule is similar to $(C_6H_5)_5C_{60}H$, studied here, but it may be expected that the presence of the highly electronegative oxygen could inhibit the donor behaviour observed in $(C_6H_5)_5C_{60}H$/Ag:Si(111)–$(\sqrt{3} \times \sqrt{3})$R30°. Since charge is transferred *to* the fullerene cage from the phenyl groups, the effects of the oxygen on the electronic structure of this molecule may also be particularly interesting, in their own right.

The work concerning potassium-doped monolayers has revealed considerable information regarding changes in the structure of the C_{60} LUMO, as a result of a strong interaction with the substrate. A similar approach could be employed to investigate changes resulting from different types of adsorbate-substrate interaction, such as that observed for C_{60}/Ag(100) [173].

Finally, there is still much to address concerning the effects of a reactive sub-

strate on endohedral fullerenes, which have not been considered here. The high level of delocalisation across fullerene cages can yield very effective electronic screening. Studies of the electronic structure of the enclosed species in an endohedral system may provide insights into the nature of this screening, and how it is affected by adsorbate–substrate interactions.

APPENDIX A

Additional work

A.1 Colloidal particle foams

AFM and PES has been used to study the structures formed by colloidal particles when spin-coated onto silicon-oxide surfaces. The colloidal particles were Au nanoclusters, coated with various alkanethiols. The particles were observed to form a variety of patterns at the surface, including two-dimensional cellular networks. The behaviour of these structures under annealing was particularly interesting. Annealing at temperatures in the region of 200°C to 300°C results in breaking of the Au–thiolate bonds and desorption of the passivating organic chains. However, the cellular network formed by the Au clusters remains intact. At higher temperatures, there is also significant sintering of the clusters. This work was published in *Applied Physics Letters* [174].

A.2 Hydrogen-bonded molecular networks

A series of semi-empirical, Hartree-Fock and DFT calculations was carried out to study the structures and interaction of perylene tetracarboxylic di-imide (PTCDI)

and melamine when confined to planar geometries, after STM images revealed that these molecules formed a hexagonal supramolecular network on the Ag:Si(111)–$(\sqrt{3} \times \sqrt{3})$R30° surface. The calculations revealed that the hexagonal structure could not, as first thought, be formed from PTCDI alone, but in fact arises due to hydrogen bonding between PTCDI and melamine, with the latter at the vertexes of the hexagonal cells. The theoretical intermolecular separation of hydrogen-bonded PTCDI and melamine, when confined to a planar gemeotry, was found to be near-commensurate with the HCT structure of the Ag:Si(111)–$(\sqrt{3}\times\sqrt{3})$R30° surface. Investigation of the interaction strength as a function of intermolecular separation revealed that the hexagonal network can become fully commensurate with the HCT structure, via the relaxation of bond lengths, with a very low energetic cost. This research contributed to a publication in *Nature* [175].

A.3 Novel GaAs quantum dots

AFM was used to study the structure of quantum dots grown using a specialist molecular-beam epitaxy (MBE) technique developed at the University of Nottingham. Novel structures were observed, including pyramidal quantum dots and elliptical rings. The latter may be of particular use in the experimental study of excited modes in quantum dots. The AFM studies revealed that the growth technique did not yield uniform growth across the surface. The spatial variation in the population density of the two different structures was evaluated. It is hoped that the results of this study, in conjunction with considerations of growth processes and the geometry of the MBE system, may be useful in refinement of the growth technique.

List of figures

Nomenclature

Symbols

$\mathbf{C}$; C_{mi}	expansion coefficient matrix; matrix element
$\mathbf{D}$	density matrix
E_B	binding energy
E_{LJ}	The Lennard-Jones potential
$\hat{f}_i$	Fock operator
$\mathbf{F}$; F_{mn}	Fock matrix; matrix element
$\hat{g}$	electron–electron repulsion operator
$\mathbf{G}$	matrix of two-electron integrals
$\hat{H}$	Hamiltonian operator
h	Planck constant
$\mathbf{h}_{\mathrm{KS}}$	Kohn-Sham operator
J_{ij}; $\hat{J}_i$	Coulomb integral; operator form
K_{ij}; $\hat{K}_i$	exchange integral; operator form
l	orbital angular-momentum quantum number
R_0	van der Waals atomic radius

s	spin angular-momentum quantum number
$\mathbf{S}$; S_{mn}	overlap matrix; matrix element
$\hat{T}$	kinetic energy operator
$\hat{V}$	potential energy operator
α, β	orthonormal functions used to represent spin
Γ_G	Gaussian width
Γ_L	Lorentzian width
ν	frequency
σ_c	photoelectron capture cross-section
ϕ_i	Kohn-Sham orbital
Φ_{SD}	many-electron Slater-determinant wavefunction
χ_i	one-electron spin-orbital; molecular orbital
Ψ	time independent wavefunction

Abbreviations

AFM	atomic force microscopy
AO	atomic orbitals
B3	Becke three-parameter exchange functional
DAS	dimer adatom stacking-fault
DFT	density functional theory
DOS	density of states
EDC	energy distribution curve; a photoelectron spectrum
EDF1	empirical density functional 1
GGA	generalised gradient approximation
HF	Hartree-Fock
HOMO	highest occupied molecular orbital
HOMO$-N$	$(N+1)^{st/nd/rd/th}$ highest occupied molecular orbital

LCAO	linear combination of atomic orbitals
LDA	local density approximation
LSDA	local spin density approximation
LUMO	lowest unoccupied molecular orbital
LUMO$-N$	($N + 1^{st/nd/rd/th}$ lowest unoccupied molecular orbital
LYP	Lee, Yang and Parr correlation functional
MBE	molecular-beam epitaxy
MFP	mean free path
MM	molecular mechanics
MO	molecular orbital
NEXAFS	near edge X-ray absorption fine structure
PES	photoemission spectroscopy
PTCDI	perylene tetracarboxylic di-imide
PYD	partial yield detector
QM/MM	quantum mechanical / molecular mechanical
RBE	relative binding energy
RHF	restricted Hartree-Fock
ROHF	restricted open-shell Hartree-Fock
SCF	self consistent field
SCLS	surface core-level shifts
SD	Slater determinant
STO	Slater-type orbital
TEY	total electron yield (detector)
TF	Thomas Fermi
TFD	Thomas Fermi Dirac
UHF	unrestricted Hartree-Fock
UHV	ultra-high vacuum

UPS	ultraviolet photoemission spectroscopy
XANES	X-ray absorption near edge structure (*syn.* NEXAFS)
XC	exchange-correlation
XPS	X-ray photoemission spectroscopy

References

[1] H. W. Kroto, J. R. Heath, S. C. Obrien, R. F. Curl, and R. E. Smalley. *Nature*, **318**, 6042, 162–163, (1985).

[2] E. Osawa. *Kagaku*, **25**, 854–863, (1970).

[3] W. Krätschmer, L. D. Lamb, K. Fostiropoulos, and D. R. Huffmann. *Nature*, **347**, 354, (1990).

[4] T. L. Makarova, B. Sundqvist, R. Hohne, P. Esquinazi, Y. Kopelevich, P. Scharff, V. A. Davydov, L. S. Kashevarova, and A. V. Rakhmanina. *Nature*, **413**, 6857, 716–718, (2001).

[5] J. Pascual, J. Gomez-Herrero, C. Rogero, A. Baro, D. Sanchez-Portal, E. Artacho, P. Ordejon, and J. Soler. *Chem. Phys. Lett.*, **321**, 1-2, 78–82, (2000).

[6] M. J. Butcher, J. W. Nolan, M. R. C. Hunt, P. H. Beton, L. Dunsch, P. Kuran, P. Georgi, and T. J. S. Dennis. *Phys. Rev. B*, **67**, 12, art. no.–125413, (2003).

[7] D. L. Keeling, M. J. Humphry, P. Moriarty, and P. H. Beton. *Chem. Phys. Lett.*, **366**, 3-4, 300–304, (2002).

[8] M. J. Butcher, F. H. Jones, P. Moriarty, P. H. Beton, K. Prassides, K. Kordatos, and N. Tagmatarchis. *Appl. Phys. Lett.*, **75**, 8, 1074–1076, (1999).

[9] P. Moriarty, Y. R. Ma, M. D. Upward, and P. H. Beton. *Surf. Sci.*, **407**, 1-3, 27–35, (1998).

[10] J. Gimzewski, T. Jung, M. Cuberes, and R. Schlittler. *Surf. Sci.*, **386**, 1-3, 101–114, (1997).

[11] H. Tang, M. T. Cuberes, C. Joachim, and J. K. Gimzewski. *Surf. Sci.*, **386**, 1-3, 115–123, (1997).

[12] P. Moriarty, A. W. Dunn, Y. R. Ma, M. D. Upward, and P. H. Beton. *Fullerene Sci. Technol.*, **5**, 4, 769–780, (1997).

[13] M. T. Cuberes, R. R. Schlittler, and J. K. Gimzewski. *Appl. Phys. Lett.*, **69**, 20, 3016–3018, (1996).

[14] P. H. Beton, A. W. Dunn, and P. Moriarty. *Surf. Sci.*, **362**, 1-3, 878–881, (1996).

[15] P. H. Beton, A. W. Dunn, and P. Moriarty. *Appl. Phys. Lett.*, **67**, 8, 1075–1077, (1995).

[16] R. Yamachika, M. Grobis, A. Wachowiak, and M. F. Crommie. *Science*, **304**, 5668, 281–284, (2004).

[17] P. J. Benning, D. M. Poirier, T. R. Ohno, Y. Chen, M. B. Jost, F. Stepniak, G. H. Kroll, J. H. Weaver, J. Fure, and R. E. Smalley. *Phys. Rev. B*, **45**, 12, 6899–6913, (1992).

[18] D. Bethune, R. Johnson, J. Salem, M. Devries, and C. Yannoni. *Nature*, **366**, 6451, 123–128, (1993).

[19] R. D. Johnson, M. S. Devries, J. Salem, D. S. Bethune, and C. S. Yannoni. *Nature*, **355**, 6357, 239–240, (1992).

[20] Y. Chai, T. Guo, C. Jin, R. Haufler, L. Chibante, J. Fure, L. Wang, J. Alford, and R. Smalley. *J. Phys. Chem.*, **95**, 20, 7564–7568, (1991).

[21] J. C. Hummelen, B. Knight, J. Pavlovich, R. Gonzalez, and F. Wudl. *Science*, **269**, 5230, 1554–1556, (1995).

[22] F. Jensen. *Introduction to Computational Chemistry.* Wiley, 1999.

[23] W. J. Hehre, L. Radom, J. A. Pople, and P. V. R. Schleyer. *Ab Initio Molecular Orbital Theory.* Wiley, 1986.

[24] J. E. Lennard-Jones. *Proc. Roy. Soc. London Ser. A*, **106**, 463, (1924).

[25] T. L. Hill. *J. Chem. Phys.*, **16**, 399–404, (1948).

[26] T. Koopmans. *Physica*, **1**, 104–113, (1933).

[27] C. C. J. Roothaan. *Rev. Mod. Phys.*, **23**, 69–89, (1951).

[28] G. G. Hall. *Proc. Roy. Soc. London Ser. A*, **205**, 541–542, (1951).

[29] R. G. Parr and W. Yang. *Density Functional Theory of Atoms and Molecules.* Oxford University Press, 1989.

[30] P. Hohenberg and W. Kohn. *Phys. Rev. B*, **136**, B864–B871, (1964).

[31] S. H. Vosko, L. Wilk, and M. Nusair. *Can. J. Phys.*, **58**, 8, 1200–1211, (1980).

[32] J. P. Perdew. *Phys. Rev. B*, **33**, 12, 8822–8824, (1986).

[33] A. D. Becke. *Phys. Rev. A*, **38**, 6, 3098–3100, (1988).

[34] D. P. Chong, O. V. Gritsenko, and E. J. Baerends. *J. Chem. Phys.*, **116**, 1760–1772, (2002).

[35] O. V. Gritsenko and B. E. J. *J. Chem. Phys.*, **120**, 18, 8364–8372, (2004).

[36] K. Neymeyr and F. Seelig. *Int. J. Quantum Chem.*, **53**, 5, 519–535, (1995).

[37] K. Neymeyr and K. Engel. *Int. J. Quantum Chem.*, **53**, 5, 537–540, (1995).

[38] K. Neymeyr. *Int. J. Quantum Chem.*, **53**, 5, 541–552, (1995).

[39] K. Neymeyr. *Int. J. Quantum Chem.*, **53**, 5, 553–568, (1995).

[40] T. A. Halgren. *J. Comput. Chem.*, **17**, 5-6, 490–519, (1996).

[41] T. A. Halgren. *J. Comput. Chem.*, **17**, 5-6, 520–552, (1996).

[42] T. A. Halgren. *J. Comput. Chem.*, **17**, 5-6, 553–586, (1996).

[43] T. A. Halgren and R. B. Nachbar. *J. Comput. Chem.*, **17**, 5-6, 587–615, (1996).

[44] T. A. Halgren. *J. Comput. Chem.*, **17**, 5-6, 616–641, (1996).

[45] T. A. Halgren and B. L. Bush. *Abstr. Pap. Am. Chem. Soc.*, **212**, 2–COMP, (1996).

[46] K. M. Dieter and J. J. P. Stewart. *ACS Symp. Ser.*, **430**, 31–41, (1990).

[47] M. J. S. Dewar, E. G. Zoebisch, E. F. Healy, and J. J. P. Stewart. *J. Am. Chem. Soc.*, **115**, 12, 5348–5348, (1993).

[48] M. J. S. Dewar, E. G. Zoebisch, E. F. Healy, and J. J. P. Stewart. *J. Am. Chem. Soc.*, **107**, 13, 3902–3909, (1985).

[49] J. J. P. Stewart. *J. Comput. Chem.*, **10**, 2, 209–220, (1989).

[50] J. J. P. Stewart. *J. Comput. Chem.*, **10**, 2, 221–264, (1989).

[51] J. J. P. Stewart. *J. Comput. Chem.*, **12**, 3, 320–341, (1991).

[52] W. R. Wadt and P. J. Hay. *J. Chem. Phys.*, **82**, 1, 284–298, (1985).

[53] P. J. Hay and W. R. Wadt. *J. Chem. Phys.*, **82**, 1, 299–310, (1985).

[54] J. Kong, C. A. White, A. I. Krylov, D. Sherrill, R. D. Adamson, T. R. Furlani, M. S. Lee, A. M. Lee, S. R. Gwaltney, T. R. Adams, C. Ochsenfeld, A. T. B. Gilbert, G. S. Kedziora, V. A. Rassolov, D. R. Maurice, N. Nair, Y. H. Shao, N. A. Besley, P. E. Maslen, J. P. Dombroski, H. Daschel, W. M. Zhang, P. P. Korambath, J. Baker, E. F. C. Byrd, T. Van Voorhis, M. Oumi, S. Hirata, C. P. Hsu, N. Ishikawa, J. Florian, A. Warshel, B. G. Johnson, P. M. W. Gill, M. Head-Gordon, and J. A. Pople. *J. Comput. Chem.*, **21**, 16, 1532–1548, (2000).

[55] A. D. Becke. *J. Chem. Phys.*, **98**, 2, 1372–1377, (1993).

[56] C. T. Lee, W. T. Yang, and R. G. Parr. *Phys. Rev. B*, **37**, 2, 785–789, (1988).

[57] R. D. Adamson, P. M. W. Gill, and J. A. Pople. *Chem. Phys. Lett.*, **284**, 1-2, 6–11, (1998).

[58] L. A. Curtiss, K. Raghavachari, G. W. Trucks, and J. A. Pople. *J. Chem. Phys.*, **94**, 11, 7221–7230, (1991).

[59] N. X. Nair, private communications.

[60] H. Hertz. *Ann. Physik (Leipzig)*, **31**, 983, (1887).

[61] A. Einstein. *Ann. Physik*, **17**, 132–148, (1905).

[62] A. Hedgran, K. Siegbahn, and N. Svartholm. *Proc. Phys. Soc.*, **A63**, 960, (1950).

[63] E. Rotenberg, C. Enkvist, P. A. Bruhwiler, A. J. Maxwell, and N. Martensson. *Phys. Rev. B*, **54**, 8, R5279–R5282, (1996).

[64] P. J. Benning, D. M. Poirier, N. Troullier, J. L. Martins, J. H. Weaver, R. E. Haufler, L. P. F. Chibante, and R. E. Smalley. *Phys. Rev. B*, **44**, 4, 1962–1965, (1991).

[65] M. R. C. Hunt, T. Pichler, L. Siller, P. A. Bruhwiler, M. S. Golden, N. Tagmatarchis, K. Prassides, and P. Rudolf. *Phys. Rev. B*, **66**, 19, art. no.–193404, (2002).

[66] A. Proctor and P. M. A. Sherwood. *Analytical Chem.*, **54**, 13–19, (1982).

[67] J. Stöhr. *NEXAFS spectroscopy*. Springer, 1996.

[68] J. Stöhr. *NEXAFS spectroscopy*, chapter 4.2.5. Springer, 1996.

[69] V. R. Dhanak, A. W. Robinson, G. Vanderlaan, and G. Thornton. *Rev. Sci. Instrum.*, **63**, 1, 1342–1345, (1992).

[70] C. S. Mythen, G. Vanderlaan, and H. A. Padmore. *Rev. Sci. Instrum.*, **63**, 1, 1313–1316, (1992).

[71] M. D. Roper, G. van der Laan, H. A. Durr, E. Dudzik, S. P. Collins, M. C. Miller, and S. P. Thompson. *Nucl. Instrum. Methods Phys. Res. A*, **467**, 1101–1104, (2001).

[72] PSP Vacuum Technology. http://www.pspvacuum.com/.

[73] M. Bowler, J. West, F. Quinn, D. Holland, B. Fell, P. Hatherly, I. Humphrey, W. Flavell, and B. Hamilton. *Surf. Rev. Lett.*, **9**, 1, 577–581, (2002).

[74] K. Takayanagi, Y. Tanishiro, S. Takahashi, and M. Takahashi. *Surf.Sci.*, **164**, 367–392, (1985).

[75] G. LeLay, V. Y. Aristov, and M. Fontaine. *J. Phys. IV*, **4**, C9, 213–216, (1994).

[76] G. LeLay, M. Gothelid, T. M. Grehk, M. Bjorkquist, U. O. Karlsson, and V. Y. Aristov. *Phys. Rev. B*, **50**, 19, 14277–14282, (1994).

[77] C. J. Karlsson, E. Landemark, Y. C. Chao, and R. I. G. Uhrberg. *Phys. Rev. B*, **50**, 8, 5767–5770, (1994).

[78] R. J. Hamers, R. M. Tromp, and J. E. Demuth. *Surf. Sci.*, **181**, 1-2, 346–355, (1987).

[79] G. LeLay. *Mater. Chem. Phys.*, **40**, 3, 212–218, (1995).

[80] E. Landemark, C. J. Karlsson, Y. C. Chao, and R. I. G. Uhrberg. *Surf. Sci.*, **287**, 529–533, (1993).

[81] O. Paz, A. J. R. da Silva, J. J. Saenz, and E. Artacho. *Surf. Sci.*, **482**, 458–463, (2001).

[82] M. S. Gordon, J. R. Shoemaker, and L. W. Burggraf. *J. Chem. Phys.*, **113**, 20, 9355–9356, (2000).

[83] J. S. Hess and D. J. Doren. *J. Chem. Phys.*, **113**, 20, 9353–9354, (2000).

[84] J. Shoemaker, L. W. Burggraf, and M. S. Gordon. *J. Chem. Phys.*, **112**, 6, 2994–3005, (2000).

[85] E. Penev, P. Kratzer, and M. Scheffler. *J. Chem. Phys.*, **110**, 8, 3986–3994, (1999).

[86] C. Yang, S. Y. Lee, and H. C. Kang. *J. Chem. Phys.*, **107**, 8, 3295–3299, (1997).

[87] C. Yang and H. C. Kang. *J. Chem. Phys.*, **110**, 22, 11029–11037, (1999).

[88] P. C. Weakliem, G. W. Smith, and E. Carter. *Surf. Sci.*, **232**, 3, L219–L223, (1990).

[89] Y. Kondo, T. Amakusa, M. Iwatsuki, and H. Tokumoto. *Surf. Sci.*, **453**, 1-3, L318–L322, (2000).

[90] T. Takahashi, S. Nakatani, N. Okamoto, T. Ichikawa, and S. Kikuta. *Surf. Sci.*, **242**, 54–58, (1991).

[91] R. I. G. Uhrberg, H. M. Zhang, T. Balasubramanian, E. Landemark, and H. W. Yeom. *Phys. Rev. B*, **65**, 8, art. no.–081305, (2002).

[92] D. Kondo, K. Sakamoto, H. Takeda, F. Matsui, K. Amemiya, T. Ohta, W. Uchida, and A. Kasuya. *Surf. Sci.*, **514**, 1-3, 337–342, (2002).

[93] M. de Seta, D. Sanvitto, and F. Evangelisti. *Phys. Rev. B*, **59**, 15, 9878–9881, (1999).

[94] D. Kondo, K. Sakamoto, Y. Ushimi, M. Harada, A. Kimura, A. Kakizaki, and S. Suto. *Jpn. J. Appl. Phys. Part 1 - Regul. Pap. Short Notes Rev. Pap.*, **38**, 328–331, (1999).

[95] S. Suto, K. Sakamoto, D. Kondo, T. Wakita, A. Kimura, and A. Kakizaki. *Surf. Sci.*, **428**, 85–90, (1999).

[96] K. Sakamoto, D. Kondo, M. Harada, A. Kimura, A. Kakizaki, and S. Suto. *Surf. Sci.*, **435**, 642–646, (1999).

[97] K. Sakamoto, D. Kondo, Y. Ushimi, M. Harada, A. Kimura, A. Kakizaki, and S. Suto. *J. Electron Spectrosc. Relat. Phenom.*, **103**, 413–418, (1999).

[98] K. Sakamoto, D. Kondo, Y. Ushimi, M. Harada, A. Kimura, A. Kakizaki, and S. Suto. *Phys. Rev. B*, **60**, 4, 2579–2591, (1999).

[99] K. Sakamoto, D. Kondo, Y. Ushimi, A. Kimura, A. Kakizaki, and S. Suto. *Surf. Sci.*, **438**, 1-3, 248–253, (1999).

[100] S. Suto, K. Sakamoto, T. Wakita, M. Harada, and A. Kasuya. *Surf. Sci.*, **404**, 1-3, 523–528, (1998).

[101] D. Chen and D. Sarid. *Surf. Sci.*, **329**, 3, 206–218, (1995).

[102] A. V. Hamza and M. Balooch. *Chem. Phys. Lett.*, **201**, 5-6, 404–408, (1993).

[103] P. Moriarty, M. D. Upward, A. W. Dunn, Y. R. Ma, P. H. Beton, and D. Teehan. *Phys. Rev. B*, **57**, 1, 362–369, (1998).

[104] G. LeLay, M. Gothelid, V. Y. Aristov, A. Cricenti, M. C. Hakansson, C. Giammichele, P. Perfetti, J. Avila, and M. C. Asensio. *Surf. Sci.*, **377**, 1-3, 1061–1065, (1997).

[105] M. D. Upward, P. Moriarty, and P. H. Beton. *Phys. Rev. B*, **56**, 4, R1704–R1707, (1997).

[106] Y. Wada. *Electrochemistry*, **71**, 11, 947–952, (2003).

[107] Y. Wada. *Ann.NY Acad.Sci.*, **960**, 39–61, (2002).

[108] H. W. C. Postma, M. de Jonge, Z. Yao, and C. Dekker. *Phys. Rev. B*, **62**, 16, 10653–10656, (2000).

[109] C. Joachim, J. K. Gimzewski, and A. Aviram. *Nature*, **408**, 6812, 541–548, (2000).

[110] H. W. C. Postma, A. Sellmeijer, and C. Dekker. *Adv. Mater.*, **12**, 17, 1299–+, (2000).

[111] P. Avouris, T. Hertel, R. Martel, T. Schmidt, H. R. Shea, and R. E. Walkup. *Appl. Surf. Sci.*, **141**, 3-4, 201–209, (1999).

[112] W. A. Hofer, A. J. Fisher, G. P. Lopinski, and R. A. Wolkow. *Phys. Rev. B*, **6308**, 8, art. no.–085314, (2001).

[113] W. A. Hofer, A. J. Fisher, G. P. Lopinski, and R. A. Wolkow. *Surf. Sci.*, **482**, 1181–1185, (2001).

[114] R. Konečný and D. J. Doren. *Surf. Sci.*, **417**, 2-3, 169–188, (1998).

[115] W. Pan, T. H. Zhu, and W. T. Yang. *J. Chem. Phys.*, **107**, 10, 3981–3985, (1997).

[116] L. Clemen, R. M. Wallace, P. A. Taylor, M. J. Dresser, W. J. Choyke, W. H. Weinberg, and J. T. Yates. *Surf. Sci.*, **268**, 1-3, 205–216, (1992).

[117] P. A. Taylor, R. M. Wallace, C. C. Cheng, W. H. Weinberg, M. J. Dresser, W. J. Choyke, and J. T. Yates. *J. Am. Chem. Soc.*, **114**, 17, 6754–6760, (1992).

[118] J. H. Cho, L. Kleinman, C. T. Chan, and K. S. Kim. *Phys. Rev. B*, **6307**, 7, art. no.–073306, (2001).

[119] R. A. Wolkow, G. P. Lopinski, and D. J. Moffatt. *Surf. Sci.*, **416**, 3, L1107–L1113, (1998).

[120] Y. Taguchi, M. Fujisawa, T. Takaoka, T. Okada, and M. Nishijima. *J. Chem. Phys.*, **95**, 6870–6876, (1991).

[121] M. Niwano, M. Terashi, and J. Kuge. *Surf. Sci.*, **420**, 1, 6–16, (1999).

[122] C. H. Choi, D.-J. Liu, J. W. Evans, and M. S. Gordon. **124**, 8730–8740, (2002).

[123] Y. Jung, C. H. Choi, and M. S. Gordon. **105**, 4039–4044, (2001).

[124] P. D. Godwin, S. D. Kenny, and R. Smith. *Surf. Sci.*, **529**, 237–246, (2003).

[125] A. W. Dunn, B. N. Cotier, A. Nogaret, P. Moriarty, P. H. Beton, and S. P. Beaumont. *Appl. Phys, Lett.*, **71**, 20, 2937–2939, (1997).

[126] M. Merkel, M. Knupfer, M. S. Golden, J. Fink, R. Seemann, and R. L. Johnson. *Phys. Rev. B*, **47**, 17, 11470–11478, (1993).

[127] P. Moriarty. *Rep. Prog. Phys.*, **64**, 3, 297–381, (2001).

[128] S. Margadonna and K. Prassides. *J. Solid State Chem.*, **168**, 2, 639–652, (2002).

[129] K. Sakamoto, T. Wakita, D. Kondo, A. Harasawa, T. Kinoshita, W. Uchida, and A. Kasuya. *Surf. Sci.*, **499**, 1, 63–72, (2002).

[130] T. W. Pi, L. H. Hong, R. T. Wu, C. P. Cheng, and M. H. Ko. *Surf. Rev. Lett.*, **5**, 1, 101–104, (1998).

[131] J. E. Fischer, G. Bendele, R. Dinnebier, P. W. Stephens, C. L. Lin, N. Bykovetz, and Q. Zhu. *J. Phys. Chem. Solids*, **56**, 10, 1445–1457, (1995).

[132] T. Pichler, M. Matus, J. Kurti, and H. Kuzmany. *Phys. Rev. B*, **45**, 23, 13841–13844, (1992).

[133] D. M. Poirier, T. R. Ohno, G. H. Kroll, Y. Chen, P. J. Benning, J. H. Weaver, L. P. F. Chibante, and R. E. Smalley. *Science*, **253**, 5020, 646–648, (1991).

[134] B. W. Hoogenboom, R. Hesper, L. H. Tjeng, and G. A. Sawatzky. *Phys. Rev. B*, **57**, 19, 11939–11942, (1998).

[135] F. H. Jones, M. J. Butcher, B. N. Cotier, P. Moriarty, P. H. Beton, V. R. Dhanak, K. Prassides, K. Kordatos, N. Tagmatarchis, and F. Wudl. *Phys. Rev. B*, **59**, 15, 9834–9837, (1999).

[136] L. Q. Jiang and B. E. Koel. *Phys. Rev. Lett.*, **72**, 1, 140–143, (Jan 1994).

[137] D. Chen and D. Sarid. *Surf. Sci.*, **318**, 1-2, 74–82, (1994).

[138] D. Chen, J. Chen, and D. Sarid. *Phys. Rev. B*, **50**, 15, 10905–10909, (October 1994).

[139] T. Hashizume, X. D. Wang, Y. Nishina, H. Shinohara, Y. Saito, Y. Kuk, and T. Sakurai. *Jap. J. Appl. Phys.*, **31**, 7A, L880–L883, (July 1992).

[140] G. K. Wertheim, G. N. E. Buchanan, and J. E. Rowe. *Chem. Phys. Lett.*, **202**, 320, (1993).

[141] C. Gu, F. Stepniak, D. M. Poirier, M. B. Jost, P. J. Benning, Y. Chen, T. R. Ohno, J. L. Martins, J. H. Weaver, J. Furer, and R. E. Smalley. *Phys. Rev. B*, **45**, 6348, (1992).

[142] G. K. Wertheim and D. N. E. Buchanan. *Phys. Rev. B*, **50**, 15, 11070–11073, (1994).

[143] L. G. Petersson and S. E. Karlsson. *Phys. Scr.*, **16**, 5-6, 425–431, (1977).

[144] M. D. R. Taylor, P. Moriarty, B. N. Cotier, M. J. Butcher, P. H. Beton, and V. R. Dhanak. *Appl. Phys. Lett.*, **77**, 8, 1144–1146, (2000).

[145] A. Goldoni and G. Paolucci. *Surf. Sci.*, **437**, 3, 353–361, (1999).

[146] L. H. Tjeng, R. Hesper, A. C. L. Heessels, A. Heeres, H. T. Jonkman, and G. A. Sawatzky. *Solid State Comm.*, **103**, 1, 31–35, (1997).

[147] D. W. Owens, C. M. Aldao, D. M. Poirier, and J. H. Weaver. *Phys. Rev. B*, **51**, 23, 17068–17072, (1995).

[148] J. J. Yeh, J. Hwang, K. Bertness, D. J. Friedman, R. Cao, and I. Lindau. *Phys. Rev. Lett.*, **70**, 24, 3768–3771, (1993).

[149] A. Franciosi, D. W. Niles, G. Margaritondo, C. Quaresima, M. Capozi, and P. Perfetti. *Phys. Rev. B*, **32**, 10, 6917–6919, (1985).

[150] A. Franciosi, D. G. O'Neill, and Weaver. *J. Vac. Sci. Tech. B*, **1**, 3, 524–529, (1983).

[151] M. del Giudice, J. J. Joyce, and J. Weaver. *Phys. Rev. B*, **36**, 9, 4761–4768, (1987).

[152] A. W. Dunn, P. Moriarty, M. D. Upward, and P. H. Beton. *Appl. Phys. Lett.*, **69**, 4, 506–508, (1996).

[153] C. T. Tzeng, W. S. Lo, J. Y. Yuh, R. Y. Chu, and K. D. Tsuei. *Phys. Rev. B*, **61**, 3, 2263–2272, (2000).

[154] D. Purdie, H. Bernhoff, and B. Reihl. *Surf. Sci.*, **364**, 3, 279–286, (1996).

[155] A. J. Maxwell, P. A. Bruhwiler, A. Nilsson, N. Martensson, and P. Rudolf. *Phys. Rev. B*, **49**, 15, 10717–10725, (1994).

[156] A. G. Avent, P. R. Birkett, J. D. Crane, A. D. Darwish, G. J. Langley, H. W. Kroto, R. Taylor, and D. R. M. Walton. *J. Chem. Soc.-Chem. Commun.*, , 12, 1463–1464, (1994).

[157] A. Hebard, M. Rosseinsky, R. Haddon, D. Murphy, S. Glarum, T. Palstra, A. Ramirez, and A. Kortan. *Nature*, **350**, 6319, 600–601, (1991).

[158] M. D. Upward, P. Moriarty, P. H. Beton, P. R. Birkett, H. W. Kroto, D. R. M. Walton, and R. Taylor. *Surf. Sci.*, **405**, 2-3, L526–L531, (1998).

[159] J. Diaz, G. Paolicelli, S. Ferrer, and F. Comin. *Phys. Rev. B*, **54**, 11, 8064–8069, (1996).

[160] D. Wacker, K. Weiss, U. Kazmaier, and C. Woll. *Langmuir*, **13**, 25, 6689–6696, (1997).

[161] C. Mainka, P. S. Bagus, A. Schertel, T. Strunskus, M. Grunze, and C. Woll. *Surf. Sci.*, **341**, 3, L1055–L1060, (1995).

[162] M. X. Yang, M. Xi, H. J. Yuan, B. E. Bent, P. Stevens, and J. M. White. *Surf. Sci.*, **341**, 1-2, 9–18, (1995).

[163] K. Sakamoto, M. Harada, D. Kondo, A. Kimura, A. Kakizaki, and S. Suto. *Phys. Rev. B*, **58**, 20, 13951–13956, (1998).

[164] S. Suto, K. Sakamoto, D. Kondo, T. Wakita, A. Kimura, A. Kakizaki, C. W. Hu, and A. Kasuya. *Surf. Sci.*, **438**, 1-3, 242–247, (1999).

[165] M. de Seta, N. Tomozeiu, D. Sanvitto, and F. Evangelisti. *Surf. Sci.*, **460**, 1-3, 203–213, (2000).

[166] G. LeLay. *Surf. Rev. Lett.*, **4**, 2, 287–293, (1997).

[167] X. Tong, C. Jiang, and S. Hasegawa. *Phys. Rev. B*, **57**, 15, 9015–9023, (1998).

[168] M. H. Hecht. *Phys. Rev. B*, **41**, 11, 7918–7921, (1990).

[169] S. Hasegawa, K. Tsuchie, K. Toriyma, X. Tong, and T. Nagao. *Appl. Surf. Sci.*, **162**, 42–47, (2000).

[170] L. S. O. Johansson, E. Landemark, C. J. Karlsson, and R. I. G. Uhrberg. *Phys. Rev. Lett.*, **63**, 19, 2092–2095, (1989).

[171] P.-F. Coheur, J. Cornil, D. A. dos Santos, P. R. Birkett, J. Lievin, J. L. Bredas, D. R. M. Walton, R. Taylor, H. W. Kroto, and R. Colin. *J. Chem. Phys.*, **112**, 19, 8555–8566, (2000).

[172] G. Hughes, private communication.

[173] M. Grobis, X. Lu, and M. F. Crommie. *Phys. Rev. B*, **66**, 16, 161408, (2002).

[174] J. N. O'Shea, M. A. Phillips, M. D. R. Taylor, P. Moriarty, M. Brust, and V. R. Dhanak. *Appl. Phys. Lett.*, **81**, 26, 5039–5041, (2002).

[175] J. A. Theobald, N. S. Oxtoby, M. A. Phillips, N. R. Champness, and P. H. Beton. *Nature*, **424**, 6952, 1029–1031, (2003).